THE APPLICATION OF FAST CORRELATION METHODS WITH DISSOLUTION DNP ENHANCED NMR

A Dissertation

by

GUANNAN ZHANG

Submitted to the Office of Graduate and Professional Studies of
Texas A&M University
in partial fulfillment of the requirements for the degree of

DOCTOR OF PHILOSOPHY

Chair of Committee,	Christian Hilty
Committee Members,	David H. Russell
	Emile Schweikert
	Steven M. Wright
Head of Department,	Simon W. North

December 2017

Major Subject: Chemistry

ABSTRACT

Nuclear magnetic resonance (NMR) spectroscopy is a powerful analytical technique for chemistry and biochemistry. Since an inherent limitation of NMR is a lack of sensitivity, long experimental time with signal averaging or spins with high concentration are often required. An emerging technique, dissolution dynamic nuclear polarization (D-DNP), significantly enhances an NMR signal by several orders of magnitude. The large signal gains enable detection of spins with micromolar concentration and offer opportunities to various fields of applications.

Two dimensional (2D) correlation spectroscopy plays an essential role in identifying molecular structure and dynamics. Because of the non-renewability of the hyperpolarized spin state, this property prevents the application of conventional 2D methods which rely on repetition of the experiment by successive increments of the indirect dimension. Therefore, it is important to find applicable methods to circumvent this problem. The present dissertation is focused on using fast single-scan 2D and pseudo-2D correlation methods to elucidate molecular structures and characterize physical parameters, such as diffusion and spin relaxation, with the goal of investigating reaction kinetics and mechanisms as well as studying membrane transport of metabolite.

Since conventional 2D correlation spectroscopy is not compatible with D-DNP, an alternative way of collecting correlation information without obtaining an indirect spectral dimension is via off-resonance decoupling. Based on this concept, heteronuclear chemical shift correlations were determined in single scan DNP-enhanced NMR spectra under off

resonance decoupling by Scaling of Heteronuclear Couplings by Optimal Tracking (SHOT) pulses, with the purpose of determining the identity of transient species and reaction mechanisms.

Physical parameters of molecules, such as diffusion and spin relaxation, can further be characterized with single-scan correlation methods and used to examine membrane transport of metabolite. Ultrafast diffusion-T_2 correlation Laplace NMR enables one to correlate spin relaxation and diffusion parameters in a single-scan. Diffusion-T_2 correlation data was acquired by detecting hyperpolarized ^{13}C / ^{1}H signals of small molecules, and maps were generated using inverse Laplace transform. The accurate determination of diffusion and T_2 relaxation in homogeneous / inhomogeneous magnetic fields demonstrated the robustness of the method.

The usability of hyperpolarized UF-LNMR is then demonstrated in the context of cell metabolism, by investigating the conversion of pyruvate to lactate in the cultures of mouse 4T1 cancer cells. We show that ^{13}C ultrafast diffusion-T_2 relaxation correlation measurements, with the sensitivity enhanced by several orders of magnitude by D-DNP, allows the determination of the extra- *vs.* intracellular location of metabolites in the cells due to their significantly different values of diffusion coefficients and T_2 relaxation times.

DEDICATION

To my parents

ACKNOWLEDGEMENTS

Foremost, I would like to express my highest gratitude and regards to my advisor Dr. Christian Hilty. Thanks for his smart guidance and patience on my academic writing and experiments during my Ph.D study. Most importantly, he offered me so many opportunities that allowed me to learn NMR from different projects. He always provided great suggestion and advice that helped me to solve problems in my research. Without his guidance, I could not have completed these works.

I would like to thank my committee members, Dr. Russell, Dr. Wright and Dr. Schweikert, for guiding my research and their support through the course of this work. Furthermore, I wish to thank Dr. Son for his willingness to act as substitute committee member.

Many thanks to my collaborators in my projects. I really appreciate their useful discussion and fruitful collaboration. Thanks Dr. Schilling and Dr. Glaser for providing SHOT pulses about studying chemical shift correlations using hyperpolarized NMR. Thanks Dr. Ahola and Dr. Telkki for providing the ultrafast diffusion-T_2 pulse sequence about identifying intra- vs. extracellular metabolites in cancer cells. Thanks Dr. Lerche for providing samples and useful discussion on cell experiments. Thanks Dr. Meldrum for providing single-sided NMR instrument about investigating hyperpolarized ultrafast diffusion-T_2 correlation LNMR in inhomogeneous field.

I am thankful to my lab members, Youngbok Lee, Giridhar Sekar, Hsueh-Ying Chen, Mukundan Ragavan, Mengxiao Liu, Yunyi Wang, Chia-Hsiu Chen, Yaewon Kim, Yue Zhu, Jihyun Kim, and Ratnamala Mandal for comments on my work.

A special thanks to my family. I really appreciate their unconditional and great support.

CONTRIBUTORS AND FUNDING SOURCES

Contributors

This work was supervised by a dissertation committee consisting of Professor Christian Hilty, Professor David H. Russell, Professor Emile Schweikert of the Department of Chemistry and Professor Steven M. Wright of the Department of Electrical and Computer Engineering.

The SHOT pulses for Chapter 2 were provided by Dr. Franz Schilling and Professor Steffen J. Glaser of Technical University of Munich. In Chapter 4, the pulse sequence of D-T_2 correlation Laplace NMR experiment using a high field magnet was provided by Dr. Susanna Ahola and Professor Ville-Veikko Telkki of University of Oulu. The pulse sequence of D-T_2 correlation Laplace NMR experiment using a single sided magnet was provided by Professor Tyler K. Meldrum of College of William and Mary. The single sided nuclear magnetic resonance instrument was provided by Professor Tyler K. Meldrum. In Chapter 5, the pulse sequence of D-T_2 correlation Laplace NMR experiment was provided by Dr. Susanna Ahola and Professor Ville-Veikko Telkki of University of Oulu. For the analysis of D-T_2 data in Chapter 4 and 5, the 2D relaxation time and diffusion coefficient distributions was determined from a Laplace inversion program provided by Professor P. Callaghan (Victoria University of Wellington, New Zealand).

All other work conducted for the dissertation was completed by the student under the advisement of Professor Christian Hilty of the Department of Chemistry.

Funding Sources

This work was made possible by the National Science Foundation under Grants Number CHE-0846402 and CHE-1362691, the Welch Foundation under Grant Number A-1658, and the Ji and Li Family Foundation.

NOMENCLATURE

1D	One Dimensional
2D	Two Dimensional
ADC	Apparent Diffusion Coefficient
ALT	Alanine Aminotransferase
BAEE	N_{α}-Benzoyl-L-Arginine Ethyl Ester
BDPA	α,γ-Bisdiphenylene-β-Phenylallyl
BW	Bandwidth
CE	Cross Effect
CPG2	Carboxypeptidase G2
CPMG	Carr-Purcell-Meiboom-Gill
CW	Continuous Wave
D-DNP	Dissolution Dynamic Nuclear Polarization
DHFR	Dihydrofolate Reductase
DPBD	1,4-dipheneylbutadiene
D-T_2	Diffusion-T_2
DMSO	Dimethyl Sulfoxide
DNP	Dynamic Nuclear Polarization
E.coli	Escherichia coli
EG	Ethylene Glycol
EDTA	Ethylenediaminetetracetic Acid

Gd-DTPA	Diethylenetriamine Pentaacetic Acid Gadolinium Complex
LB	Lysogeny Broth
LDH	Lactate Dehydrogenase
LLS	Long-Lived Spin State
LNMR	Laplace Nuclear Magnetic Resonance
MCT	Monocarboxylate Transporter
MRI	Magnetic Resonance Imaging
NMR	Nuclear Magnetic Resonance
NNLS	Non-Negative Least Square Minimization
NOE	Nuclear Overhauser Effect
NS	Number of Scans
OPN	Osteopontin
OX63	tris[8-carboxy-2,2,6,6-tetrakis(2-hydroxyethyl)benzo[1,2-d:4,5-d′]bis[1,3]-dithiol-4-yl]methyl free radical sodium salt
PDH	Pyruvate Dehydrogenase
PGSE	Pulsed Field Gradient Echo
PGSTE	Pulsed Field Gradient Stimulated Echo
PTD	4-phenyl-1,2,4-triazole-3,5-dione
SE	Solid Effect
SEX	Selective X Nucleus
SH	Slice Height
SHOT	Scaling of Heteronuclear Couplings by Optimal Tracking

SNR	Signal to Noise Ratio
SVD	Singular Value Decomposition
TEMPOL	4-Hydroxy-2,2,6,6-Tetramethylpiperidine 1-Oxyl Radical
THF	Tetrahydrofuran
TMS	Tetramethylsilane
TM	Thermal Mixing
TXI	Triple Resonance
UF LNMR	Ultrafast Laplace Nuclear Magnetic Resonance

TABLE OF CONTENTS

Page

Page

Page

LIST OF FIGURES

FIGURE Page

LIST OF TABLES

CHAPTER I

INTRODUCTION

High resolution Nuclear Magnetic Resonance (NMR) spectroscopy is a powerful and modern analytical technique for structural characterization and molecular identification. NMR exploits molecules containing nuclei with spin quantum number > 0 which absorb an exact electromagnetic radio-frequency when exposed to an external magnetic field. The local electron environments in a molecule induce a local magnetic field experienced by a nucleus which leads to a variation in the exact radio-frequency that a nucleus absorbs. Chemical shifts of an NMR spectrum caused by such variation in frequencies are used to distinguish chemical species. Other than chemical shift, intra- or inter-molecular interactions are probed by correlations through bonds or space between nuclei by acquiring spectra with multi-frequency dimensions.[1] Macroscopic behavior of molecules dependent on molecular motions are captured by NMR relaxometry[2] and diffusometry studies.[3]

Various fields of applications are explored due to the different types of information provided by liquid-state high-resolution NMR. NMR is widely used to elucidate molecular structures,[4–6] for example organic compounds and natural products. It can also be used as an essential tool for monitoring molecular interactions,[7,8] determination of protein dynamics,[9,10] and investigation of biochemical processes.[11,12]

1.1 NMR Sensitivity

Despite unparalleled richness of information provided by NMR, NMR spectroscopy suffers from its lack of sensitivity. The reason for low sensitivity of NMR spectroscopy stems from the weak interaction between nuclear spins and an external magnetic field. Such interaction, described by Zeeman effect, results in the splitting of a single energy level into multiple spaced energy levels for different spin states. The energy transfer between spin states provides a basis for NMR spectroscopy. For a spin -1/2 system, the nuclear spins occupy two spin states which are denoted as α and β states correspond to the parallel (α state) or antiparallel (β state) orientation of nuclear spins with respect to the external field. Since α state has slightly lower energy than β state, more nuclear spins take up α state. Polarization, defined as a fraction of excess population that occupies α state, determines the sensitivity of NMR,

$$P = \frac{n_\alpha - n_\beta}{n_\alpha + n_\beta} \tag{1.1}$$

n_α and n_β are the populations of nuclei in α and β state. It is apparent that the sensitivity of NMR increases as the number of nuclei in the lower energy state increases.

According to Boltzmann statistics, the ratio of n_β over n_α is $e^{-\frac{\Delta E}{kT}}$. ΔE is the energy difference between two spin states, T is temperature, k is Boltzmann constant. Taking into account Boltzmann distribution, P is expressed as,

$$P = \frac{1 - n_\beta/n_\alpha}{1 + n_\beta/n_\alpha} = \frac{1 - e^{-\frac{\Delta E}{kT}}}{1 + e^{-\frac{\Delta E}{kT}}} = \tanh\left(\frac{\Delta E}{2kT}\right) = \tanh\left(\frac{\hbar \gamma B_0}{2kT}\right) \tag{1.2}$$

where γ is gyromagnetic ratio, B_0 is the strength of an external magnetic field, $\hbar = h/2\pi$ is the reduced Planck's constant. From Eq. 1.2, it can be seen that P and its corresponding

sensitivity is proportional to magnetic field strength. Because sensitivity scales by $B_0^{7/4}$,[13] recent years have witnessed the quest for increasing magnetic field strength. However, the higher expense with increased magnetic field strength and construction difficulties of ultra-high field NMR magnets limits the increase of experimental sensitivity.

One way to improve NMR sensitivity is to reduce noise. Signal to noise ratio (SNR) is calculated by dividing signal by a noise voltage V_{noise}, as shown in Eqs. 1.3 and 1.4,[14]

$$V_{noise} \propto \sqrt{4k(\Delta f)(T_{N,probe} + T_{N,preamp})} \tag{1.3}$$

where k is Boltzmann constant, $T_{N,probe}$ and $T_{N,preamp}$ are noise temperatures of probe and preamplifier, Δf is receiver bandwidth. Here, $T_{N,probe}$ and $T_{N,preamp}$ is expressed as,

$$T_{N,probe} = \frac{T_{coil}R_{coil} + T_{sample}R_{sample}}{R_{coil} + R_{sample}} \tag{1.4}$$

where T_{coil}/T_{sample} and R_{coil}/R_{sample} are temperatures and effective resistances of coil / sample, respectively. As indicated in Eq. 1.3, SNR can be increased by cooling the NMR probe and preamplifier. For example, the use of cryogenically cooled probes reduces noise contribution of a sample. Apart from cryogenic techniques, the use of low conductivity solvents[15] and a better probe design are proposed as well.

Despite reducing noise, maximizing signal intensity is a frequently used method. Typically, increasing the number of NMR-active nuclei is the most convenient way to improve signal intensity. This is usually achieved by increasing sample amount in a NMR receiver coil. But in some cases, such method is restricted by samples with limited mass or concentration.

Since SNR is proportional to the square root of number of signal averages, increasing the number of scans (NS) enables the improvement of SNR. However, the time that is required to increase NS poses a challenge to measurements which require rapid signal detection. Nevertheless, the simple implementation of this method allows its extensive use for various experiments.

Besides the various approaches mentioned above, the room for improvement of NMR sensitivity is still limited by the low nuclear spin polarization in the range from ~10^{-6} to ~10^{-4} for nuclei, such as ^{13}C, ^{1}H, ^{15}N, under thermal equilibrium conditions. Therefore, other efficient strategies are required to significantly improve the degree of polarization for NMR measurement.

1.2 Enhancing Magnetic Resonance Signal Using Dynamic Nuclear Polarization

In the early 1950s, Albert Overhauser first demonstrated the use of Overhauser effect to polarize metal nuclei.[16] Carver and Slichter later observed an enhanced lithium spectrum experimentally.[17] In Overhauser enhanced dynamic nuclear polarization (DNP), an increased nuclear signal is detected by irradiating electrons at electron Larmor frequency. Such enhancement results from polarization transfer caused by cross-relaxation between electron and nuclear spins. This method opens the possibility to significantly increase P above thermal equilibrium level. With hyperpolarization, the polarization enhancement factor ε which is defined as,

$$\varepsilon = \frac{P_{hyperpolarization\ state}}{P_{thermal\ equilibrium}} \tag{1.5}$$

can reach 4~5 orders of magnitude in high field and even greater in low field.[18,19] The realized ε is exhibited in the enhanced NMR sensitivity and its corresponding detectable NMR signal.

Since the main application of Overhauser DNP is in solution, sample heating due to microwave irradiation decreases polarization efficiency which becomes a limiting factor for its extensive use. An alternative way to generate high polarization is to polarize samples in solid state. The hyperpolarization occurs via three main mechanisms: solid effect, cross effect and thermal mixing. To realize polarization transfer, it requires the addition of radical with free electrons to provide a paramagnetic center. The radical and its corresponding EPR linewidth (δ) indicate the major mechanism that achieves hyperpolarization.[20]

1.2.1 Solid Effect

The solid effect (SE) depends on the hyperfine coupling of a two spin system involving an electron and a nucleus.[21] As shown in Figure 1.1a, population is determined by Boltzmann distribution at thermal equilibrium. Mixing electron and nuclear spin state partially allows double quantum and zero quantum transitions (see Figure 1.1b and c). Microwave irradiation at frequency $(\omega_e - \omega_n)$ pumps electron-nuclear spin pairs from |2> to |3> corresponding to a double quantum transition. Electron-nuclear spin pairs subsequently restore to |1> with an appropriate assumption that $W_S \gg W_2, W_0 \gg W_I$, where W_S, W_I and W_2 / W_0 are electron, nuclei and cross relaxation rates. The repetition of this process leads to population at |1> larger than that at |2>. The net effect is pumping spin pairs from |2> to |1>, resulting in a positive nuclear spin polarization. The same

procedure applies for irradiation at frequency $(\omega_e + \omega_n)$ (zero quantum transition) which allows a negative nuclear spin polarization. Since microwave irradiation at frequencies $(\omega_e - \omega_n)$ and $(\omega_e + \omega_n)$ leads to opposite effect, the two resulting EPR line must be well resolved. This requires a homogeneous EPR linewidth (δ) and an inhomogeneous spectral breadth (Δ) of the polarizing substances smaller than nuclear Larmor frequency (ω_I). The fulfillment of SE needs a polarization agent exhibiting narrow EPR linewidth. Radicals, such as BDPA,[22] OX63,[23] satisfy this requirement. These radicals are frequently used in ^{13}C enhanced experiments. Haze[24] introduced a highly water-soluble BDPA derivative which not only preserves DNP properties of BDPA, but also extend its utility in biological applications to aqueous media.

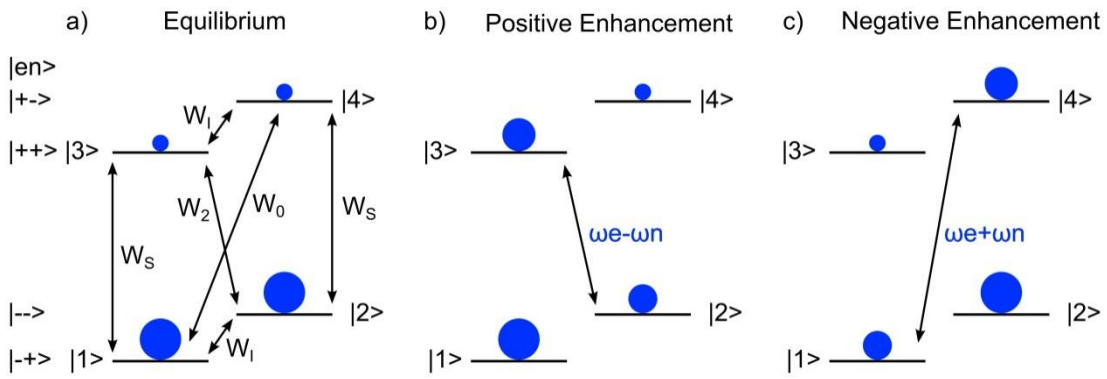

Fig. 1.1. Energy level diagram for DNP solid effect. a) A two spin system in thermal equilibrium. W_S ,W_I, W_2 and W_0 are EPR, NMR, double quantum and zero quantum transitions, respectively. Transitions at frequencies $(\omega_e - \omega_n)$ and $(\omega_e + \omega_n)$ lead to positive and negative nuclear spin polarization in b) and c). Blue colored balls represent spin populations. [25,26]

1.2.2 Cross Effect and Thermal Mixing

When $\Delta > \omega_I$, cross effect (CE) and thermal mixing (TM) dominates the mechanism. The two mechanisms are further distinguished by whether the EPR spectrum is either inhomogeneously ($\Delta > \delta$) or homogeneously ($\Delta \approx \delta$) broadened, respectively.[21] CE is explained by a three spin system including two electrons and a nucleus. CE occurs when $|\omega_{0S1} - \omega_{0S2}|$ matches ω_{0I}. Here, ω_{0S1} and ω_{0S2} are Larmor frequencies of two coupled electrons. $\omega_{0I}$is nuclear Larmor frequency. Two EPR frequencies ω_{0S1} and ω_{0S2} are split by ω_{0I}, maximizing the efficiency of CE.[25] TM is caused by a strongly coupled, multiple electron spin bath, resulting in manifold of states which is an extension of CE.[21] Since CE requires a coupling between two electrons which has an appropriate Larmor frequency difference, biradical polarization agents, such as two TEMPO radicals with a poly(ethylene glycol) linkage[27] or TOTAPOL[28], are employed.

DNP does not require any special features of polarized substances. Almost any molecules are able to be polarized using DNP. To achieve a highly efficient polarization transfer, radicals need to be dispersed among nuclear spins homogeneously. This requires a polarization agent forming an amorphous glassing matrix in the solid state. Some solvents, such as toluene, glycerol or styrene, are glass-forming by itself. Other than that, a mixture of two or multiple solvents, such as dimethyl sulfoxide/water (1/1, v/v) or ethylene glycol/water (3/2, v/v), satisfy this condition.

1.3 Dissolution DNP Enhanced NMR Experiments

1.3.1 Dissolution DNP

For applications of DNP in the solution state, the most striking strategy is a technique where polarization occurs in the frozen solid state and NMR measurement in the liquid state, which is also called dissolution DNP (D-DNP) method pioneered by Ardenkjær-Larsen in 2003.[29] In this method, an analyte molecule mixed with an organic radical are dissolved in a glass-forming solvent. This sample aliquot is hyperpolarized at temperature ~1.4 K for an optimal polarization time, by irradiating microwave at an appropriate frequency ($(\omega_e + \omega_n)$ or $(\omega_e - \omega_n)$) in a 3.35 T magnetic field. Subsequently, the hyperpolarized sample was quickly dissolved in pre-heated solvent, and injected into an NMR tube installed in an NMR instrument.

The signal enhancement εh is calculated as,[25]

$$\varepsilon h = \varepsilon' \cdot \frac{B_{DNP}}{B_{NMR}} \cdot \frac{T_{NMR}}{T_{DNP}} \tag{1.6}$$

where ε' is the actual solid-state DNP enhancement.[30] Typically, a temperature factor $T_f = \frac{T_{NMR}}{T_{DNP}}$ is ~250 with T_{NMR} = 298 K and T_{DNP} = 1.2 K. Thanks to T_f, D-DNP can achieve a higher enhancement than other DNP methods, such as solid state DNP and Overhauser DNP.[25]

Since the relaxation of hyperpolarization to thermal polarization is on the time scale of solution-state T_1 relaxation, the actual signal enhancement in liquids is smaller than εh (Eq. 1.9) due to polarization loss during sample transfer from DNP polarizer to NMR magnet. In order to avoid such loss, molecules with long T_1 relaxation are preferred.

For instance, $^{13}C_1$-pyruvate has 60 s T_1 relaxation[31] which accounts for ~ 10% relaxation with 6 s sample transfer time.[29] Atoms, such as carbonyl carbon or quaternary ammonium cation, have longer T_1 due to reduced dipole-dipole interaction without an attached ^1H. A signal enhancement of > 10,000 fold can be achieved.[29] However, if molecules of interest have short T_1, this would cause a loss of polarization.

1.3.2 Sample Injection Techniques

The development of rapid sample injection technique achieves a more efficient transfer of polarization to an NMR spectrometer.[32] An automatic device for sample injection was designed by Bowen *et al*.[33,34] Polarized sample after dissolution is transferred to an injection loop and detected by an optical sensor. This triggers a two-way valve switched to an injection position. Subsequently, the sample is pushed by a high pressure gas to an NMR tube preinstalled in a magnet. From the start of dissolution to the start of NMR measurement, the total time elapsed is ~ 1s. Since the line width of an NMR signal is determined by sample homogeneity, any gas bubbles present after sample injection would result in line broadening. To avoid this and guarantee a high resolution NMR spectrum, a pressure is maintained in the tube during the entire data acquisition period. The resulting linewidth satisfies most applications.

Residual motion brought by sample shuttling using gas driven injection was observed during NMR measurement and quantitatively characterized.[35] The effect of residual motion becomes a concern for experiments using pulse field gradients. Chen *et al.* introduced a flow injection device which avoids much of the turbulence inherent in gas-driven injection and shows a similar performance in terms of linewidth and injection

time.[36] In this design, polarized sample is transferred to a flow cell by a high pressure liquid rather than a high pressure gas.

By reducing transfer time, gas driven or liquid driven injection enables stopped-flow analysis making use of most of polarization. Alternative ways to prevent polarization loss during sample transfer, such as shortening transfer path length or removing radicals from hyperpolarized samples, are proposed as well. The design of a dual-isocenter magnet allows a rapid sample transfer between two different areas of a magnet, an upper compartment for DNP enhancement and a lower compartment for NMR measurement, within 0.7 s.[37] For microfluidic application, the implementation of a transfer system realizes DNP hyperpolarization and NMR detection in different regions of a home built probe.[38] For *in vivo* application, the sample is usually transferred to a syringe which is used to manually inject hyperpolarized substrate solution into isolated cells or animals.[32] An automated sample transfer and injection system was also developed. Radicals are scavenged without the cost of reducing the final sample concentration before injection into living animals.[39]

1.3.3 Long-lived Spin States

Since hyperpolarization is a non-equilibrium distribution of nuclear spin populations,[40] a hyperpolarized spin system will eventually return to an equilibrium state because of spin-lattice relaxation. In order to enhance the sensitivity of NMR by hyperpolarization, increasing lifetime of hyperpolarization is important. The so-called long-lived spin state (LLS), generated due to the symmetry properties of the spin system, opens the possibilities to extend hyperpolarization lifetimes from the order of seconds to

minutes or even hours.[40] Since the transitions from nuclear singlet state to triplet state break spin-exchange symmetry and are often slow, the lifetime of nuclear singlet order is longer than T_1 relaxation, in case that such transitions are suppressed.[41] In consequence, the lifetime of nuclear singlet order is extended and converted afterwards into observable magnetization by broken the exchange symmetry.[41] Singlet NMR is combined with D-DNP by a variety of ways. For instance, hyperpolarized magnetization was generated in a DNP polarizer and converted into long-lived singlet state in a high field magnet after dissolution.[42,43] Alternatively, hyperpolarized nuclear spins were transferred to high field to prepare an initial condition which was converted into a long-lived state by shuttling to a low magnetic field.[44] By converting small fractions of the populations of long-lived states into observable magnetization at desired intervals, it opens the possibility to investigate slow chemical reactions and slow transport phenomenon, such as molecular diffusion.[43]

1.3.4 Fast Correlation Spectroscopy

A significant challenge in realizing signal enhancement for solution state NMR is the non-renewability of the hyperpolarized spin state. Since most of the molecules have short T_1 relaxation in the liquid state, this requires data acquisition accomplished in a limited time. As correlation NMR spectroscopy is an important tool to characterize structures and dynamic properties of molecules, several single-scan detection strategies are developed to realize these measurements that are applicable to D-DNP.

By spreading the spectral peaks over a 2D frequency plane, 2D correlation spectroscopy allows to extract structural and dynamic information of molecules.[45] In

correlation spectroscopy, the connectivity of atoms in a molecule is established through chemical shift correlations between neighboring spins.[46] Modern NMR spectroscopy uses heteronuclear or homonuclear correlations to study structures of proteins, polymers and nuclei acids. However, the acquisition of correlation spectroscopy relies on repetition of the experiment by successive increment of the indirect dimension. This property is not applicable to D-DNP due to non-renewable hyperpolarization. Several strategies are proposed to circumvent this problem so that correlation information can be acquired in a single scan. Frydman and coworkers developed a UF approach (UF 2D NMR) based on gradient encoding, capable of recovering any kind of correlation information in a single scan.[45,47–49] In this approach, instead of increasing the evolution time (t1) with each increment in conventional correlation methods, the whole volume of a sample is spatially partitioned into sub-volumes, and a different evolution time is ascribed to a different sub-volume.[50] By collecting signals from various partitions, correlation information can be obtained in a single scan. Hilty and coworkers reported methods to reconstruct chemical shift correlations by acquisition of 1D spectra using D-DNP, including Hadamard spectroscopy using flow NMR,[51] off-resonance decoupling scheme using continuous wave decoupling[52] and scaling of heteronuclear couplings by optimal tracking.[46,53] In off-resonance decoupling, a radiofrequency field is applied at the frequency of one type of nucleus during the acquisition of a one dimensional spectrum of a second type of nucleus.[46] Based on the magnitude of the observed residual coupling constants, correlation information can be constructed by calculating the difference in chemical shift between the irradiation frequency and the actual frequency of the coupled spin.[46] The single scan

approach facilitates the application of multidimensional correlation spectroscopy with D-DNP, providing unprecedented opportunities to elucidate structures of mass-limited samples as well as investigate fast chemical and biochemical non-equilibrium processes.

NMR spectroscopy is one of the most powerful techniques for characterizing physical properties of molecules. NMR measurements of spin relaxation and molecular self-diffusion (D) explore molecular interactions and molecular motion, providing detailed chemical information by these parameters. The most commonly used pulse techniques for measuring spin-lattice relaxation, spin-spin relaxation and diffusion coefficient involving inversion-recovery sequence, Carr–Purcell–Meiboom–Gill (CPMG) sequence and pulsed field gradient spin-echo or pulsed field gradient stimulated echo sequence. However, for a sample containing different spin systems which have similar physical properties, the independent measurement with T_1, T_2 or D alone cannot distinguish the spins. For instance, it has been found that the two spin systems cannot be separated if their T_2s differ by a factor less than 5 fold.[54] In such a case, the heterogeneity of spins can be resolved by adding a second dimension which helps to enhance the resolution of an image.[55] The joint distribution of T_2 and T_1 relaxation or T_2 relaxation and diffusion components is measured in two dimensional correlation experiments.[56,57] The acquisition of a correlation spectrum using conventional methods requires repetition of the experiment by successive increment of the indirect dimension, which is not applicable to D-DNP due to the non-renewable spin state. A fast correlation method, ultrafast Laplace NMR (UF-LNMR), enables one to carry out two dimensional (2D) relaxation and diffusion measurements in a single-scan. This method relies on spatial encoding of multidimensional data, on the basis of 1D

diffusion[58–60] and relaxation experiments[61] as well as UF NMR spectroscopy.[62,63] Ahola presented a UF T_1-T_2 correlation[64] and a UF diffusion-T_2 correlation LNMR experiment by a high field magnet.[65] King demonstrated measurements of UF T_1-T_2 correlation spectra using a single-sided magnet.[66] The obtained T_1-T_2 or diffusion-T_2 map by Laplace inversion provides a combined T_1-T_2 or diffusion-T_2 contrast as well as an improved image resolution. A single scan is sufficient to obtain the same information as conventional multidimensional measurements. The significantly reduced experimental time due to the single scan approach facilitates the use of D-DNP technique to boost experimental sensitivity. This method opens new avenue to investigate molecular processes,[64] distinguish identical molecules in different physical environments and enhance chemical resolution in the spectra.[65]

1.4 Applications of Dissolution DNP Enhanced NMR in Chemistry and Biochemistry

1.4.1 Cellular Metabolism

The characterization and understanding of cellular metabolism is of fundamental importance for disease diagnosis and treatment,[67] such as cancer, diabetes and cardiac disease. The advent of high-resolution liquid-state NMR, coupled with its unparalleled ability to yield extensive information on diverse biological processes, opens the possibility to monitor metabolism.[68] Last decades have witnessed the development of NMR to track metabolic pathways in perfused organs,[69] animal models[70] and humans.[71,72] Insights have been gained into physiological control and regulation of a wide range of cellular metabolism. Many efforts have been devoted to develop NMR to target key biomolecular activities aiming to understand biological processes and mechanism.[73]

The development of D-DNP which enhances the signals of molecules by more than 10,000 fold,[29] makes a significant breakthrough in this field. ^{1}H is the most frequently used nuclei, due to its ~100% natural abundance and high sensitivity. One shortcoming of ^{1}H is its small chemical shift dispersion which results in signal overlap. Since ^{13}C covers a large chemical shift range, various metabolic precursors with ^{13}C isotopic labeling, such as pyruvate, glucose, fumarate, and others, have served as probes for specific metabolic pathways.[20]

In vitro Cellular Metabolism

The employment of real time DNP enhanced NMR assays permits to detect enzymatic transformations of hyperpolarized metabolic precursors in various cell lines *in vitro*. After injection hyperpolarized substrates into cell suspensions preloaded in an NMR tube, a series of ^{13}C spectra are acquired by exciting ^{13}C nuclei with a small flip angle (e.g. 10^{o}) excitation pulse. A repetition time is used between successive scans. The hyperpolarized metabolic precursors and downstream metabolites are then observed in real-time spectra. Meier visualized central carbon metabolism of living *Saccharomyces cerevisiae* and *Escherichia coli* (*E.coli*) by injection hyperpolarized [U-^{2}H, U-^{13}C] glucose to cell suspensions.[74,75] The time-resolved NMR assays followed the entire pathway from glucose to the catabolic end products via various transient pathway intermediates.[74,75] Hyperpolarized metabolites were produced by sequential enzymatic transformation steps and observed in a series of ^{13}C NMR spectra in real time.

From the time resolved spectra, the kinetic analysis of signal intensities of the metabolites enables to quantify metabolic flux. Pyruvate, a key intermediate in many

biological pathways, is the most widely used metabolic precursor for this purpose, due to its long T_1 relaxation and rapid conversion to other metabolites. Several kinetic models are reported to quantify the metabolic flux between pyruvate and its downstream metabolites *in vitro*.[76] A two-site exchange model was used to fit peak intensities of labeled pyruvate and lactate to the modified Bloch equations.[77] Harrison compared two-pool and three-pool first-order models for kinetic analysis of exchange between pyruvate and lactate. It was found that the simpler two-pool model was sufficient to determine the ^{13}C lactate concentration measured only by D-DNP, whereas the three-pool model was necessary to fit the combined data measured from both mass spectroscopy and D-DNP.[78] Instead of using kinetic modeling, Hill proposed a model free approach. It was demonstrated that the ratio of the total areas under the curve of pyruvate and lactate is proportional to the forward rate constant, without depending on the pyruvate input function.[79] The analysis was robust and applicable to a range of cancer lines.

The flux between pyruvate and its downstream metabolites depends on several factors, involving the activity of monocarboxylate transporter (MCT) which mediated the transfer of extracellular pyruvate to intracellular space and the intracellular enzyme which catalyzed the net conversion for the metabolic flux. Witney showed control of flux from pyruvate to lactate is dependent on both MCT and the enzyme lactate dehydrogenase (LDH) in a murine lymphoma cell line.[80] Another study monitored the effect of treatment with the mitogen-activated extracellular signal-regulated kinase inhibitor in prostate and breast cancer cell suspensions using pyruvate.[81] A drop in flux of breast cells but an increased flux of prostate cells was observed. A further investigation found a reduced

expression of MCT1 in breast cells. This explained the decreased flux and proved MCT-1 mediated transport of pyruvate as a rate limiting step in drug treated breast cells.[81] Keshari reported a significantly higher MCT4 expression and corresponding higher lactate efflux in metastatic renal cell carcinomas.[82] Reineri assessed the rate of hyperpolarized metabolites from intra- to extracellular space by "quenching" extracellular metabolites signal using a paramagnetic substance.[83] Then information about exchange rate of metabolites across membrane was extracted from analysis of decay curves of intracellular metabolites signals.[83]

In addition to measure metabolic flux, diffusion measurement is another approach to localize signals of metabolites to the intra- and extracellular environments which is a more direct way to examine transport.[84] Apparent diffusion coefficients (ADC) of lactate and pyruvate were measured after injection hyperpolarized pyruvate into human breast cancer cells. The observed ADC of pyruvate and lactate is significantly different. This indicates that pyruvate is predominantly from extracellular space and lactate predominantly stems from intracellular space. During progressive membrane permeabilization, a decreased ratio of ADC_{pyr} to ADC_{lac} was observed due to an increased blending of the intra- and extracellular compartments with time.[85] In another study, extra- and intracellular signals of pyruvate and lactate were identified by diffusion measurements using renal cell carcinomas.[86] In order to probe membrane transport of metabolites, cells were treated with a MCT inhibitor and an increase in intracellular lactate pool was observed.

In vivo Cellular Metabolism

The application of D-DNP to *in vivo* ^{13}C NMR was initially used for early-stage diagnosis of cancer by Golman.[87–89] Since one hallmark of metabolic pathways in cancer cells is the enhanced aerobic glycolysis which is referred to as Warburg effect,[90] these types of measurements probe different dynamic information of metabolic fluxes between normal and cancerous tissues due to their different metabolite levels.[91] So far, the most widely used hyperpolarized ^{13}C metabolic precursor is pyruvate. In cancer cells, pyruvate is predominantly converted to lactate by lactate dehydrogenase or alanine by alanine aminotransferase (ALT) in cytosol, resulting in an abnormally high concentration of lactate or alanine due to a high glycolysis rate. The flux of hyperpolarized ^{13}C label from pyruvate to lactate and alanine is used to grade tumor and determine response of tumors to drug treatment in a variety of tumor models *in vivo*, including prostate, hepatocellular carcinoma, glioma, lymphoma, and so on.[25,77,84,92]

The percentage of tumor cell necrosis *in vivo* also reflects early response of tumors to treatment. If membrane transport of a hyperpolarized precursor is slow, a small amount of hyperpolarized metabolic products would be observed in the polarization time frame. On the other hand, if cancer cells are treated with anticancer drugs, cell necrosis results in increased permeability of cell membrane which leads to a higher production of metabolites due to a rapid transport of metabolic precursors into cells. Based on this principle, fumarate is used as a metabolic precursor for this purpose. After treating implanted lymphoma tumors with etoposide for 24 hours, a 2.4-fold increase in hyperpolarized [1,4-$^{13}C_2$]malate production from hyperpolarized [1,4-$^{13}C_2$] fumarate was observed.[93,94] This

indicated significant levels of tumor cell necrosis. Therefore, the formation of hyperpolarized ^{13}C-labeled malate from [1,4-$^{13}C_2$]fumarate is a sensitive marker of tumor cell death *in vivo* and could be used to characterize the early treatment response of tumors.[93,94]

In tissues with a high aerobic capacity, such as heart, metabolic precursors, such as pyruvate, undergoes rapid decarboxylation, catalyzed by intra-mitochondrial pyruvate dehydrogenase to produce hyperpolarized $^{13}CO_2$.[95] If sufficient carbonic anhydrase is present to catalyze the equilibrium between $^{13}CO_2$ and $H^{13}CO_3^-$, their intensity ratio can be used to calculate *in vivo* pH.[95,96] The rate of appearance of $^{13}CO_2$ and $H^{13}CO_3^-$ reflects flux through pyruvate dehydrogenase (PDH)[97] is sensitive to physiological perturbations, such as fasting, diabetes and ischemia.[98,99] In other organs, such as liver, metabolic flux of hyperpolarized pyruvate is different than in heart. Its primary pathway in tricarboxylic acid cycle is catalyzed by pyruvate carboxylase which produces malate and aspartate. The production of hyperpolarized $H^{13}CO_3^-$ from $^{13}C_1$-pyruvate follows multiple mechanisms, catalyzed by phosphoenolpyruvate carboxykinase, isocitrate dehydrogenase, or PDH.[100]

Other hyperpolarized metabolic precursors, such as α-ketoisocaproic acid,[101] butyrate,[102] glutamine,[103] ascorbate and dehydroascorbate,[104–106] were also reported as sensitive biomarkers for *in vivo* and *in vitro* applications. The first successful clinical trial with human prostate cancer using $^{13}C_1$-pyruvate demonstrates the potential of hyperpolarized MR technique to translate to clinic for disease diagnosis and treatment monitoring in the future.

1.4.2 Enzymology

One benefit of D-DNP enhancement NMR is that the entire hyperpolarized signal is available at one time, which opens the possibility to investigate enzyme reactions in real time. Typically, the fate of a hyperpolarized molecule catalyzed by an enzyme is tracked over time, yielding real-time reaction progress curves.[107] The observation of kinetic processes opens new avenue to study reaction kinetics and mechanisms. Bowen reported a time-resolved D-DNP enhanced ^{13}C NMR spectroscopy for studying enzyme kinetics,[34] using the hydrolysis of N_{α}-benzoyl-L-arginine ethyl ester (BAEE) catalyzed by enzyme trypsin as a model reaction. The progress of the reaction was monitored in a multi-scan manner, by observing the consumption of substrate signal and buildup of product signal over the course of 3 s. A small proportion of the hyperpolarized signal was utilized in each scan by a variable flip angle pulse. The resulting normalized signal intensities of BAEE were fit to a linear function where a rate of catalysis was obtained. Miclet presented a real-time monitoring of the enzymatic phosphorylation reaction of glucose by hexokinase.[108] Under the assumption of a pseudo-first order reaction, a simple model was proposed, taking into account the inhibition of reaction product. The obtained kinetic constants demonstrated a comparable kinetics for the phosphorylation of two glucose anomers. Allouche-Arnon proposed a kinetic model of obtaining kinetic parameters in successive enzymatic reactions which enables quantitative analysis for multi-step reactions.[109] Jensen reported the detection and quantification of low-populated reaction intermediates in a consecutive and competing acetyl-CoA synthetase reaction, demonstrating the ability of real-time hyperpolarized NMR assays to elucidate reaction mechanisms.[110]

Apart from studying reaction kinetics and mechanisms, enzyme activities also serve as reporter probes for monitoring cell activity and function. Acetyltransferase, which catalyzes the transfer of acetyl group from peptides and small molecules, involves in gene regulation.[20] Chen reported a ^{13}C MR reporter system, where de-acetylation of the prepolarized [1-^{13}C]N-acetyl-L-methionine catalyzed by the aminoacylase-1 enzyme was detected and imaged by magnetic resonance imaging (MRI).[111] The system was translated to an *in vitro* application where the de-acetylation of the substrate was monitored in HEK 293 cells transfected with Acy-1 reporter gene.[111] The observed product signal indicated the elevated aminoacylase-1 expression and provided insights into cell functions. The study demonstrated that indirect labeling cells with reporter genes provided an essential tool for reporter-based cell detection.[111] Choline metabolism has been found to be related to stage and progression in a variety of cancer types.[20] Allouche-Arnon presented the monitoring of the synthesis of the deuterated acetylcholine from hyperpolarized [1,1,2,2-D_4,2-^{13}C] choline chloride. The reaction was catalyzed by carnitine acetyltransferase enzyme. Because of deuteration, the observed signals had longer T_1 which facilitates the use of this system for *in vivo* applications to study brain activity.[112] Carboxypeptidases, a group of protease enzymes, play a role to cleave carboxyl groups of molecules and are associated with protein regulation.[20] This enzyme reaction needs the coordination of the zinc ion. Jamin observed a conversion of a hyperpolarized reporter probe 3,5-difluorobenzoyl-L-glutamic acid to 3,5-difluorobenzoic acid and L-glutamic acid mediated by a bacterial enzyme Carboxypeptidase G2 (CPG2). The capability of

observing peptide carboxyl cleavage using CPG2 as a reporter enzyme has the potential to be translated to *in vivo* applications, with the goal of probing the activity of CPG2.[113]

1.4.3 Organic Reactions

Hilty and coworkers widened the application range of reactions monitored by hyperpolarized NMR spectroscopy to organic reactions, demonstrated with Grignard reaction,[114] Diels-Alder reaction,[115] styrene polymerization[116] and olefin polymerization.[117] Bowen reported the Grignard addition of methylmagnesium bromide to 3-methylbenzophenone.[114] In this experiment, atom positions of reactant and reaction product were correlated by selectively inverting a spin state of the reactant. The reactant underwent continuous transformation and carried over the inverted polarization to reaction product. Due to the use of hyperpolarization, this transfer was followed in real time with sufficient sensitivity of ^{13}C nuclei at natural isotope abundance.[114] The resulting correlation scheme helped to identify molecular structures as well as reaction mechanisms.

Apart from determining molecular structures in a reaction through chemical shift correlations, kinetic models were proposed which facilitated the determination of reaction kinetics and mechanisms. Zeng explored the effects of spin-relaxation on the signal intensities in reactions investigated by DNP-NMR, using a Diels-Alder reaction of 1,4-dipheneylbutadiene (DPBD) with 4-phenyl-1,2,4-triazole-3,5-dione (PTD) as a model reaction.[115] By fitting the signal intensities of the reactant and reaction product via a kinetic model, reaction rate constants and relaxation rates were obtained quantitatively.[115] The model took into account auto- and cross-relaxation in dipole-dipole coupled spin systems[115] which are applicable to NMR of most small molecules. The obtained reaction

rates and relaxation constants provided information about the structure of reaction product as well as reaction mechanism. Lee demonstrated real-time measurements on anionic polymerization of hyperpolarized styrene monomers.[116] During reaction progression, intermediates were identified via chemical shift correlation with the reactant. The kinetic information of the reaction was extracted via a kinetic model in which propagation rate constant of polymerization were obtained. In this model, the signal intensity of the living anionic polystyrene chain end was calculated, taking into account fresh polarization added through monomer addition and polarization lost through both spin relaxation and the transition of a given moiety to the interior of the polymer.[116] The method offered a way for fundamental studies of polymerization reactions.[116]

Chen presented the stereochemistry, kinetics, and mechanism of olefin polymerization catalyzed by a set of zirconium-based metallocenes investigated by DNP enhanced NMR.[117] A C_2 symmetric catalyst, [(EBI)ZrMe]-[$B(C_6F_5)_4$] (EBI = rac-(C_2H_4(1-indenyl)$_2$)), and a C_{2v} symmetric catalyst, [$(Cp)_2$ZrMe][$B(C_6F_5)_4$] (Cp = cyclopentadienyl),[117] were used to catalyze the in situ polymerization of hyperpolarized 1-hexene. Hyperpolarized monomer and oligomer signals were identified from time-resolved ^{13}C NMR spectra. By calculating the signal intensities of isomers, signal contributions from different elements of tacticity can be determined from ^{13}C NMR spectra.[117] The results indicated that isotactic or atactic forms of the polymers were dominant in the reaction catalyzed by [(EBI)ZrMe]-[$B(C_6F_5)_4$] or [$(Cp)_2$ZrMe][$B(C_6F_5)_4$], respectively. By employing chemical shift correlations using the same principle as demonstrated by Bowen,[114] minor peaks observed in the spectra were identified. These

peaks were originated from signals of side products, vinylidene-terminated polymer chains. Elucidation of the side products also proved the previously proposed reaction mechanism. By kinetic analysis of time dependence of the signals from monomers or polymers, rate constants for the polymerization process (k_p) as well as the deactivation process of the catalyst-polymeryl species (k_d) were obtained. Investigation of the influence of catalyst concentration on rate constants showed that k_p was dependent on catalyst concentration and k_d was independent on the concentration. These properties indicated a second-order process for the polymerization reaction and a first-order process for the deactivation reaction.[117]

1.4.4 Molecular Interactions

Protein-Ligand Interactions

Investigation of the interaction between a ligand and a protein reflects the biological effect of a ligand on the activity of a targeted protein, providing insights into regulation of biological functions as well as design of new bioactive molecules.[118] High resolution NMR spectroscopy is one of the biophysical techniques to study protein-ligand interactions with a large range of affinities (10^{-9}-10^{-3} M),[118] and is extensively used in pharmaceutical research for the screening of fragment libraries.[119] Protein-ligand complexes are detected by ligand observation and protein observation in which NMR parameters of protein and ligand are compared in their free and bound state.[118] However, one challenge that limits the general applicability of NMR based methods for studying protein-ligand interactions is the low signal to noise ratio of the experiment. D-DNP, which significantly enhances NMR signal by several orders of magnitude, solves this

problem. The large signal gains permit the identification and quantification of a broad range of binding constants and different binding kinetics through various NMR parameters, such as chemical shift, linewidth and peak height.[119,120]

Apart from characterization of binding, information on binding epitope can be obtained by observing protein-mediated magnetization transfer between two competitive ligands.[121] Based on inter-ligand nuclear Overhauser effect (NOE), polarization is transferred from one ligand to the other via a binding pocket on a target protein. Hyperpolarization of one of the ligands provided a sufficiently large sensitivity contrast, enabling the analysis of build-up of transferred signal intensities from one hyperpolarized ligand to the other non-hyperpolarized ligand via a kinetic model. From the obtained build-up rate, limited structural information on the binding epitope were obtained.[121]

Ligand-based NMR screening with competitive binding was also developed using ^{19}F NMR spectroscopy for determining binding affinity of compounds. If a fluorinated reporter ligand is in fast exchange with a protein, binding of a second, non-fluorinated ligand causes changes in the binding fraction of the bound reporter ligand, resulting in an observable change in R_2.[122] Thus, binding affinities of non-fluorinated ligands, in terms of dissociation constant (K_D), are characterized. If the detection sensitivity is enhanced by D-DNP technique, the experiment can be accomplished using a rapid, single-scan Carr–Purcell–Meiboom–Gill (CPMG) experiment. The detectable range of K_D was further extended in a parallel screening experiment. The hyperpolarized fluorinated reporter ligand was mixed with two protein samples injected into two flow cells.[123] The protein samples consisted of the same mixture of a target protein and a ligand of interest,

differentiated by different concentration ratios between the protein and the ligand. Two single-scan CPMG experiments were conducted simultaneously where an averaged K_D value was derived. This method enables the characterization of two ligands of interest that have binding affinities differing by an order of magnitude without changing any experimental conditions.[123]

Wang demonstrated a method for site specific characterization of protein-ligand interactions. A predominantly enhanced ^{1}H signal of the protein dihydrofolate reductase (DHFR) on its methyl group region was observed when mixed with a hyperpolarized ligand folic acid. ^{13}C single quantum selection was used to acquire NMR spectra where ^{13}C chemical shift ranges of the methyl groups can be identified. The observed methyl proton signals were consistent with the chemical shifts of amino acids in the active site of DHFR-folic acid complex.[124]

Lerche reported a competitive assay to characterize binding of hyperpolarized ligands, salicylate and ascorbate, to human serum albumin using ^{13}C NMR spectroscopy.[125] Stronger binding salicylate showed a pronounced signal loss due to the larger fraction of time in the faster-relaxing target-bound state and exchange line broadening.[125] Such strong effect on signal intensity of a ligand due to strong binding implied the feasibility of using hyperpolarized ligand signal to detect protein-ligand interactions with a wide range of binding affinities. Apart from a significant signal loss, binding was also observed as chemical shift changes for salicylate. Additionally, ligand binding to enzymes was also assessed by real time activity assays of enzyme in presence of an inhibitor.[125] The inhibition of jack bean urease by acetohydroxamate was monitored

with real-time assays of urease activity *in vitro*.[125] By monitoring the decomposition of hyperpolarized substrate ^{13}C-urea catalyzed by enzyme urease at varying concentrations of inhibitor acetohydroxamate, an IC_{50} value of acetohydroxamate against urease was obtained. The IC_{50} value was then used to estimate dissociation constant of urease-urea complex.

Protein-Solvent Interactions

Protein-solvent interactions have been extensively studied to investigate macromolecules. On the basis of intermolecular interactions, such as protein-water interactions, spin magnetization of a small molecule is transferred to a target macromolecule through chemical exchange of labile protons, as well as cross relaxation due to NOE.[124,126–129] NMR based measurements of exchange or cross relaxation rates indicates such interaction and provides structural information of macromolecules. The advent of D-DNP enhanced NMR technique provides new opportunities for measuring protein-water interactions. If a highly non-equilibrium spin state for ^{1}H nuclei of water is created by hyperpolarization, the transferred polarization from protons of water to labile protons of proteins due to exchange or cross relaxation processes is also significantly enhanced.[129] In consequence, the enhanced sensitivity of nuclei in proteins enables to record NMR data in a single scan, opening the possibilities to quantify exchange and cross relaxation rates as well as study transient phenomenon, such as dynamic processes of proteins.[129]

Harris observed polarization transfer from hyperpolarized water to exchangeable proton resonances of amino acids on proteins. The ^{1}H enhancement was further passed on

to nitrogen atoms on side-chain and backbone through one-bond Overhauser effect. The enhanced biomolecular sensitivity opens the possibility to investigate biomolecular dynamic processes.[126] Kim measured a pH dependence of transferred signals to the protein trypsin from hyperpolarized water. Maximum enhancements of 47 and 2.5 were observed in the amide and aliphatic proton at pH 7.5, respectively. Based on proposed two- and three-site models, average exchange and cross-relaxation rates were quantified from the enhanced amide and aliphatic proton signals. The method provides potential application to the study of protein structural changes, as well as other protein-solute interactions.[129] Olsen reported a study that explored the use of hyperpolarized water to enhance the sensitivity of nuclei in biomolecules.[128] Based on intermolecular NOE effect, protons on labile amide backbone and sidechain groups of biomolecules underwent fast exchanges with hyperpolarized protons of water.[128] Such proton exchange process results in a polarization enhancement of the protons of biomolecules. The ^{1}H enhancement was further passed on to nitrogen atoms through one-bond Overhauser effect. By maximizing T_1 relaxation of water using D_2O/heptane solvent mixture as dissolution solvent and employing rapid sample injection technique, the polarization of water was largely preserved during sample transfer process. 2D SOFAST-HMQC[130,131] ^{1}H-^{15}N correlation spectra were collected after injection hyperpolarized water into an alanine sample and a ^{15}N labeled aldehyde reductase sample. Enhancements of ~100 and ~330 were achieved for ^{15}N nuclei on amine group of alanine and amide group of aldehyde reductase. It was proposed that the sensitivity of nuclei in biomolecules could be further enhanced by

increasing the polarization level of water protons in the solid state and reducing dilution of water protons during dissolution process.

1.4.5 Protein Folding

The characterization of protein folding and unfolding is important for understanding regulation of biological activity. Protein folding occurs on a timescale that cannot be captured by most conventional NMR methods.[132] The significantly enhanced liquid state NMR signals by D-DNP facilitate the study of protein structural changes during folding or unfolding processes. Chen reported that the refolding of a ribosomal protein L23 was monitored following a pH jump.[132] L23 was hyperpolarized and dissolved with denaturing buffer. Its subsequent mixing with a high pH buffer in an NMR tube triggered the folding. The increased intensities in carbonyl regions, denoted as the characteristic of a folded protein, were visualized in time-resolved spectra. The signal intensities were fitted to a kinetic model based on a two-state folding mechanism where the folding rates were extracted. The site specific information was also obtained for methyl groups (Ile $C^{\delta 1}$) with resolved chemical shifts. The experiment demonstrated identification of intermediate states on a folding pathway or protein folding kinetics is feasible if ^{13}C relaxation rates of large polypeptides are on the order of seconds.[132]

The principle that signals of proton resonances on a protein can be selectively enhanced due to protein-solvent interactions via intermolecular NOE was utilized to monitor protein conformational change. Kurzbach presented the enhanced signals of amide protons on a protein Osteopontin (OPN) due to fast exchange with hyperpolarized HDO enabled monitoring conformational change of OPN induced by a ligand heparin near

physiological conditions.[133] The long lifetime of the hyperpolarized HDO proton (~29 s) made the acquisition of ^{15}N-^{1}H correlation spectra (~19 s) possible. The selectively enhanced signal through exchange with HDO solved the problem of peak overlap and broadening. Therefore, signals that were invisible in conventional correlation methods could be assigned in hyperpolarized correlation spectra. Upon heparin binding to OPN, new cross peaks emerged in the spectra.[133] The changed signal intensities in the glycine regions indicated accelerated or decreased exchange rates due to conformational change of OPN upon binding to heparin.

Ragavan demonstrated the real-time observation of ^{13}C DNP enhanced NMR signals during p27 folding upon binding to Cdk2/cyclin A on a time scale of several seconds, providing evidence for a structural change of p27 associated with the interaction with Cdk2/cyclin A.[134] Comparing ^{13}C NMR spectra of hyperpolarized p27 with and without admixing of Cdk2/cyclin A complex, higher signal intensities of ^{13}CO groups in samples of hyperpolarized p27 mixed with Cdk2/cyclin A complex was observed which indicated the formation of α-helical secondary structures. Since a series of spectra were recorded in non-equilibrium processes, the observation of increased signal intensities indicated p27 mixed with Cdk2/cyclin A was partially folded into α-helical secondary structures during the DNP measurement.[134] The series of spectra obtained from samples with and without Cdk2/cyclin A complex were analyzed by fitting intensities of spectra at each chemical shift.[134] From the fit, decay rate constants were obtained. The sample with Cdk2/cyclin A complex showed a reduced decay rate in the region from predominantly a-helical secondary structure.[134] This result was consistent with the assumption that a bound

α-helix experienced a slower spin-lattice relaxation.[134] By calculating expected relaxation rates for ^{13}C spins as a function of the rotational correlation time, the calculated relaxation rates were higher than the folding rate from the literature indicated that the observed signal changes were dominated by relaxation.[134]

1.5 Topics Focused in the Present Dissertation

The focus of the present dissertation is the application of fast correlation methods with D-DNP to identify molecular structures and characterize physical parameters, such as diffusion and spin relaxation, with the goal of investigating reaction kinetics and mechanisms as well as studying membrane transport of metabolite. Our experiments involve determination of heteronuclear chemical shift correlations in single scan, NMR spectra under off resonance decoupling by SHOT pulses, identification of diffusion and T_2 behavior of small molecules in solution, as well as intra- vs. extracellular metabolites in cancer cells using hyperpolarized UF-LNMR.

In heteronuclear chemical shift correlation experiments, off resonance decoupling using SHOT pulses causes a user-defined dependence of the observed *J*-splitting. By determining the *J*-splitting constants, [^{13}C, ^{1}H] chemical shift correlations were calculated. The ability to obtain the correlations in single scans makes this method ideal for determination of chemical shifts in on-going reactions, with the goal of determining the identity of transient species and reaction mechanisms.

Physical parameters of molecules, such as diffusion and spin relaxation, were further characterized by fast correlation methods. Ultrafast diffusion-T_2 correlation Laplace NMR enables one to correlate spin-spin relaxation and diffusion parameters in a

single-scan. Besides reducing the experiment time to a fraction, it significantly facilitates the use of nuclear spin hyperpolarization to boost experimental sensitivity, because the time consuming polarization step does not need to be repeated. Diffusion-T_2 correlation data was acquired by detecting hyperpolarized ^{13}C / ^{1}H signals of small molecules, and maps were generated using inverse Laplace transform. The experiments were performed in homogeneous field using a 400 MHz NMR magnet or inhomogeneous field using a 13.24 MHz single sided magnet. The accurate determination of diffusion and T_2 relaxation in both fields demonstrated the robustness of the method. The usability of hyperpolarized UF-LNMR is then demonstrated in the context of cell metabolism, by investigating the conversion of pyruvate to lactate in the cultures of mouse 4T1 cancer cells. We show that ^{13}C ultrafast diffusion-T_2 relaxation correlation measurements, with the sensitivity enhanced by several orders of magnitude by D-DNP, allow the determination of the extra- *vs.* intracellular location of metabolites in the cells. A significant difference both in observed diffusion coefficient and T_2 parameters indicates the ability to distinguish these pools.

CHAPTER II

REACTION MONITORING USING HYPERPOLARIZED NMR WITH SCALING OF HETERONUCLEAR COUPLINGS BY OPTIMAL TRACKING*

2.1 Introduction

Hyperpolarized nuclear spin states now can be quite readily created for liquid state samples using technology such as D-DNP.[29] The resulting signal gain of several orders of magnitude in a single scan or a series of scans in rapid succession, provides new impetus for the application of NMR to the study of non-equilibrium processes using stopped-flow techniques[34,115,117]. With its high sensitivity to structural change, NMR spectroscopy in particular assisted by hyperpolarization offers the promise of enabling the characterization of short-lived species in chemical and biochemical reactions[110,116]. At the same time, the rapid time evolution in stopped-flow experiments precludes the application of the traditional multi-dimensional NMR techniques that allow for the determination of chemical shift correlations, which often are crucial structural indicators.[1] As such, stopped-flow NMR *a priori* lacks access to one of the most powerful types of information available from NMR spectroscopy. Various methods however allow fully or partially recovering this information. Complete multi-dimensional data sets can be acquired in a single scan by spatial encoding of indirect dimensions, by the use of pulsed field gradient based techniques[45,48,49]. In a small number of scans, combinatorial selective excitation suc-

*Part of this chapter is reprinted with permission from Zhang, G.; Schilling, F.; Glaser, S. J.; Hilty, C. (2016). "Reaction monitoring using hyperpolarized NMR with scaling of heteronuclear couplings by optimal tracking" *J. Magn. Reson.* 272: 123-128, copyright 2016 Elsevier, and Zhang, G.; Schilling, F.; Glaser, S. J.; Hilty, C. (2013). "Chemical Shift Correlations from Hyperpolarized NMR Using a Single SHOT" *Anal. Chem.* 85(5): 2875-2881, copyright 2013 American Chemical Society.

-h as in Hadamard spectroscopy likewise can be used to explore a second spectral dimension[51,135]. Chemical shift correlations are further available from off-resonance decoupling, which imparts a change in observed *J*-splitting dependent on the chemical shift of an indirectly observed nucleus.[136,137] In off-resonance decoupling, a radiofrequency field is applied at the frequency of one type of nucleus during the acquisition of a one dimensional spectrum of a second type of nucleus. Based on the magnitude of the observed residual coupling constants, correlation information can be constructed by calculating the difference in chemical shift between the irradiation frequency and the actual frequency of the coupled spin. Previously, off-resonance continuous wave (CW) decoupling in conjunction with D-DNP was proposed as a way of obtaining heteronuclear chemical shift correlation.[52] In CW off-resonance decoupling, the effective scaling of the scalar coupling constant is a nonlinear function of frequency offset.[138] In consequence, the accuracy of the calculated chemical shift for any spin is strongly dependent on the chosen decoupling frequency.

In remedy of this drawback, an efficient optimization technique for generating hetero-nuclear decoupling sequences[139–141] was developed, based on principles of optimal control theory.[142,143] This highly flexible approach makes it also possible to design decoupling sequences that produce a pre-defined chemical shift dependence of the observed multiplet splitting. Pulses developed by this method, termed Scaling of Heteronuclear Couplings by Optimal Tracking (SHOT), have been demonstrated to allow reliable determination of chemical shifts combined with rapid implementation once pulses have been calculated.[46,140] When applied to stopped-flow NMR techniques, a major

advantage of SHOT based determination of indirect chemical shift is the need for only a single scan to determine the chemical shift from all offset frequencies. Pulses that exhibit a piecewise linear dependence of the scaled *J*-splitting on chemical shift have subsequently been used in combination with dissolution dynamic nuclear polarization.

Here, we demonstrate the application of SHOT pulses to obtain chemical shift correlations from D-DNP hyperpolarized samples. [^{13}C, ^{1}H] chemical shift correlations of vanillin were reconstructed via off-resonance decoupling by SHOT pulses. Specifically, we demonstrate the calculation of ^{1}H chemical shifts from a series of ^{13}C spectra acquired of a transient carbanionic species in a catalyzed polymerization reaction of styrene. In addition, we extend the capability of SHOT pulses to allow for the scaling of *J*-splittings larger than the actual *J*-coupling constant. Subsequently, we evaluate the accuracy of the indirect chemical shift determination as a function of changing signal-to-noise ratio in these data sets.

2.2 Experimental Section

2.2.1 Dynamic Nuclear Polarization

For DNP experiments of vanillin, a 10 μL sample of 2 M vanillin was dissolved in 28% D_2O and 72% DMSO-d_6 or 28% H_2O and 72% DMSO for ^{1}H or ^{13}C experiments, respectively. The sample was mixed with 15 mM 4-hydroxy-2,2,6,6-tetramethylpiperidine-1-oxyl (TEMPOL) free radical (Sigma-Aldrich, St. Louis, MO) for ^{1}H experiments or tris[8-carboxy-2,2,6,6-tetrakis(2-hydroxyethyl)benzo[1,2-d:4,5-d′]bis[1,3]-dithiol-4-yl]methyl free radical sodium salt (OX63; Oxford Instruments, Tubney Woods, U.K.) for ^{13}C experiments. For DNP experiments of the catalyzed

polymerization of styrene or the reaction of p-anisaldehyde, a 40 μL or 25 μL sample of the reactant styrene or p-anisaldehyde, which both are self-glassing, was mixed with 15 mM of the free radical α,γ-Bisdiphenylene-β-phenylallyl (BDPA; Sigma-Aldrich, St. Louis, MO). The sample was hyperpolarized on ^{1}H for 30 mins at 1.4 K in a HyperSense system (Oxford Instruments, Abingdon, UK), by irradiating microwaves (100 mW) at a frequency of 94.005 GHz in a 3.35 T magnetic field. Hyperpolarized on ^{13}C was performed using an irradiation frequency of 93.974 GHz or 93.965 GHz for samples containing OX63 radicals or BDPA radicals, an irradiation time of 3 hours and a microwave power of 60 mW. Subsequently, the hyperpolarized sample was quickly dissolved in pre-heated acetonitrile, dioxane or trifluoroethanol (Alfa Aesar, Ward Hill, MA), and injected rapidly into a 5 mm NMR tube installed in an NMR instrument (Bruker Biospin, Billerica, MA) by a gas driven injection device[33] at a temperature of 298 K-300 K. Because the polymerization reaction is sensitive to oxygen and water, the transfer line in the DNP polarizer, the injection system and the NMR tube were purged with nitrogen gas before preloaded the catalyst solution. In the NMR tube, the hyperpolarized sample was mixed with 35 μL catalyst solution or 25 μL isobutylamine (Alfa Aesar, Ward Hill, MA) for hyperpolarized samples of styrene or p-anisaldehyde. The catalyst solution is sodium naphthalenide, which was prepared by dissolving 0.5 g sodium film and 2 g naphthalene in 10 mL tetrahydrofuran (THF) solution and sonicated for 5 min at a temperature of 298 K.

2.2.2 SHOT Pulses

The SHOT pulses are developed by Dr. Schilling and Dr. Glaser at Technical University of Munich. SHOT pulses are optimized such that observed *J*-splittings under off resonance decoupling by SHOT pulses (J_{SHOT}) depend linearly on frequency offset (ν).[46] Equation 2.1 describes this relationship, with the *J*-splitting varying between zero and $s_J \times J_{opt}$ for offsets between $-\nu_{max}$ and ν_{max},

$$J_{SHOT}(\nu) = s_J \times J_{opt} \frac{\nu + \nu_{max}}{2\nu_{max}} \tag{2.1}$$

Here, s_J is an arbitrary scaling factor that can also be larger than 1. For ^{1}H decoupling, a nominal coupling J_{opt} =160 Hz, a first pulse with s_J = 1 and ν_{max} = 1250 Hz was used, resulting in a maximal *J*-splitting of 160 Hz for $\nu = \nu_{max}$. A second pulse with a higher bandwidth ν_{max} = 2000 Hz and a scaling factor s_J = 1.5 was computed. For the case of s_J = 1.5, a maximum *J*-splitting of 240 Hz occurs at $\nu = \nu_{max}$ in the optimization algorithm, which is 50 % larger than the actual coupling constants of about J_{opt} = 160 Hz for which the SHOT was optimized. The maximum required radio frequency (rf) amplitudes $(\gamma/2\pi)B_{1,max}$ for the two pulses were 1.64 kHz and 2.1 kHz, respectively. For ^{13}C decoupling, J_{opt} =160 Hz, s_J = 1, ν_{max} = 7500 Hz and $(\gamma/2\pi)B_{1,max}$ = 3.51 kHz was used.

A SHOT pulse with a profile consisting of three linear segments of successively reversed direction ("zigzag profile") was also designed,[46]

$$J_{SHOT}(\nu) = \begin{cases} s_J \times J_{opt} \dfrac{\nu + \nu_{max}}{800Hz} & -\nu_{max} < \nu \leq -450Hz \\ s_J \times J_{opt} \left(1 - \dfrac{\nu + 425Hz}{800Hz}\right) & -425Hz < \nu \leq 375Hz \\ s_J \times J_{opt} \dfrac{\nu - 400Hz}{800Hz} & 400Hz < \nu \leq \nu_{max} \end{cases} \tag{2.2}$$

This pulse was used for ^{1}H decoupling with J_{opt} =160 Hz, s_J = 1, ν_{max} = 1250 Hz and $(\gamma/2\pi)B_{1,max}$ = 1.96 kHz.

For all SHOT pulses, the value for J_{opt} was chosen to lie within the typical range of direct heteronuclear carbon-proton couplings, and the SHOT off-resonance decoupling profile is very robust against deviations between the actual experimental coupling constants J_{opt}.[46]

Table 2.1. Setting parameters of SHOT pulses.

SHOT pulse	$(\gamma/(2\pi))B_{1,max}$ (kHz)	BW (Hz)	N_{dig}	T (ms)
SHOT_linear_2500Hz.txt	1.64	2500	1280	256
SHOT_zigzag_2500Hz.txt	1.96	2500	1280	256
SHOT_linear_15kHz.txt	3.51	15000	10240	256
Upscale_SHOT_4kHz.txt	2.10	4000	2560	256

For implementation of SHOT pulses on a spectrometer, all pulses are optimized for heteronuclear *J*-scaling assuming actual coupling constants of about J_{opt} = 160 Hz with individual scaling factors s_J set to either 1 or 1.5. The maximum RF amplitude $(\gamma/(2\pi))B_{1,max}$ must be calibrated to the value specified with the pulse (Table 2.1). The duration of data acquisition must be equal to (or shorter than) the SHOT pulse, and digitization points of the pulse are integer multiples *i* of the number of acquisition points $i \times N_{dig}$. Even though a SHOT pulse is initially calculated for a specific set of parameters, the maximum RF field $B_{1,max}$, the bandwidth BW, the pulse length *T*, and the optimized

scalar coupling constant $s_J \times J_{opt}$ can be moderately rescaled according to the relation $B_{1,max} \propto BW \propto s_J \times J_{opt} \propto T^{-1}$ (arbitrary scaling factors are possible if also the actual coupling constant is scaled accordingly).

2.2.3 NMR spectroscopy

For measuring hyperpolarized NMR spectra of vanillin, the pulse sequence for ^{13}C detected hyperpolarized experiments consisted of elements [(p1 – g1)3 – pe – acq – g2], and was repeated two times on a single hyperpolarized sample to measure a SHOT decoupled spectrum and an undecoupled spectrum. p1 is a selective π/2 pulse on the ^{13}C channel (EBURP shape, 10 ms duration), applied at the solvent resonance of DMSO (40.17 ppm). g1 (40.6 G/cm, 42.0 G/cm, 97.2 G/cm, 1 ms) is a pulsed field gradient applied along x, y and z axes to de-phase the coherences from the solvent signal. pe is a hard ^{13}C excitation pulse ($(\gamma/(2\pi))B_1$ = 29.41 kHz) applied with a flip-angle of π/4 in the first scan, and π/2 in the second scan in order to equally distribute signal. g2 (50 G/cm, 2.5 ms) is another pulsed field gradient applied along the z axis to remove the unwanted coherence from the previous acquisition. The pulse sequence for the ^{1}H detected experiment included additionally a filter element to remove ^{1}H coherence from atoms not coupled to ^{13}C. It consists of [pe – τ1 – p1 – τ2 – p2/p3 – g1/τ2 – p1 – g2/τ1 – acq – g3]. Parameters are similar to the ^{13}C detected experiments described above. The hard ^{1}H excitation pulse pe (small flip angle, see above) was applied with a field strength of $(\gamma/(2\pi))B_1$ = 22.22 kHz. p1 is a 90 degree hard pulse ($(\gamma/(2\pi))B_1$ = 29.41 kHz) applied on ^{13}C. p2 ($(\gamma/(2\pi))B1$ = 11.11 kHz) and p3 ($(\gamma/(2\pi))B1$ = 14.71 kHz) are 180 degree hard pulses applied simultaneously on the ^{1}H and ^{13}C channels for chemical shift refocusing.

Pulses p2 and p3 have a phase difference of π/2 compared to pe and the first p1 pulse. The second p1 pulse has a phase difference of π compared to the first p1 pulse. The time delay for the heteronuclear filter is τ1 = 1/(2*J*) = 3.57 ms. The pulsed field gradients for coherence selection are g1 (40.6 G/cm, 42.0 G/cm, 97.2 G/cm, 1 ms) and g2 (–30.5 G/cm, –31.4 G/cm, –74.3G/cm, 1 ms), applied along x, y and z axes. τ2 is a short time delay for stabilization after pulsed field gradients.

For reaction monitoring, the pulse sequence for ^{13}C detected hyperpolarized NMR experiments was (trigger – [G_z – α – acquire]$_{\times n}$). For the catalyzed polymerization of styrene, a total of n = 8 transients were acquired within 3 s. For the experiment with p-anisaldehyde, a total of n = 15 transients were acquired over a duration of 12 s. G_z was a pulsed field gradient (97 G/cm, 1 ms) applied for attenuation of coherences from previous scans. α was an excitation pulse of strength γB_1 = 28.57 kHz corresponding to a flip angle of 20 degrees for the styrene experiment or 13 degrees for the p-anisaldehyde experiment. In each scan, a total of 12,800 complex points (10 times the number of digitization points of the SHOT pulses) was acquired. During acquisition, ^{1}H off resonance decoupling by one of the two SHOT pulses was applied (s_J = 1 for the reaction with styrene and s_J = 1 or 1.5 for the reaction with p-anisaldehyde, see below). The acquisition time during each transient is 256 ms, which is the same as the SHOT pulse length. The SHOT pulse is applied once for each transient acquisition.

The proton and carbon chemical shifts of vanillin, the reactants and products were calibrated to the ^{1}H signal and ^{13}C signal of tetramethylsilane (TMS) at 0 ppm. For the experiments with vanillin, the transmitter frequency offsets to the frequency of 0 ppm were

2670.23 Hz and 13134.02 Hz on the ^{1}H and ^{13}C channel. A thermally polarized ^{1}H spectrum was acquired immediately after a hyperpolarized experiment to verify the actual ^{1}H chemical shifts. The ^{1}H chemical shifts for thermally polarized and hyperpolarized experiments were referenced to the solvent resonance of acetonitrile. The chemical shift of acetonitrile was calibrated to the ^{1}H signal of TMS at 0 ppm using a substitution method. Chemical shifts of ^{13}C were indirectly calibrated via the known ^{1}H calibration, using γ_C/γ_H = 0.25145020.[46,144] For the experiments with reaction monitoring, the transmitter frequency offset to the frequency of 0 ppm was 2286.02 Hz on the ^{1}H channel for the catalyzed polymerization reaction. The ^{1}H chemical shifts of the transient carbanionic site were verified from the ^{1}H spectrum acquired immediately after a DNP experiment, while the reaction was still progressing. The ^{1}H chemical shifts were referenced to the solvent resonance of dioxane. The chemical shift of dioxane was calibrated to the ^{1}H signal of TMS at 0 ppm using a separate sample. For the experiments with p-anisaldehyde, the transmitter frequency offset to the frequency of 0 ppm was 2729.23 Hz for the experiment with the pulse using s_J = 1 and 1908.63 Hz for the experiment with the pulse using s_J = 1.5 on the ^{1}H channel. To verify the actual proton chemical shifts, a proton spectrum was acquired immediately after a DNP experiment under the same experimental conditions. Because isobutylamine was in excess, the reactant was fully consumed. Therefore, the actual proton chemical shifts of the reactant peaks were verified using another sample, in which the concentration of p-anisaldehyde was the same as the concentration used in the DNP experiment.

Data was Fourier transformed and zero-filled to 65536 points or 131072 points and

an exponential window function was applied (line broadening of 10 Hz or 0 Hz) for the experiments with vanillin, styrene and p-anisaldehyde, respectively. Peak positions for each of the doublet peaks were picked using the Topspin 3 software (Bruker Biospin). Indirect ^{1}H chemical shifts were back-calculated based on Eq. (2.1) and (2.2).

2.3. Results and Discussion

2.3.1 Chemical Shift Correlations for a Molecule

Since vanillin contains several functional groups with various coupling constants and chemical shifts, it was selected as a model compound to evaluate the performance of the SHOT pulses. The expanded view of the spectra obtained from hyperpolarized experiments with and without SHOT decoupling is shown in Figure 2.1. Due to decoupling, the coupling constant of each peak in the upper panel was reduced by different amounts compared to the peaks without decoupling in the lower panel. The long-range ^{1}H-^{13}C couplings were also removed, resulting in increased peak heights. This feature helps to enhance signal amplitude in SHOT decoupling experiments.

Since ^{13}C has a large chemical shift dispersion, this property reduces peak overlap. The acquisition of ^{13}C spectra is more favorable than ^{1}H spectra. As shown in Figure 2.1c, peak 5 is partially overlapped with peak 7 and has a doublet split. All these features introduce additional errors for calculation of chemical shift correlation for atom 5. Additionally, ^{13}C has a relatively long T_1 relaxation time which helps to preserve hyperpolarization. On the other hand, the large gyromagnetic ratio and ~100% natural abundance of ^{1}H provides larger absolute signal than ^{13}C.

Since SHOT pulses were optimized to cover the whole frequency range of the coupled ^{1}H or ^{13}C spins, [^{13}C, ^{1}H] chemical shift correlations for all peaks can be calculated from SHOT decoupled spectra. From the *J*-splittings measured in each 1D ^{13}C / ^{1}H spectrum (Fig. 2.1), the correlated ^{1}H / ^{13}C chemical shifts were determined as $10^6(\nu_{trans} + \nu)/\nu_0$, where ν_0 is the frequency corresponding to 0 ppm on the decoupling channel, ν_{trans} is the decoupler offset from ν_0, and ν is derived from Eq. (2.1) and (2.2).[46] The calculation results are shown in Table 2.2 and 2.3.

Table 2.2. ^{1}H chemical shift calculation from hyperpolarized ^{13}C spectrum in Figure 2.1a and b with ^{1}H SHOT pulse with a linear profile ($s_J \times J_{opt}$ = 160 Hz) and a zigzag profile.

		SHOT pulse with a linear profile			SHOT pulse with a zigzag profile		
^{13}C group	δ^1H /ppm	J_{SHOT}/J_{opt}	δ^1H_{linear} /ppm	Δδ /ppm	J_{SHOT}/J_{opt}	δ^1H_{zigzag} /ppm	Δδ /ppm
1	9.809	1.01	9.833	-0.024	1.06	9.798	0.011
5	7.448	0.62	7.449	-0.001	0.08	7.440	0.008
6	7.000	0.55	7.001	-0.001	0.31	6.988	0.012
7	7.436	0.62	7.429	0.007	0.09	7.429	0.007
8	3.931	0.06	3.909	0.022	0.18	3.920	0.011

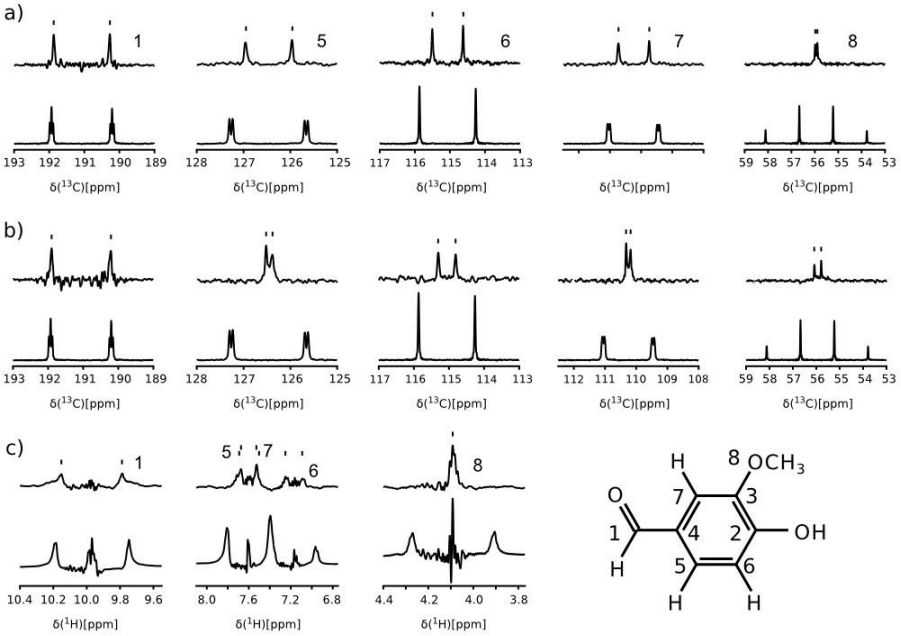

Fig. 2.1. Expanded views of hyperpolarized vanillin peaks obtained from SHOT decoupling experiments with (upper trace) and without (lower trace) SHOT decoupled spectrum in each panel. a) ^{13}C detected experiment with ^{1}H decoupling using SHOT pulse with a linear profile ($s_J \times J_{opt}$ = 160 Hz). b) ^{13}C detected experiment with ^{1}H decoupling using SHOT pulse with a zigzag profile. c) ^{1}H detected experiment with ^{13}C decoupling. Marks above peaks indicate the position used to determine scaled *J*-splitting.

Table 2.3. ^{13}C chemical shift calculation from hyperpolarized ^{1}H spectrum in Figure 2.1c with ^{1}H SHOT decoupling.

^{1}H group	$\delta^{13}C$ / ppm	J_{SHOT}/J_{opt}	$\delta^{13}C_{linear}$ / ppm	$\Delta\delta$ / ppm
1	191.37	0.91	191.49	-0.12
5	126.70	0.47	126.58	0.12
6	115.17	0.40	115.54	-0.37
7	110.31	0.37	110.58	-0.27
9	56.00	0.00	56.00	0.00

The accuracy of this method is evaluated by comparing the calculated chemical shifts with the actual chemical shifts obtained from a thermally polarized spectrum of vanillin under the same conditions. The error of the calculated chemical shifts is [-0.03 ppm, 0.03 ppm] and [-0.4 ppm, 0.4 ppm] for indirectly determined ^{1}H and ^{13}C chemical shifts, respectively. Since $\Delta J_{SHOT}/\Delta\nu$ is larger for the SHOT pulse with a zigzag profile, this property provides a higher sensitivity of the calculated chemical shifts with respect to the measured *J*-splitting.

The SHOT pulse with a zigzag profile consists of three intervals for ^{1}H decoupling. A prior knowledge about which intervals a chemical shift falls into is needed for calculating the indirect ^{1}H chemical shift. This knowledge may be obtained from a known ^{13}C chemical shift or by observing changes in chemical shifts of a known compound.

As shown in Figure 2.1, sidebands are observed close to all partially decoupled peaks in the experiments. These sidebands produced by SHOT decoupling pulses stem from a systematic noise source.[46,140] Since signal amplitudes of the sidebands are well below the amplitudes of the peaks, they do not cause problems for determining chemical shift correlations. However, the sidebands result in a reduction of signal to stochastic noise ratio. The effect is balanced by the reduced amount of signal loss due to spin-lattice relaxation of the later scans in continuous wave decoupling or alternative experiments, such as sequentially acquired two-dimensional spectra which requires a large number of points (~32) in the indirect chemical shift dimension.[145] Single-scan ultrafast multi-dimensional spectroscopy, where signal acquisition in subvolumes of a sample relies on gradient encoding, does not have this problem. However, a noise penalty has to be paid

due to a required increase in receiver bandwidth.[46,48] SHOT decoupling use entire hyperpolarized signal in a single scan without the need of pulse field gradients, avoiding the potential for signal loss due to incomplete focusing.

In contrast to SHOT decoupling which has consistent accuracy for any chosen offsets, continuous wave (CW) off resonance decoupling suffers increased inaccuracy for large offsets which requires the acquisition of spectra with 4 different chemical shift offsets and a reference spectrum.[46,52] However, splitting a single hyperpolarized signal by 5 fold decreases the signal to stochastic noise ratio in each scan and the time needed for obtaining multiple spectra reduces the utility of the method to real-time spectroscopy.[46] A simulation by Schilling *et al.* shows that SHOT decoupling is robust to *J* variations, implying the actual *J* does not need to be known for calculation of the indirect chemical shift.[46] Therefore, the chemical shift of a nucleus decoupled by a SHOT pulse can be calculated from a single 1D spectrum, this technique would open the possibility for determining chemical shift correlations in non-equilibrium samples.

2.3.2 Chemical Shift Correlations for Non-equilibrium Samples

An advantage of using SHOT pulses to determine chemical shift correlations in non-equilibrium processes is the ability of characterizing structures of species arising transiently from a reaction. This property facilitates the elucidation of reaction mechanisms. To evaluate the performance of the SHOT pulse for this purpose, the anionic polymerization of hyperpolarized styrene was studied as a model reaction using $\{^{1}H\}$ ^{13}C NMR.[146,147] In this reaction, the coupling constants of the peaks of both the reactant and the generated species with carbanionic active site range from 160 Hz to 154 Hz, which is

within the optimized *J*-splitting range of the SHOT pulse. Series of 1D ^{13}C spectra during this reaction were acquired with the ^{1}H SHOT pulse, as shown in Fig. 2.2a. In these spectra, ^{13}C signals from the transient carbanionic site, where monomer addition to the nascent polymer chain occurs, can be identified as 1', 2', 3'b, 4', 5'a and 5'b. Based on the observed *J*-splittings of these ^{13}C peaks, the correlated ^{1}H chemical shifts were calculated using Eq. (2.1).[46] For example, the peaks of C5'a and C5'b of the first scan in Fig. 2.2a stem from the phenyl ring of the transient carbanionic species. These peaks show observed *J*-splittings J_{SHOT} = 67 Hz and J_{SHOT} = 75 Hz. The resulting ^{1}H chemical shifts are calculated as 5.21 ppm and 5.51 ppm, respectively. The correlated ^{1}H chemical shifts for all of the ^{13}C atoms are shown in Table 2.4.

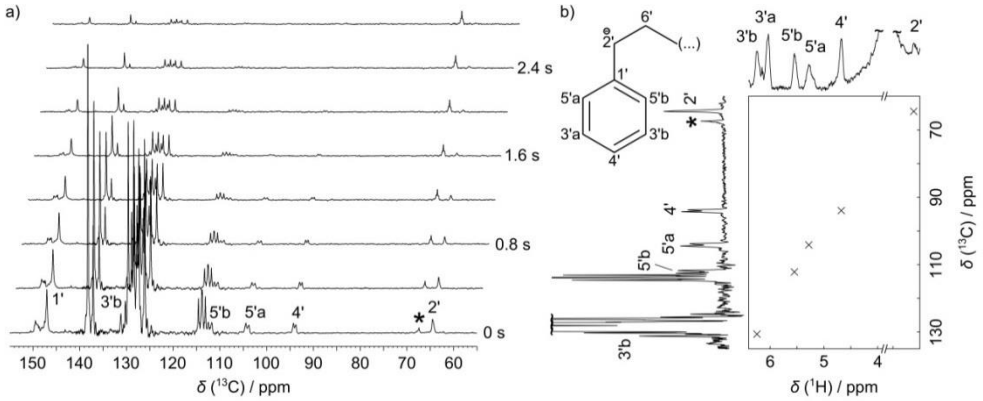

Fig. 2.2. a) Stacked plots of a series of ^{13}C spectra from hyperpolarized styrene mixed with polymerization initiator $NaC_{10}H_8$, acquired with the ^{1}H SHOT pulse of J_{opt} = 160 Hz and s_J = 1. The dioxane solvent peak is designated with an asterisk. The first 8 scans of the spectra at time intervals of 400 ms are shown. b) 2D representation of chemical shifts calculated from the first scan of (a), that correlates a 1D hyperpolarized ^{13}C spectrum and thermal ^{1}H spectrum measured separately. The labeled ^{13}C and ^{1}H resonances correspond to the carbanionic active polymerization site.

Since the SHOT pulse is applied for each scan, the ^{1}H chemical shifts of the carbanionic species in the indirect dimension can be calculated for each time point. In this reaction, large scan-to-scan chemical shift changes are not expected. Accordingly, for instance the ^{1}H chemical shifts of the peak of C4' in the first four scans at time points 0, 0.4, 0.8 and 1.6 s, are calculated as 4.68, 4.66, 4.63 and 4.63 ppm, corresponding to a variation of less than 20 Hz.

Table 2.4. ^{1}H chemical shift calculation of the carbanionic intermediate from the first scan of the hyperpolarized ^{13}C spectrum of the polymerization reaction with ^{1}H SHOT pulse of $s_J \times J_{opt}$ = 160 Hz in Figure 1a.

^{13}C group	$\delta(^{13}C)$ (ppm)	J_{SHOT} (Hz)	$J_{SHOT} / s_J \times J_{opt}$	$\delta(^{1}H_{cal})$ (ppm)	$\delta(^{1}H_{real})$ (ppm)	$\Delta\delta(^{1}H)$ (ppm)
2'	64.5	0	0.00	2.59	2.60	-0.01
3'b	130.7	95	0.60	6.30	6.25	0.05
4'	94.0	53	0.33	4.68	4.67	0.01
5'a	104.1	67	0.42	5.21	5.27	-0.06
5'b	112.1	75	0.47	5.51	5.55	-0.04

To illustrate the use of these correlations for chemical shift assignment, a 2D representation of the data obtained from this experiment is plotted in Fig. 2.2b. Here, a hyperpolarized ^{13}C and a thermal ^{1}H 1D spectrum are correlated by placing cross marks at the chemical shifts calculated from the SHOT experiment. This representation is intended to resemble a familiar 2D NMR spectrum, even if acquired from hyperpolarized

^{13}C spins. Since this correlation is calculated from the 1D SHOT spectrum, it does not increase the resolution as a conventional 2D NMR data set would. This limitation can be seen in peak 3'a, which is shown in the proton spectrum but is not observed in the hyperpolarized ^{13}C spectrum because it is overlapped with the monomer peaks.[148] However, a SHOT based correlation spectrum is available in each scan in a time resolved data set.

Previous DNP experiments that enabled measurement of the kinetics of this styrene polymerization reaction did not allow the determination of ^{1}H chemical shifts from the same data set.[116] Rather, the origin of transient peaks were identified based on known chemical shifts, as well as the correlation of signals between the reactant and the reaction product through selective inversion experiments. However, with the SHOT pulse, as shown here, the correlation could be obtained within seconds. These chemical shift correlations greatly facilitate the assignment of peaks in such transient DNP-NMR spectra, while retaining the ability for kinetic measurements based on peak intensities and for detecting species arising transiently during a reaction.

The power of off-resonance decoupling by SHOT pulses for chemical shift determination derives from the ability to define an arbitrary dependence between the frequency offset of the decoupled nucleus and the *J*-splitting of the detected nucleus. With the *J*-splittings obtained from a pulse that yields a maximum splitting of 160 Hz (Fig. 2.3),[46] the peaks of the carbanionic species are resolved in the spectra styrene polymerization. However, in the general application it is expected that peak shifts due to the decoupling result in signal overlap for a certain proportion of spectra. Signal overlap

in such a case could however readily be avoided by scaling to different *J*-splittings. Here, we extend the repertoire of SHOT pulses with a design that can scale a *J*-splitting to a value that is larger than the original *J*-coupling constant. In this case, we chose $s_J \times J_{opt}$ = 240 Hz, which is about 50 % larger than typical $^{13}C - {}^{1}H$ coupling constants. The larger slope of $\Delta J_{SHOT} / \Delta \upsilon$ of the new pulse (Fig. 2.3b) increases the sensitivity of the chemical shift determined in the indirect dimension. The relationship between the frequency offset and J_{SHOT} of this pulse was chosen to be a linear function (Eq. (2.1)), as was the case for the previously used pulse. This linear relationship is intended to provide a uniform slope and hence a uniform precision of the chemical shift determination in the indirect dimension and in addition facilitate data analysis. The simulated frequency profiles of the two pulses are compared in Fig. 2.3a. The two branches in the figure represent the contour lines from the peaks of the doublet of two heteronuclear coupled spins, when the decoupling pulse is applied at the frequency offset indicated on the vertical axis. Because of the robustness of SHOT pulses to *J* variation,[46] the simulated frequency profiles for actual coupling constants ranging from 174 Hz to 145 Hz show little variation in the decoupling pattern of SHOT pulses (Fig. 2.3a). Application of off-resonance decoupling to molecules with a different range of actual coupling constant is possible but would require re-optimisation of the pulses to the actual range of coupling constants.

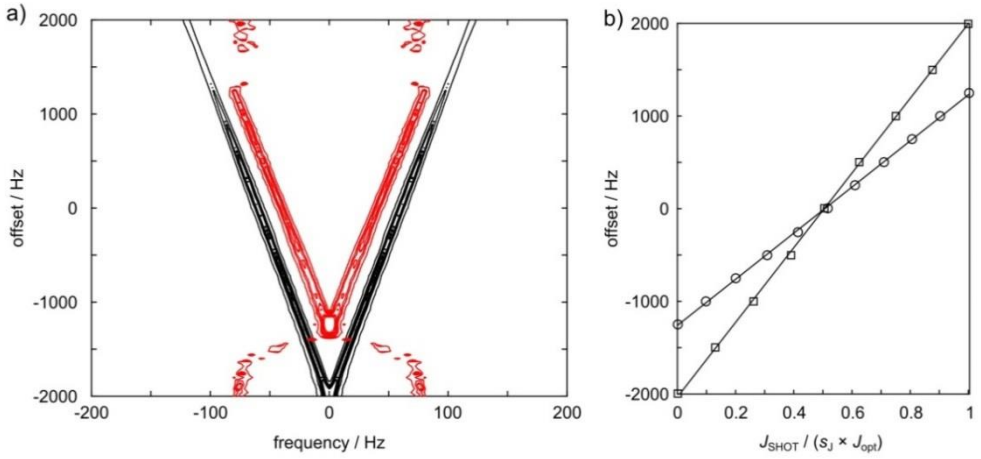

Fig. 2.3. a) Contour plot of the simulated frequency profiles of the SHOT pulses with J_{opt} = 160 Hz and s_J = 1 (red) or s_J = 1.5 (black) as a function of the transmitter offset frequency. The frequency profiles are simulated for actual coupling constants ranging from 174 Hz to 145 Hz (in steps of 1 Hz). Contour levels are at [0.2, 0.3, 0.35, 0.4, 0.45, 0.5] of the maximum decoupled peak amplitude. When the spins are not in the optimized bandwidth, the pulse with s_J = 1 shows a non-defined off-resonance decoupling pattern. This figure was made by Dr. Schilling at Technical University of Munich. b) The theoretical *J*-splitting values determined from Eq. (2.1) (solid lines) and the observed *J*-splitting values as a function of the ^{1}H off resonance decoupling offset using SHOT pulses with s_J = 1 (circles) and s_J = 1.5 (squares) for the aldehyde group (J_{actual} = 174 Hz) of p-anisaldehyde, measured on a 400 MHz NMR spectrometer.

For comparison, the experimental performance of the SHOT pulses was measured using a concentrated sample of p-anisaldehyde, without DNP hyperpolarization (Fig. 2.3b). The observed *J*-splittings (J_{SHOT}) for the aldehyde signal, which has an actual *J*-splitting of 174 Hz, are plotted as a function of transmitter frequency offset in the indirect ^{1}H dimension. The linear dependence of the observed *J*-splitting on the transmitter offset can be seen as designed. In the case of the SHOT pulse with $s_J \times J_{opt}$ = 160 Hz, all of the observed *J*-splittings represent an apparent down-scaling of the actual coupling constant, as would normally be expected in an experiment employing off-resonance decoupling.[149]

However, for the pulse with $s_J \times J_{opt}$ = 240 Hz, the two points with highest offset represent an apparent up-scaling of the actual coupling constant.

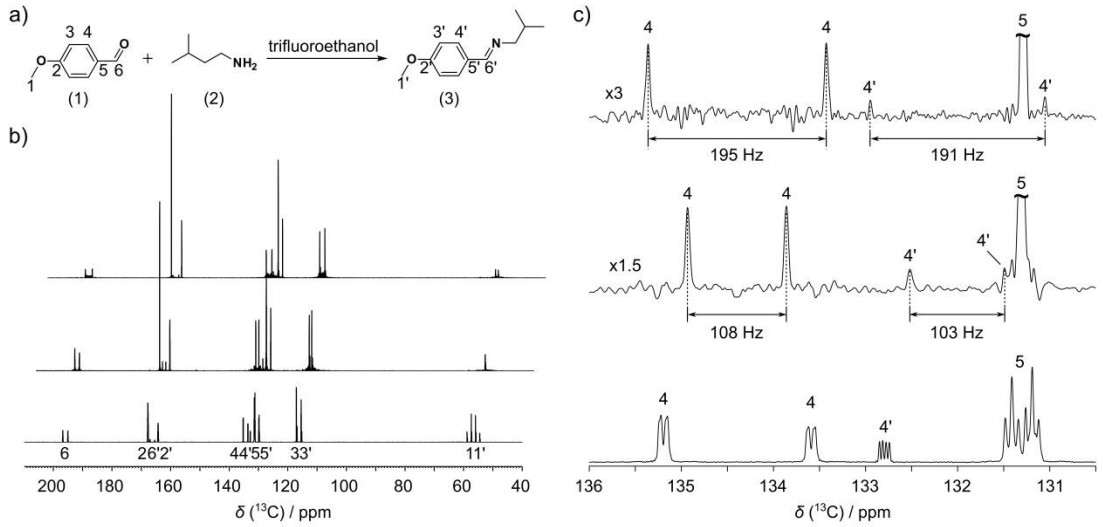

Fig. 2.4. a) The chemical reaction between p-anisaldehyde (1) and isobutylamine (2) using trifluoroethanol as solvent. b) Hyperpolarized ^{13}C NMR reference spectrum without decoupling (bottom), with ^{1}H SHOT pulses of J_{opt} = 160 Hz and s_J = 1 (middle) or s_J = 1.5 (top). c) Expanded views of (b) are shown for peak 4, 4' and 5.

The difference between the two pulses is seen in the reaction between p-anisaldehyde and isobutylamine, where a Schiff base N-(4-methoxybenzylidene)-2-methylpropan-1-amine is formed (Fig. 2.4a). The spectra from the third scan with two different SHOT pulses, as well as one spectrum without decoupling, are shown in Fig. 2.4b, and are expanded around peak 4 in Fig. 2.4c. (see also Fig. 2.5 for the whole spectra and Fig. 2.6 for expanded views of peak 1, 1', 3, 3', 6, 6'). Here, one of the C4' peaks overlaps with C5 both in the spectrum without decoupling, as well as in the decoupled spectrum using the pulse with $s_J \times J_{opt}$ = 160 Hz. This overlap is resolved by the larger

observed *J*-splitting of 191 Hz when using the pulse with $s_J \times J_{opt}$ = 240 Hz. According to Eq. (2.1), the ratio of the observed *J*-splittings of the same ^{13}C peak in the decoupled spectra (top and middle) depends on their individual s_J, ν_{max} and frequency offset (ν) which is the difference between the calculated ^{1}H frequency and transmitter frequency. For instance, the frequency offsets of C4 are ν = 1256 Hz (top) and 436 Hz (middle). With ν_{max} = 2000 Hz (top) or 1250 Hz (middle) and s_J = 1.5 (top) or 1 (middle), the calculated J_{SHOT} ratio of C4 in the top and middle spectrum is 1.8 as observed in Fig. 2.4c.

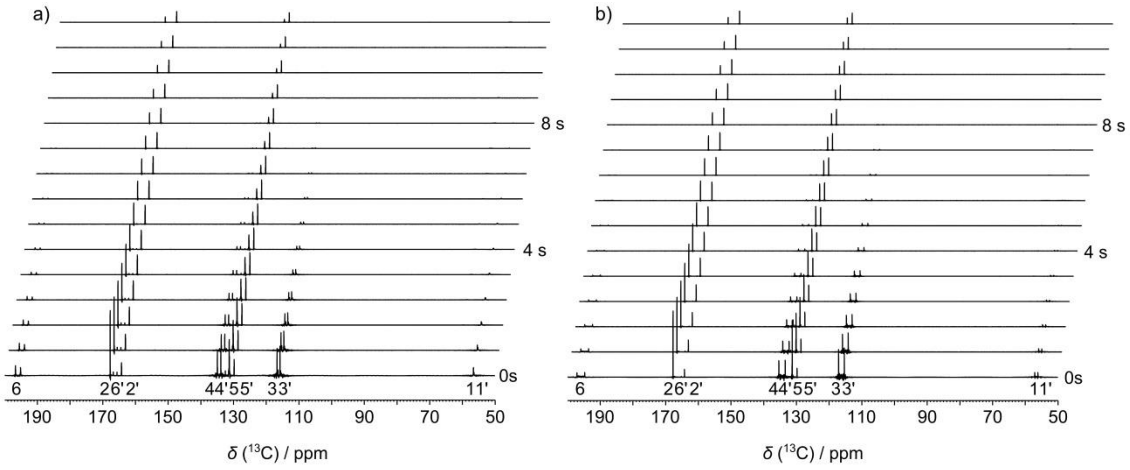

Fig. 2.5. Stacked plots of series of ^{13}C spectra from hyperpolarized p-anisaldehyde and isobutylamine with ^{1}H SHOT pulses (a) $s_J \times J_{opt}$ = 160 Hz; (b) $s_J \times J_{opt}$ = 240 Hz. The ^{13}C resonances from left to right correspond to atom number 6, 2, 6', 2', 4, 4', 5, 5', 3, 3', 1, 1' (for expanded view, see Figure 3c and S2). The data acquisition includes a total of 15 transients with a time interval of 800 ms between each transient.

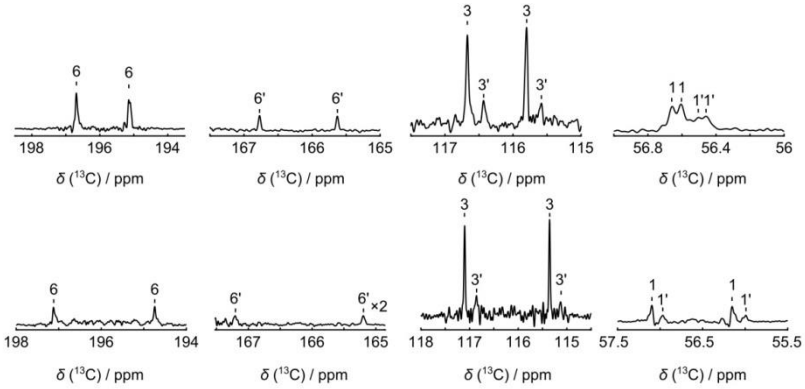

Fig. 2.6. Expanded views of the peaks obtained from the reaction of Figure 3a with ^{1}H SHOT pulses ($s_J \times J_{opt}$ = 160 Hz, upper panel; $s_J \times J_{opt}$ = 240 Hz, lower panel). From left to right, the different spectra represent ^{13}C atom number 6, 6', 3, 3', 1, 1'. Marks above peaks indicate the position used to determine scaled *J*-splitting J_{SHOT}.

The increased *J*-splitting appears at the expense of also increased spurious signals ("sidebands"), which add to the apparent noise in the spectrum. In Fig. 2.4c, the apparent signal to noise ratio (SNR) for C4 (inset) near the peak with the pulse of $s_J \times J_{opt}$ = 240 Hz and with the pulse of $s_J \times J_{opt}$ = 160 Hz are calculated as 20 and 25, respectively. Because of the side band signals, the SNR away from the peak which are SNR_{240} = 421 and SNR_{160} = 771 is larger than the apparent SNR near the peak for C4. These side band signals however scale with the main peak intensity, without degrading the limit of detection for the peak observed. For this reason, the apparent SNR of the C4 peak is stable for both pulses from scan 1 to scan 7, with values of 19.5±0.5 for the pulse with $s_J \times J_{opt}$ = 240 Hz and 24.5±0.5 for the pulse with $s_J \times J_{opt}$ = 160 Hz, but decreases in the later scans. Side bands could, however, interfere with nearby signals that are small.

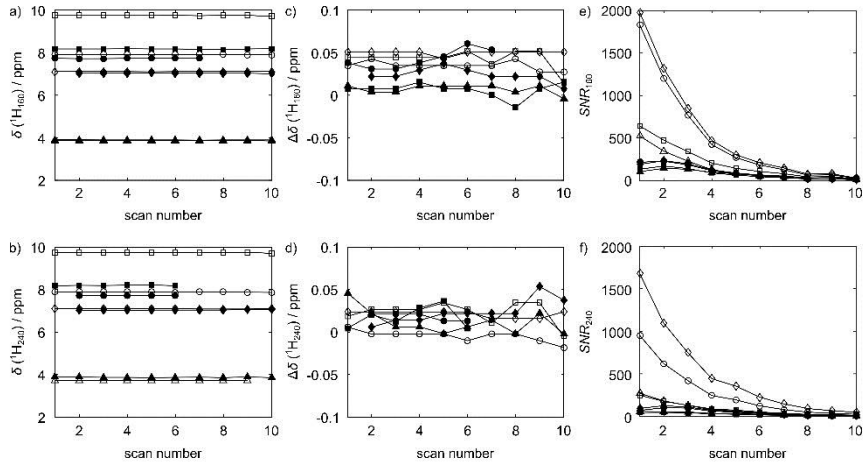

Fig. 2.7. a) The calculated ^{1}H chemical shift $\delta(^{1}H)$ from the ^{13}C experiment with the ^{1}H SHOT pulse of J_{opt} = 160 Hz and s_J = 1, shown as a function of scan number. b) The same as (a), but using the SHOT pulse with s_J = 1.5. c) ^{1}H chemical shift difference $\Delta\delta(^{1}H)$ between the calculated value of (a) and the real value from a thermal measurement, shown as a function of scan number. d) $\Delta\delta(^{1}H)$ between the calculated value of (b) and the real value from a thermal measurement, shown as a function of scan number. e) The SNR of each corresponding ^{13}C resonance using the SHOT pulse with s_J = 1, shown as a function of scan number. f) The same as (e), but using the SHOT pulse with s_J = 1.5. Carbons 1, 1', 3, 3', 4, 4', 6, 6' are indicated by open and filled triangle, diamond, circle and square. In (a)-(d), no data points are displayed when no signal was detectable.

Table 2.5. ^{1}H chemical shift calculation from hyperpolarized ^{13}C spectrum in Figure 2.3b with ^{1}H SHOT pulse of $s_J \times J_{opt}$ = 160 Hz.

^{13}C group	$\delta(^{13}C)$ (ppm)	J_{SHOT} (Hz)	$J_{SHOT} / s_J \times J_{opt}$	$\delta(^{1}H_{cal})$ (ppm)	$\delta(^{1}H_{real})$ (ppm)	$\Delta\delta(^{1}H)$ (ppm)
6	195.9	155	0.97	9.75	9.71	0.04
6'	166.2	115	0.72	8.18	8.17	0.01
4	134.4	108	0.68	7.91	7.88	0.03
4'	132.0	103	0.65	7.73	7.70	0.03
3	116.2	88	0.55	7.12	7.07	0.05
3'	116.0	85	0.53	7.03	7.01	0.02
1	56.6	5	0.03	3.90	-	-
1'	56.5	4	0.03	3.86	3.86	0.00

From the J-splitting measured in each 1D ^{13}C spectrum (Figure 2.4b), proton chemical shifts of both the reactant and reaction product were determined using Eq. 2.1 (see Table 2.5 and 2.6). Since the ^{13}C data sets contain signals from reactant and reaction product in the first 10 scans, the corresponding ^{1}H chemical shifts for these species can be calculated from each scan and should remain constant throughout the reaction (see Fig. 2.7a and b). The precision and accuracy of the correlated ^{1}H chemical shifts can be evaluated by comparing the chemical shift values among the different scans, as well as by comparing with ^{1}H NMR spectra of the respective compounds. Fig. 2.7c and d show the difference between the chemical shifts determined from the experiments with SHOT pulses and the ^{1}H NMR reference experiment, apart from the methyl group (1), for which the ^{1}H chemical shift overlaps with the solvent resonance in the reference spectrum. The overall standard deviation of these difference values is 0.02 ppm, representing a measure for the accuracy of the determination of the indirect ^{1}H chemical shift. Even though the ratio of signal to stochastic noise decreases as scan number increases (see Fig. 2.7e and f), the correlated ^{1}H chemical shift in the indirect dimension can still be calculated accurately for each scan.

Table 2.6. ^{1}H chemical shift calculation from hyperpolarized ^{13}C spectrum in Figure 2.3b with ^{1}H SHOT pulse of $s_J \times J_{opt}$ = 240 Hz.

^{13}C group	$\delta(^{13}C)$ (ppm)	J_{SHOT} (Hz)	$J_{SHOT} / s_J \times J_{opt}$	$\delta(^{1}H_{cal})$ (ppm)	$\delta(^{1}H_{real})$ (ppm)	$\Delta\delta(^{1}H)$ (ppm)
6	195.9	239	1.00	9.73	9.71	0.02
6'	166.2	202	0.84	8.18	8.17	0.01
4	134.4	195	0.81	7.88	7.88	0.00

Table 2.6. Continued.

^{13}C group	$\delta(^{13}C)$ (ppm)	J_{SHOT} (Hz)	$J_{SHOT} / s_J \times J_{opt}$	$\delta(^1H_{cal})$ (ppm)	$\delta(^1H_{real})$ (ppm)	$\Delta\delta(^1H)$ (ppm)
4'	132.0	191	0.80	7.72	7.70	0.02
3	116.2	176	0.73	7.09	7.07	0.02
3'	116.0	174	0.73	7.02	7.01	0.01
1	56.6	95	0.40	3.72	-	-
1’	56.5	98	0.41	3.86	3.86	0.00

2.4 Conclusion

Chemical shift correlations are obtained from a single NMR spectrum, which is useful in combination with hyperpolarization by D-DNP for monitoring non-equilibrium chemical reactions, with the goal of determining the identity of transient species and reaction mechanisms. Under off-resonance decoupling by SHOT pulses, the calculation of indirectly detected chemical shift is straight forward due to the linear relationship between the observed *J*-splitting and frequency offset and due to the uniform slope the precision of the chemical shift determination is uniform in the entire frequency range for which the pulses were developed. Moreover, the chemical shifts can be estimated even without precise knowledge of actual coupling constants. In addition, SHOT pulses can scale the observed *J*-splittings in an NMR spectrum to values larger than the actual coupling constant which was demonstrated here for the first time. This feature is useful to resolve overlap in some cases. In view of the robustness and, once pulses have been computed, simple implementation of this method, the scope of its application can be extended to many small and medium sized molecules. It may be useful in areas such as

analyzing enzymatic and chemical reaction intermediates, as well as studying the fate of in vivo metabolites over time.

CHAPTER III

COMPARISON OF KINETIC MODELS FOR ANALYSIS OF MEMBRANE TRANSPORT OF PYRUVATE USING SUSPENSIONS OF INTACT AND LYSED ESCHERICHIA COLI CELLS BY HYPERPOLARIZED NMR

3.1 Introduction

NMR is a powerful technique to measure metabolic flux, in systems ranging from perfused organs,[69] through animal models,[70] to humans.[71,72] Compared to other spectroscopic methods, an inherent limitation of NMR is a lack of sensitivity. Dissolution DNP (D-DNP), which enhances signal by several orders of magnitude, makes a significant breakthrough in this field.[29] Various metabolic precursors, such as $^{13}C_1$-pyruvate, $^{13}C_1$-ascorbic acid, [U-^{13}C, U-^{2}H] glucose, and others, have been used to track a variety of metabolic pathways using D-DNP.[150] Among them, pyruvate is the most extensively used molecule, due to its long T_1 relaxation and fast metabolic rates.[151]

Acquisition of a series of time-resolved spectra after injection hyperpolarized pyruvate to living systems enables investigation of the kinetics of the conversion of pyruvate to its downstream metabolites in specific metabolic pathways. The kinetic analysis of hyperpolarized ^{13}C label transfer between pyruvate and its metabolic products was reported,[76,78] where changes in metabolic flux were determined by two steps: membrane transport of pyruvate from extracellular spaces to intracellular spaces and the intracellular conversion of pyruvate to metabolic products catalyzed by intracellular enzymes.[77] In order to understand the origin of the observed flux, it is necessary to identify which process, either the membrane transport of pyruvate or enzyme catalysis, determines

the effective conversion of pyruvate. Harris analyzed rates of pyruvate-to-lactate conversion as a function of pyruvate concentration in human breast cancer cells and found that transport is a rate limiting process for the conversion of pyruvate to lactate.[152] Here, we present that, by removing cell membrane of *E.coli* cells, kinetic analysis showed that an apparent rate of conversion from pyruvate to CO_2 was increased. The experimental results were then compared with calculated signals from a zero order kinetic model and a first order kinetic model where transport rate could be estimated.

3.2 Experimental Section

3.2.1 Cell Culture and Cell Lysate Preparation

The E.*coli* BL21 wild type cells were inoculated in 20 mL lysogeny broth (LB) medium (10g/L peptone, 5g/L yeast extract and 5g/L sodium chloride) from an agar plate and were grown as precultures overnight at 37^{o}C until OD^{600} = 0.02. Then 1 mL of the preculture solution was transferred to an Erlenmeyer flask containing 1L LB broth medium. Cells were grown until OD^{600} = 3 and harvested by centrifugation for 5 min. The supernatant was discarded and cells were resuspended in 3 mL phosphate buffer (100 mM, pH 7.4). For cell lysate preparation, 3 mL cell suspension was sonicated (30 cycles with pulses 1 s on / 1 s off) for 1 min on ice. In order to maintain cell viability or enzyme activity, 600 uL of cell suspension or cell lysate was transferred to a 10 mm NMR tube shortly before NMR measurement.

3.2.2 Hyperpolarization

A solution of 1 M $^{13}C_1$-pyruvate (Cambridge Isotopes, Tewksbury, MA) with 15 mM tris[8-carboxy-2,2,6,6-tetrakis(2-hydroxyethyl)benzo[1,2-d:4,5-d′]bis[1,3]-dithiol-4-yl]methyl free radical sodium salt (OX63; Oxford Instruments, U.K.) and 1 mM diethylenetriamine pentaacetic acid gadolinium complex (Gd-DTPA; Sigma-Aldrich, St. Louis, MO) was prepared in a D_2O/ethylene glycol (2/3 v/v) glass forming mixture. 5 μL of this sample solution was hyperpolarized for 3 hours at 1.4 K in a HyperSense system (Oxford Instruments, Abingdon, UK), by irradiating microwaves (60 mW) at a frequency of 93.965 GHz in a 3.35 T magnetic field. Subsequently, the hyperpolarized sample was quickly dissolved in pre-heated 100 mM phosphate buffer of pH 7.4, injected rapidly into a 10 mm NMR tube installed in an NMR instrument (Bruker Biospin, Billerica, MA) by a gas driven injection device[33], and mixed with 600 μL cell suspension or cell lysate preloaded in the NMR tube. During sample injection, pressurized nitrogen gas was applied with 6.9 bar forward and 4.7 bar backward pressures. From the start of sample injection to the start of NMR measurement, the total time elapsed was 4.2 s.

3.2.3 NMR Spectroscopy

The NMR spectra were acquired on a 400 MHz NMR spectrometer with a selective SEX probe (Bruker Biospin, Billerica, MA). The pulse sequence consisted of (trigger – $[G_z - \alpha - \text{acquire}]_{\times n}$). A pulsed field gradient G_z (67.2 G/cm, 1 ms) was applied for attenuation of coherences present from the previous scans. The small flip angle of the excitation pulse was 10^o. The pulse strength $(\gamma B_1)/2\pi$ = 15.6 kHz. A total of n = 100

transients were acquired over a duration of 400 s. In each scan, 26 k complex points were acquired with an acquisition time of 0.5 s.

T_1 relaxation times were measured using an inversion recovery pulse sequence without hyperpolarization. The pulse strength $(\gamma B_1)/2\pi = 27.8$ kHz. Variable delay list τ between 180^o and 90^o pulses was 0 s, 10 s, 20 s, 60 s, 100 s, 150 s. A total of 6 scans were acquired in each experiment with 10 repetitions in each scan for cell suspension and 32 repetitions in each scan for cell lysate. The time interval between two repetitions was 80 s.

3.3 Results and Discussion

The time evolution of 1D ^{13}C spectra of hyperpolarized $^{13}C_1$-pyruvate with *E.coli* cell suspension or cell lysate are shown in Figure 3.1. The signals at 170.4 ppm, 160.3 ppm and 124.8 ppm are identified as ^{13}C signals of $^{13}C_1$-pyruvate, metabolic products $H^{13}CO_3^-$ and $^{13}CO_2$. A further signal at 178.7 ppm belongs to $^{13}C_1$-pyruvate hydrate, which is metabolically inert. The observation of these metabolic signals is consistent with the metabolic pathway as shown in Figure 3.2. Due to the combined effects of small flip angle pulses, T_1 relaxation and reaction kinetics, the signal depletion of substrates and signal buildup of metabolic products is observed as reaction time increases.

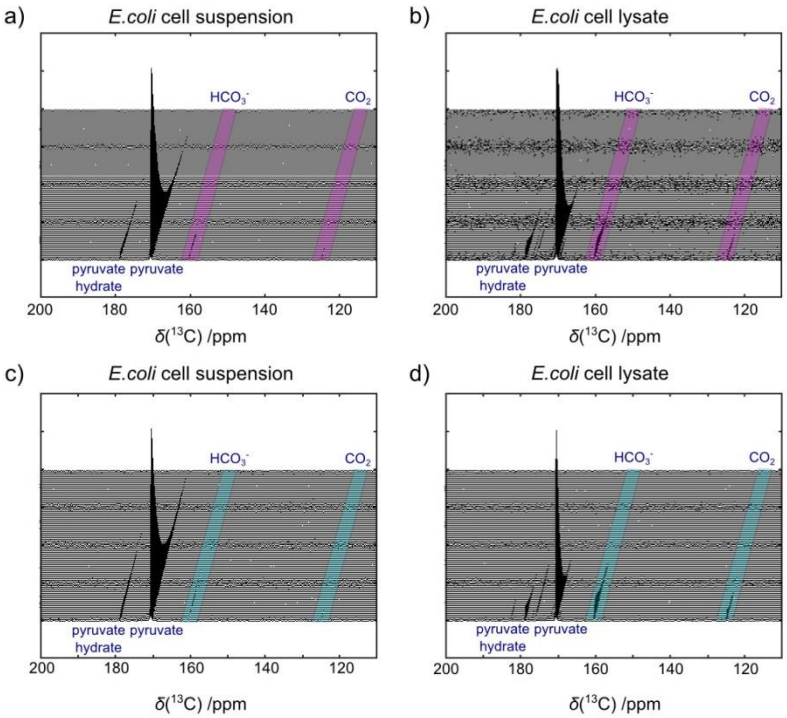

Fig. 3.1. Stacked plots of ^{13}C spectra after injection hyperpolarized $^{13}C_1$-pyruvate to a), c) *E.coli* cell suspension and b), d) *E.coli* cell lysate. Spectra were measured with a time interval of 4 s for a), b) and 3 s for c) and d).

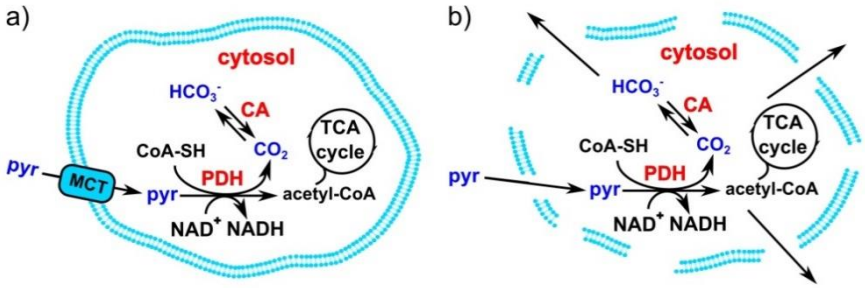

Fig. 3.2. Scheme of pyruvate transport and its metabolic pathway in a) *E.coli* cell suspension and b) *E.coli* cell lysate. MCT: monocarboxylate transporter; PDH: pyruvate dehydrogenase; CA: carbonic anhydrase.

Table 3.1. Kinetic fitting results after injection hyperpolarized $^{13}C_1$-pyruate to *E.coli* cell suspension and cell lysate. a, b and c, d are fitting results for data sets acquired with time intervals 4 s and 3 s, respectively. $k_{pyr\text{-}CO2}$ and $k_{CO2\text{-}biCO2}$ are conversion rate constants. r_{pyr} is relaxation rate of pyruvate. The errors are from 95% confidence interval of the fit.

Fit parameters	Fitting results (s^{-1})			
	a. cell suspension	b. cell lysate	c. cell Suspension	d. cell lysate
$k_{pyr\text{-}CO2}$	0.0006±0.0001	0.0036±0.0001	0.0005±0.0001	0.0075±0.0002
$k_{CO2\text{-}biCO2}$	0.21±0.03	0.20±0.01	0.27±0.03	0.17±0.00
*r*pyr	0.015±0.002	0.024±0.001	0.015±0.002	0.034±0.001

The signals of pyruvate, HCO_3^- and CO_2 in Figure 3.1 were quantitatively modeled:[152]

$$\frac{dM_{z,pyr}}{dt} = -k_{pyr-CO2} \times M_{z,pyr} - (r_{pyr} + \lambda) \times M_{z,pyr} \quad (3.1)$$

$$\frac{dM_{z,CO2}}{dt} = -k_{CO2-biCO2} \times M_{z,CO2} + k_{pyr-CO2} \times M_{z,pyr} - (r_{CO2} + \lambda) \times M_{z,CO2} \quad (3.2)$$

$$\frac{dM_{z,biCO2}}{dt} = k_{CO2-biCO2} \times M_{z,CO2} - (r_{biCO2} + \lambda) \times M_{z,biCO2} \quad (3.3)$$

Here, $M_{z,pyr}$, $M_{z,CO2}$ and $M_{z,biCO2}$ are z-magnetizations of pyruvate, CO_2 and HCO_3^-. r_{pyr}, r_{CO2} and r_{biCO2} are the respective relaxation rates on the carbonyl sites. $k_{pyr-CO2}$ and $k_{CO2-biCO2}$ are conversion rate constants for pyruvate and CO_2, respectively. The parameter $\lambda = -\ln(\cos(\alpha))/\Delta t$ is to compensate signal depletion due to small flip angle pulses, where α = 10° and Δt is time interval between two scans. The relaxation rates of CO_2 and HCO_3^- were measured in thermally polarized experiments (Figure 3.3) and used in the fitting. Four data sets were acquired as shown in Figure 3.1. Signal integrals of each

data set were fitted individually using the kinetic model (Figure 3.4). The fitting results are shown in Table 3.1.

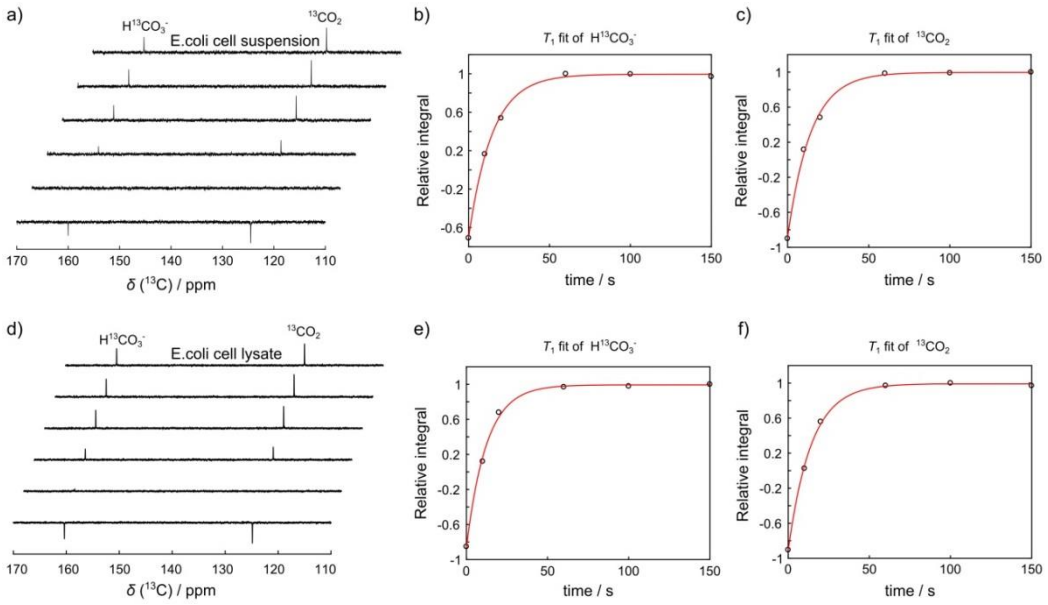

Fig. 3.3. Stacked plots of a series of thermally polarized ^{13}C spectra of $H^{13}CO_3^-$ and $^{13}CO_2$ in a) *E.coli* cell suspension and d) *E.coli* cell lysate using an inversion recovery pulse sequence. Signals of $H^{13}CO_3^-$ and $^{13}CO_2$ were produced by adding 302 mM $^{13}C_1$-pyruvate in cell suspension or lysate. 0.4 mM OX063 radical and 0.03 mM Gd-DPTA were also added in the sample in order to perform the measurements under the same experimental conditions as the hyperpolarized measurements. A variable decay list τ = 0 s, 10 s, 20 s, 60 s, 100 s, 150 s was applied in ascending order from bottom to top spectrum in a) and d). Integrals of b) $H^{13}CO_3^-$ and c) $^{13}CO_2$ in a) are plotted as a function of τ and fitted with $I_s = I_0 \cdot (1 - 2 \cdot \exp\left(-\frac{\tau}{T_1}\right))$. The fitting results are $T_{1,HCO3^-}$ = (14.5±2.2) s, $T_{1,CO2}$ = (14.2±2.8) s. Integrals of e) $H^{13}CO_3^-$ and f) $^{13}CO_2$ in d) are plotted as a function of τ and fitted with the same equation as in b) and c). The fitting results are $T_{1,HCO3^-}$ = (12.4±2.3) s, $T_{1,CO2}$ = (14.1±1.7) s. In b), c), e), and f), integrals in each panel are normalized to the maximum integral of the same panel. The errors are from 95% confidence interval of the fit. $T_{1,HCO3^-}$ and $T_{1,CO2}$ fall in the range of values reported in an aqueous solution ($T_{1,HCO3^-}$ = (10±1) s at near neutral pH) as well as for an *in vivo* experiments using rat hearts ($T_{1,HCO3^-}$ = 19 s, $T_{1,CO2}$ = 21 s).[153,154]

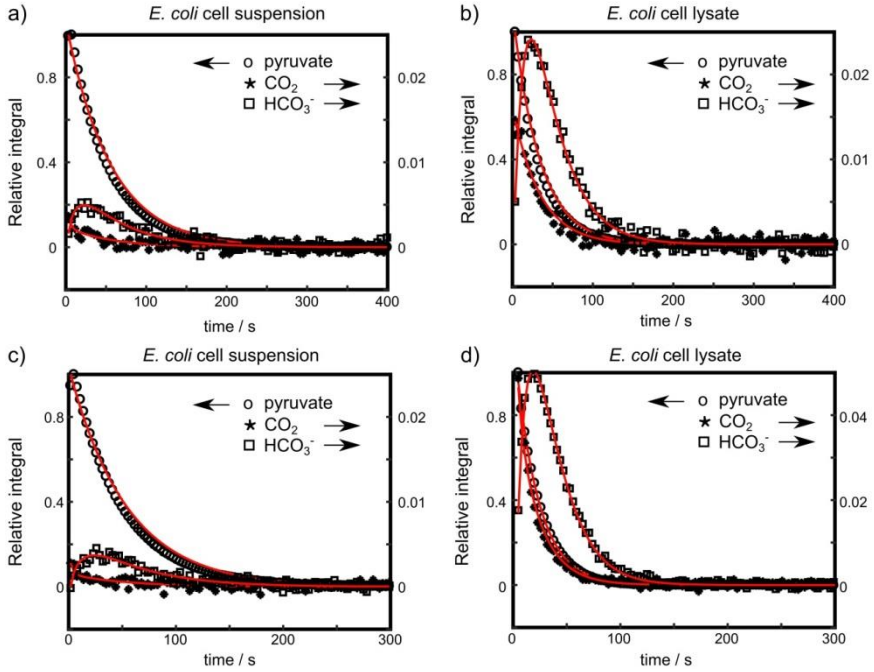

Fig. 3.4. Time dependent signal integrals and kinetic fit of pyruvate, CO_2 and HCO_3^- signals after injection hyperpolarized $^{13}C_1$-pyruvate to a),c) E.*coli* cell suspension and b),d) E. *coli* cell lysate. Signals were measured with a time interval of 4 s for a), b) and 3 s for c) and d). In each panel, the integrals were normalized with the maximum integral of the same panel.

Based on the quantitative modeling of signal integrals, the estimated pyruvate relaxation rates r_{pyr} in cell suspension and cell lysate were averaged which were 0.015 s^{-1} and 0.029 s^{-1}, respectively. The relaxation rates approximate the values reported for *in vitro* experiments using an one-way kinetic model (r_{pyr} = 0.017 s^{-1})[155] or using glioblastoma cells (r_{pyr} = (0.0207±0.0027) s^{-1})[78] and in *vivo* experiment (r_{pyr} ~ 0.033 s^{-1}).[156] The conversion of pyruvate to CO_2, $k_{pyr\text{-}CO2}$ in cell suspension, depends on the activity of PDH as well as the membrane transport of pyruvate by MCT. On the other hand, because of the removal of cell membrane, $k_{pyr\text{-}CO2}$ in cell lysate only depends on PDH's activity. As shown in Table 3.1, $k_{pyr\text{-}CO2}$ is increased from (0.0006±0.0001) s^{-1} /

(0.0005±0.0001) s^{-1} in cell suspension to (0.0036±0.0001) s^{-1} / (0.0075±0.0002) s^{-1} in cell lysate presumably due to the removal of membrane barrier. The values of $k_{pyr\text{-}CO2}$ in cell lysate in Table 3.1 b and d are on the same order, albeit not equal. A difference in the estimated conversion rate constants may be due to a loss of enzyme activities caused by heat generation during the sonication process for the removal of cell membrane. This effect could be minimized by controlling sample temperature during sonication or employing other method to remove cell membrane, such as using a buffer solution containing a non-ionic detergent.[157]

In order to better interpret the experimental results, a simulation for the conditions observed in pyruvate, CO_2, HCO_3^- signals in suspensions of intact and lysed *E.coli* cells was performed, using a model as shown in Figure 3.5.

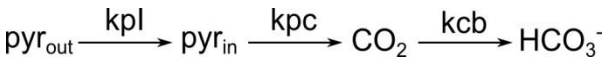

Fig. 3.5. A four pool model. k_{ij} represents conversion rate from pool i to pool j. pyr_{out}, extracellular pyruvate; pyr_{in}, intracellular pyruvate.

Here, two cases were taken into consideration. According to Michaelis-Menten equation, if pyruvate concentration is low and MCT are not saturated with pyruvate, the reaction is first order where reaction rate is proportional to pyruvate concentration. On the other hand, if pyruvate concentration is high, resulting in a saturation of MCT, the reaction is zero order where reaction rate is independent of pyruvate concentration. Therefore, differentiation equations are proposed according to first-order or zero-order kinetics.

Table 3.2. Conversion and relaxation rates used for calculating signals. Rates were chosen according to the fitting results from the experiments. The value of k_{pl} is varied as shown in Figure 3.6 and 3.7.

Parameters	values (s^{-1})
r_{pyr}	0.016
r_{CO2}	0.067
r_{HCO3^-}	0.071
*k*cb	0.20
*k*pc	0.005
*k*pl	varied

In case of a first-order reaction, the signals were quantitatively modeled:

$$\frac{dM_{z,pyr,out}}{dt} = -k_{pI} \times M_{z,pyr-out} - r_{pyr} \times M_{z,pyr,out} \quad (3.4)$$

$$\frac{dM_{z,pyr,in}}{dt} = k_{pI} \times M_{z,pyr-out} - k_{pc} \times M_{z,pyr} - r_{pyr} \times M_{z,pyr,in} \quad (3.5)$$

$$\frac{dM_{z,CO2}}{dt} = -k_{cb} \times M_{z,CO2} + k_{pc} \times M_{z,pyr,in} - r_{CO2} \times M_{z,CO2} \quad (3.6)$$

$$\frac{dM_{z,biCO2}}{dt} = k_{cb} \times M_{z,CO2} - r_{biCO2} \times M_{z,biCO2} \quad (3.7)$$

Here, $M_{z,pyr,out}$, $M_{z,pyr,in}$, $M_{z,CO2}$ and $M_{z,biCO2}$ are z-magnetizations of extracellular pyruvate, intracellular pyruvate, CO_2 and HCO_3^- in cell suspension. The signals of pyruvate, CO_2, HCO_3^- were calculated by solving the differential equations (Eq. 3.5-3.7) and then specifying the conversion and relaxation rates using values obtained from the experiments (Table 3.2). $r_{pyr} = 0.016\ s^{-1}, r_{CO2} = 0.067\ s^{-1}$ and $r_{biCO2} = 0.071\ s^{-1}$ are the respective relaxation rates on the carbonyl sites. The rate of conversion from CO_2

to HCO_3^- $k_{cb} = 0.20\ s^{-1}$. Since membrane barrier was removed in lysed cells, the apparent rate of conversion of pyruvate ($k_{pyr\text{-}CO2}$) obtained from the experiment using lysed cells was considered as the rate of intracellular conversion of pyruvate (k_{pc}) in the calculation. Therefore, $k_{pc} = 0.005\ s^{-1}$. In order to simulate the changes in metabolic flux impacted by the rate of membrane transport of pyruvate k_{pI}, $k_{pI}$was set to different values (Figure 3.6 and 3.7).

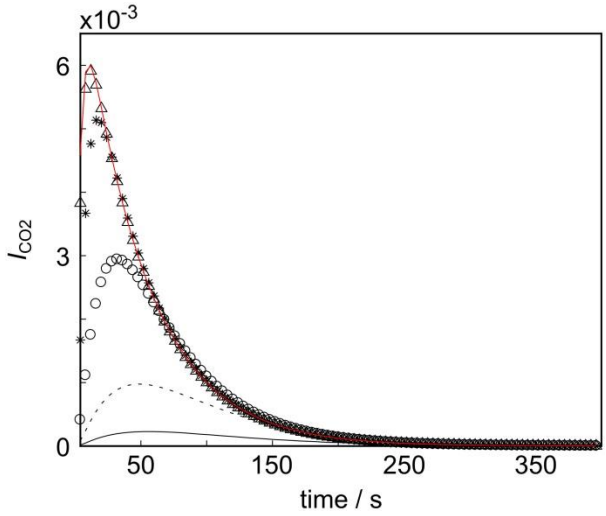

Fig. 3.6. Simulated CO_2 signals as a function of time using a first order kinetic model. The time interval between two data points was 4 s. Triangle, star, circle symbols and dashed line, line represent calculated signals using k_{pI} = 1,0.2,0.04, 0.008, and 0.0016 s^{-1}. Calculated signals represented by triangle symbols were fitted using eq. 3.1-3.2 (red curve) where $k_{pyr\text{-}CO2}$ was an unknown parameter, k_{pyr} = 0.016 s^{-1}, $k_{CO2\text{-}biCO2}$ = 0.20s^{-1}, r_{CO2} = 0.067 s^{-1}. The fitting result is $k_{pyr\text{-}CO2}$ =0.005 s^{-1}.

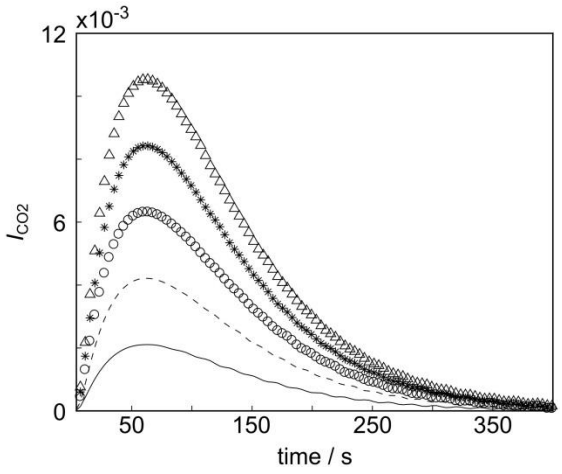

Fig. 3.7. Simulated CO_2 signals as a function of time using a zero order kinetic model. The time interval between two data points was 4 s. Triangle, star, circle symbols and dashed line, line represent calculated signals using k_{pI} = 5×10^{-5}, 4×10^{-5}, 3×10^{-5}, 2×10^{-5}, 1×10^{-5} s^{-1}.

When k_{pI} is 200 times larger than k_{pc} (triangle symbols in Figure 3.6), the calculated signals can be fitted using Eq. 3.1-3.2 without considering the transport process. In Eq. 3.1-3.3, $k_{\text{pyr-CO2}}$ is the apparent rate of conversion for pyruvate which takes into account the effect of both k_{pl} and k_{pc}. The fitting result of $k_{\text{pyr-CO2}}$ is 0.005 s^{-1}, which is the same as k_{pc} (0.005 s^{-1}) used in the calculation. When k_{pI} was larger than k_{pc} (star and circle symbols in Figure 3.6), decreasing k_{pI} by 5 times leads to a decrease of CO_2 signal by less than 5 fold, indicating membrane transport of pyruvate was not rating limiting. Both transport rate and activity of PDH determined the conversion of pyruvate in this case. When k_{pI} was smaller than or comparable to k_{pc} (line and dashed line in Figure 3.6 inset), a decrease of k_{pI} resulted in a decreased CO_2 signal by similar amount, indicating membrane transport of pyruvate is a rate limiting process. In all cases, as k_{pl} becomes

smaller, the peaks of the CO_2 curves shift right along the time axis corresponding to a slower production of CO_2, due to a slower transport of pyruvate across cell membrane.

In case of zero-order reaction, the signals were quantitatively modeled:

$$\frac{dM_{z,pyr,out}}{dt} = -k_{pI} \times \frac{M_{z,pyr-out}}{c_{pyr-out}} - r_{pyr} \times M_{z,pyr,out} \quad (3.8)$$

$$\frac{dM_{z,pyr,in}}{dt} = k_{pI} \times \frac{M_{z,pyr-out}}{c_{pyr-out}} - k_{pc} \times M_{z,pyr} - r_{pyr} \times M_{z,pyr,in} \quad (3.9)$$

$$\frac{dM_{z,CO2}}{dt} = -k_{cb} \times M_{z,CO2} + k_{pc} \times M_{z,pyr,in} - r_{CO2} \times M_{z,CO2} \quad (3.10)$$

$$\frac{dM_{z,biCO2}}{dt} = k_{cb} \times M_{z,CO2} - r_{biCO2} \times M_{z,biCO2} \quad (3.11)$$

$$\frac{dc_{pyr,out}}{dt} = -k_{pI} \quad (3.12)$$

The signals were calculated using the same procedure as indicated above. Relaxation and conversion rates used for calculation are shown in Table 3.2. The concentration of extracellular pyruvate $c_{\mathrm{pyr,out}}$ = 0.02 M which is the same as that used in the experiments. With zero order kinetics, the rate of CO_2 production does not depend on the rate of membrane transport of pyruvate. Therefore, the peaks of the CO_2 curves do not shift along the time axis as k_{pI} increases (Figure 3.7).

The experimental results were interpreted in view of the simulation results. In the experiments using cell suspension, the maximum signal integral of CO_2 is ~ 0.005 at time point ~ 8 s (Figure 3.4 a,c). This is very similar with calculated signals represented by star symbols using k_{pI} = 0.2 s^{-1} in first order kinetic model. As shown in Figure 3.6, the maximum signal integral of CO_2 is ~0.005 at time point ~ 12 s. Therefore, in case of first

order kinetics, k_{pl} of the experiment is presumably comparable with 0.2 s^{-1}. With this k_{pl}, both transport rate and activity of PDH determined the conversion of pyruvate. In zero order kinetic model, calculated signals represented by circle symbols using $k_{pl} = 3\times10^{-5}$ s^{-1} have signal integrals similar with that in the experiments. However, the calculated signals (cycle symbols) reach maximum at time point ~ 60 s which is not the same as that in the experiments. Therefore, the first order kinetic model appears to approximate the experiment results better than the zero order kinetic model. Since the contributions from the intra- and extracellular pyruvate signals could not be identified from the observed signals in the spectra, the first order and the zero order kinetic models could not fit the experimental data directly in order to obtain a transport rate. However, the transport rate could be estimated by comparing signals from the calculation and the experiments. Future work is needed to determine the transport rates experimentally and compare the measured values with the simulated results.

3.4 Conclusion

In summary, we have demonstrated a method to estimate the membrane transport rate of pyruvate, by calculating signals using proposed kinetic models and comparing the calculated signals with experimental results. Time resolved ^{13}C spectra of hyperpolarized pyruvate were measured in both *E.coli* cell suspension and cell lysate. The signal integrals were fit via a kinetic model where conversion rates for metabolic flux were obtained. An increase in the apparent rate of conversion of pyruvate was observed in experiments using cell lysate presumably due to the removal of membrane barrier. The experimental results

were then compared with signals calculated using kinetic models where transport rate could be estimated.

CHAPTER IV

HYPERPOLARIZED ULTRAFAST MULTIDIMENTIONAL DIFFUSION-T_2 LAPLACE NMR*

4.1 Introduction

NMR spectroscopy is one of the most powerful techniques for chemical analysis and molecular characterization. NMR measurements of T_2 relaxation and molecular self-diffusion explore molecular interactions and molecular motion, providing detailed chemical information by these parameters. Experimental data consisted of exponentially decaying components of diffusion and T_2 relaxation can be extracted by inverse Laplace transform, which is denoted as Laplace NMR (LNMR).

Conventional multidimensional diffusion-T_2 (D-T_2) LNMR needs repetition of the experiment, resulting in long experimental time. This is not applicable to D-DNP, due to the non-renewability of the hyperpolarized spin state.[29] UF D-T_2 LNMR, obtains the same diffusion and T_2 relaxation information as conventional measurements, but requires only a single scan.[65] The method relies on spatial encoding of multidimensional data, on the basis of the schemes of 1D diffusion [158] and T_2 relaxation experiment as well as UF experiment.[48] The single scan approach reduces the experiment time by several orders of magnitude and facilitates the use of D-DNP technique to boost experimental sensitivity.

Here, we demonstrate the application of hyperpolarized UF D-T_2 LNMR to a homogenous field using a 400 MHz magnet and an inhomogeneous field using a 13.24 M-

*Part of this chapter is reprinted with permission from Ahola, S.; Zhivonitko, V. V.; Mankinen, O.; Zhang, G.; Kantola, A. M.; Chen, H.-Y.; Hilty, C.; Koptyug, I. V.; Telkki, V.-V. (2015). "Ultrafast multidimensional Laplace NMR for a rapid and sensitive chemical analysis". *Nat. Commun. 6*, 8363. Copyright 2015 Creative Commons License.

-Hz single sided magnet. Compared to its high field counterpart which uses a pulsed field gradient, single sided NMR produces an intrinsic, constant and strong magnetic field gradient above the magnet.[66] The necessary diffusion and T_2 relaxation information can be accurately obtained on both magnets using D-DNP. Diffusion and T_2 relaxation distribution were extracted by Laplace inversion and shown in D-T_2 maps.

4.2 Experimental Section

4.2.1 Hyperpolarization

For UF experiments using a 400 MHz magnet, samples for hyperpolarization consisted of a 60 μL dimethyl sulfoxide (DMSO) in D_2O (v/v 18:7) with 15 mM sodium salt of tris-8-carboxyl-2,2,6,6 tetrakis[2-(1-hydroxethyl)]-benzo(1,2-d:4,5-dS)bis(1,3)dithiole-4-ylmethyl free radical (OX63; Oxford Instruments, Abingdon, U.K.) and 1 mM diethylenetriamine pentaacetic acid gadolinium complex (Gd-DTPA; Sigma-Aldrich, St. Louis, MO) for ^{13}C experiments or a 5 μL sample of DMSO in D2O (v/v 18:7) with 15 mM of 4-hydroxy-2,2,6,6-tetramethylpiperidine 1-oxyl radical (TEMPOL; Sigma-Aldrich, St. Louis, MO). For UF experiments using a single-sided magnet, a 45 uL DMSO in D_2O (v/v 1:1) with 15 mM TEMPOL radical was used as a sample for hyperpolarization. The sample was first hyperpolarized by irradiating 60 mW of microwaves at a frequency of 93.974 GHz at a temperature of 1.4 K in a field of 3.35 T for 3 hours for ^{13}C experiments. Hyperpolarization on ^{1}H was conducted using a 100 mW microwave power, a frequency of 94.005 GHz and an irradiation time of 30 min. Subsequently, hyperpolarized sample was rapidly dissolved in preheated water, transferred into an injection loop, and driven into a flow cell / sample holder (Figure 3.3)

pre-installed in a 400 MHz NMR magnet / on a single-sided NMR magnet, using water from a high pressure syringe pump[36] (model 1000D, Teledyne ISCO, Lincoln, NE).

4.2.2 NMR Spectroscopy

UF D-T_2 LNMR Using a High Field Magnet

UF *D*-T_2 LNMR measurements were acquired on a 400 MHz NMR spectrometer with a triple resonance TXI probe (Bruker Biospin, Billerica, MA) and installed NMR flow cell. The experiments were performed in single scans. The pulse sequence developed by Dr. Ahola and Dr. Telkki at University of Oulu is shown in ref. 160 . Each experiment was triggered after ~ 0.95 s injection and 3 s waiting time.

For ^{13}C detected experiment, 90° and 180° hard pulses were applied with $(\gamma B_1)/2\pi$ = 16.9 kHz. 180° frequency swept chirp pulses were with 10% smoothing on the edges. The pulse duration (t_{chirp}) is 2.0 ms, bandwidth is 44.6 kHz, $(\gamma B_{1max})/2\pi$ = 4.2 kHz. Pulsed field gradients are trapezoidal shaped with ramp time of 1 ms. Gradients are applied with amplitudes G_{sweep} = 32.5 G/cm, $G_{dephase}$ = 6.3 G/cm, G_{read} = 6.3 G/cm, and durations $t_{G,sweep}$ = 4.0 ms, $t_{G,dephase}$ = 3.4 ms, $t_{G,read}$ = 6.2 ms. The diffusion delay is Δ = 200 ms. The simultaneously applied G_{sweep} and chirp pulses result in a spatial dependence of the effective length of *G* that a spin experiences, δ_{eff} = 0…4 ms. The spectral width is 100 kHz. The total experiment time is t_{exp} = 3 s. The resulting two dimensional *D*-T_2 data comprises a time (T) and a spatial frequency (S) dimension for obtaining T_2 and *D*, respectively. In the T dimension, *n* = 64 CPMG echoes are collected with CPMG loop time of 0.03 ms interval. Fourier transform of each echo leads to *m* = 512 points in the S dimension encoded in the UF PGSTE block.

For ^{1}H detected UF experiment, a water presaturation sequence was added before UF-PGSTE sequence and repeated 10 times in order to suppress a large water resonance. For presaturation, a selective 90^o Gaussian pulse was applied at the center of a water ^{1}H resonance at 4.7 ppm. The pulse duration is 7073 μs and excitation bandwidth is 300.4 Hz. Then a homospoil gradient was applied with amplitude 45.5 G/cm and duration 4 ms to dephase the ^{1}H transverse magnetization. All other experimental parameters for the subsequent *D*-T_2 measurement are shown in Table 4.1.

Table 4.1. Experimental parameters for ^{1}H *D*-T_2 measurement using a 400 MHz high field magnet.

P1 $(\gamma B_1)/2\pi$	28.5 kHz
t_{chirp}	1.0 ms
P2 bandwidth	107 kHz
P2 $(\gamma B_{1max})/2\pi$	9.2 kHz
P3 $(\gamma B_1)/2\pi$	28.5 kHz
G	20.2 G/cm
$G_{dephase}$	7.9 G/cm
G_{read}	7.9 G/cm
t_G	2.0 ms
$t_{G,dephase}$	2.9 ms
$t_{G,read}$	5.2 ms
Δ	100 ms
δ_{eff}	[0 ms, 4 ms]
points in T dimension	64
points in S dimension	512
spectral width	100 kHz
t_{exp}	1 s
t_{CPMG}	[0.01 s, 0.64 s] with interval 0.01 s

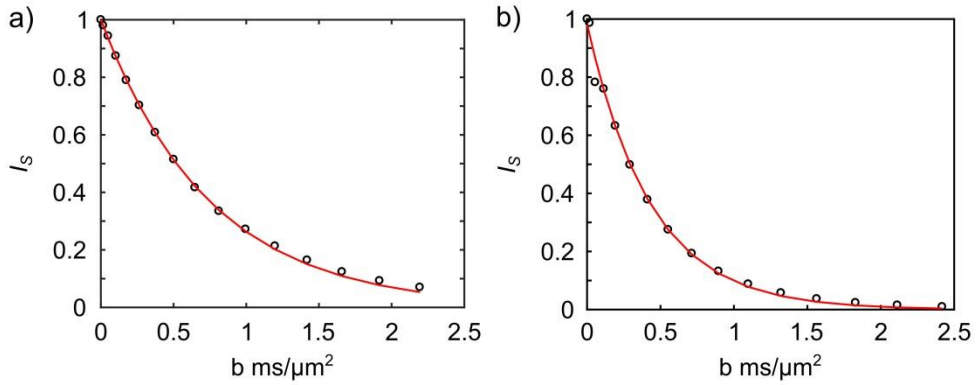

Fig. 4.1. a) ^{1}H NMR diffusion signal of a) thermally polarized DMSO on its methyl proton at T = 300 K and b) thermally polarized H_2O at T = 298 K as a function of $b = (\gamma G\delta)^2(\Delta - \frac{\delta}{3})$, using a conventional PGSTE sequence. In a), the spectrum was acquired under the same sample condition as the ^{1}H *D*-T_2 experiment of hyperpolarized DMSO. The final concentration of DMSO is 34 mM. The red fitting line yields a self-diffusion coefficient of $D = (1.3 \pm 0.1) \cdot 10^{-9}$ m^2/s. In b), the fitting result is $D = (2.3 \pm 0.3) \cdot 10^{-9}$ m^2/s, in agreement with a self-diffusion coefficient of $D_{water} = 2.3 \cdot 10^{-9}$ m^2/s from literature values.[159]

For diffusion coefficient measurement, a conventional pulsed field gradient stimulated echo (PGSTE) sequence was used for diffusion measurement (Figure 4.1a), using thermally polarized ^{1}H signals of a DMSO sample the same as that used in the hyperpolarized ^{1}H *D*-T_2 measurement. The pulse sequence consisted of [p1 – G1 – p1 – τ_1 / G2 – p1 – G3 –acquire]$_{\times n}$. 90^o hard pulses p1 were applied with $(\gamma B_1)/2\pi = 26.9$ kHz. The amplitudes of diffusion encoding gradient and diffusion decoding gradient, G1 and G3, respectively, were simultaneously and linearly increased from 1.17 G/cm to 55.58 G/cm with n = 16 steps. The gradient duration δ was 1 ms. The diffusion time Δ which is between the first and last p1 was 100 ms. Delay $\tau 1 = 98.0$ ms. A homospoil gradient G2 was applied with amplitude –10.02 G/cm and duration $\delta_{homospoil} = 0.8$ ms. By applying a pulsed field gradient spin echo sequence to a phantom, the maximum z-gradient was calibrated as 65

G/cm. The diffusion coefficient of thermally polarized water was also measured using a conventional PGSTE sequence (Figure 4.1b). The experimental parameters are $(\gamma B_1)/2\pi$ = 28.15 kHz, δ = 1.05 ms, Δ = 0.1 s, $\tau 1$ = 96.1 ms, $\delta_{homospoil}$ = 0.85 ms.

UF D-T_2 LNMR Using a Single-Sided Magnet

UF *D*-T_2 LNMR measurement was acquired using a 13.24 MHz single-sided PM25 magnet (Magritek, New Zealand) and Scout spectrometer (Tecmag, TX). A linear field gradient of G = 6.59 T/m is produced by the magnet. The experiment was triggered after 595 ms injection time and performed in a single scan. The pulse sequence (Figure 4.2) is provided by Dr. Meldrum at University of William and Mary.

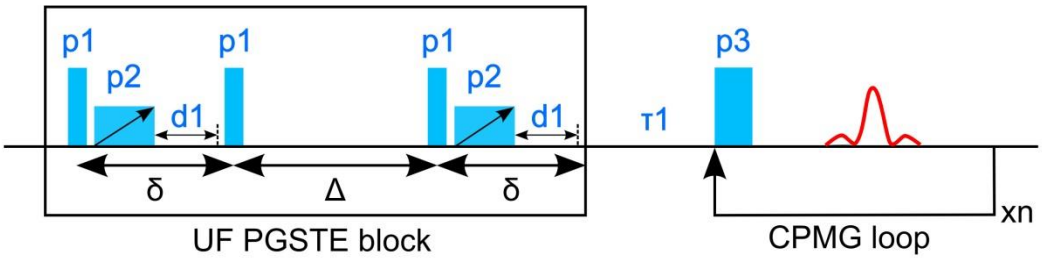

Fig. 4.2. Ultrafast Pulsed Field Gradient Stimulated Echo (UF-PGSTE) pulse sequence for D-T_2 measurement on a 13.24 MHz single-sided magnet. P1 and P3 are 90° and 180° hard pulses with ($\gamma B_1/2\pi$) = 20.8 kHz. The diffusion delay is 5.4 ms which is sum of Δ = 5 ms and δ = 400 µs. P2 are 180° frequency swept chirp pulses which are linearly ramped with 1% smoothing on the edges. The pulse length (t_{chirp}) is 193.8 µs, maximum power is 24 W. A sliceheight (SH) which is the thickness of the coil sensitive region affected by chirp pulse is 200 µm. The resulting bandwidth of the chirp pulse (BW) is 56.1 kHz which is calculated from SH, G = 6.59 T/m and ($\gamma_{1H}/2\pi$) = 42.576 MHz/T. The phase and amplitude of the chirp pulse is generated based on BW, t_{chirp}, a temporal resolution of the spectrometer dt = 40 ns, using a Matlab program (MathWorks, Natick, MA) which was described elsewhere.[66] Delay d1 is set as the same as t_{chirp} which leads to δ_{eff} = 0…387 µs due to the simultaneously applied G and P2. Here, δ_{eff} is a spatial dependence of the effective length of G that a spin experiences. In order to keep the echoes centered, the delay τ1 between the UF PGSTE block and CPMG loop is 200 µs which is half of an echo time of the first echo. The spectral width is 167 kHz. The resulting two dimensional D-T_2 data comprises a time (T) dimension and a spatial frequency (S) dimension for obtaining T_2 and D, respectively. In T dimension, the n = 64 echoes are acquired with CPMG loop time t_{CPMG} of 0.4 ms interval. The acquisition time for each echo is 0.324 ms. Fourier transform of each echo leads to 38 or 54 complex points along S dimension encoded in UF PGSTE block. The reference experiment was performed with the same parameters as that of UF-PGSTE, but the amplitude of P2 is set to zero.

4.2.3 Data Analysis

For ultrafast D-T_2 data measured using a single-sided magnet, the raw data was zero filled to 256 complex data points before Fourier transform using a Matlab program (MathWorks, Natick, MA).

To determine 2D relaxation time and diffusion coefficient distributions, the D-T_2 data was analyzed using a Laplace inversion program provided by P. Callaghan (Victoria

University of Wellington, New Zealand)[160] and based on a previously published method.[161] For ^{13}C ultrafast experiment using a 400 MHz NMR magnet, the number of samples (NS) in the T and S dimensions were 64 and 11, respectively. In order to reduce noise, the size of the data matrix was compressed to 40 × 11 points using singular value decomposition (SVD). Non-negative least square minimization (NNLS) with Tikhonov regularization was then performed over the data ranges δ_{eff} = [0.74 ms, 2.54 ms], corresponding to diffusion decay of the signal, and t_{CPMG} = [0.03 ms, 1.92 ms], for the target ranges T_2 = [0.5 s, 5 s] and D = [5×10^{-10} m^2/s, 5×10^{-9} m^2/s]. Parameters of Laplace inversion for ^1H ultrafast experiment using a 400 MHz NMR magnet and a single sided magnet are shown in table 4.2 and 4.3.

Table 4.2. Parameters of Laplace inversion for ^1H ultrafast experiment using a 400 MHz NMR magnet.

NS in T dimension	64
NS in S dimension	75
NS in T dimension after SVD	30
NS in S dimension after SVD	30
δ_{eff}	[0.35 ms, 1.72 ms]
t_{CPMG}	[0.01 s, 0.64 s]
targeted ranges of T_2	[0.1 s, 1 s]
targeted ranges of D	[10^{-10} m^2/s, 10^{-8} m^2/s]

Table 4.3. Parameters of Laplace inversion for ^{1}H ultrafast experiment using a single-sided magnet.

NS in T dimension	64
NS in S dimension	81
NS in T dimension after SVD	30
NS in S dimension after SVD	35
δ_{eff}	[0 ms, 0.36 ms]
t_{CPMG}	[0.4 ms, 25.6 ms]
targeted ranges of T_2	[0.001 s, 0.05 s]
targeted ranges of D	[5×10^{-10} m^2/s, 10^{-8} m^2/s]

4.2.4 Sample Holder

For hyperpolarized D-T_2 experiment using a single-sided magnet, the apparatus for sample transfer is very similar as described elsewhere,[162] except that a syringe pump with a flow rate of 400 mL/min was used to push the hyperpolarized sample solution from a loop into a sample holder (Figure 4.3). The holder was placed within the coil sensitive region by supporting it on 4 mm glass slides on the magnet. The sensitive region of the coil is 5 cm above the magnet with an adjustable thickness of 350 μm.

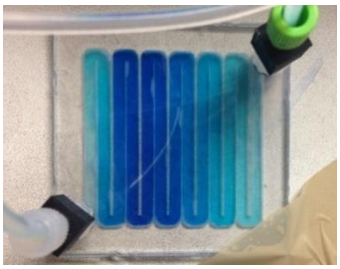

Fig. 4.3. A sample holder made by Lexan used for *D*-T_2 measurement. The s-patterned channels are 1.5 mm deep and across a 5 cm × 5 cm area. The blue dye inside the channel was used to confirm an appropriate injection time for delivering the sample in the holder. No bubbles were observed after sample transport.

4.3 Results and Discussion

4.3.1 Hyperpolarized UF D-T_2 LNMR Using a 400 MHz High Field Magnet

Figure 4.4a shows the ^{1}H spectra of hyperpolarized DMSO with and without water suppression. The spectra were acquired with 34 mM DMSO in H_2O at T = 300 K. Because of the strong hyperpolarized signal, the DMSO peak is broadened due to radiation damping.[163] The corresponding D-T_2 map was measured with solvent suppression in a single scan as shown in Figure 4.4c. All these data was obtained 3 s after delivering the sample into a flow cell. In this approach, sample flow was stopped by closure of inlet and outlet tubing at the same time. Since residual motion introduces artifacts in the acquired signal which disturbs spatial encoding, it is necessary to prevent such motion during NMR measurement. For this purpose, a flow cell with liquid driven injection was used.[36] The stability of the sample after injection into the flow cell was confirmed by a single scan UF D-T_2 measurement which shows sample movement is negligible after 3 s waiting time. D is found to be $(1.5\pm0.5)\cdot10^{-9}$ m^2/s. The value is inconsistent with that obtained by a conventional PGSTE measurement using a thermally polarized, stationary sample at T = 300 K, which yielded $D = 1.3\cdot10^{-9}$ m^2/s (Figure 4.1a). The agreement of D values demonstrates that the sample was nearly stationary when measurements started.

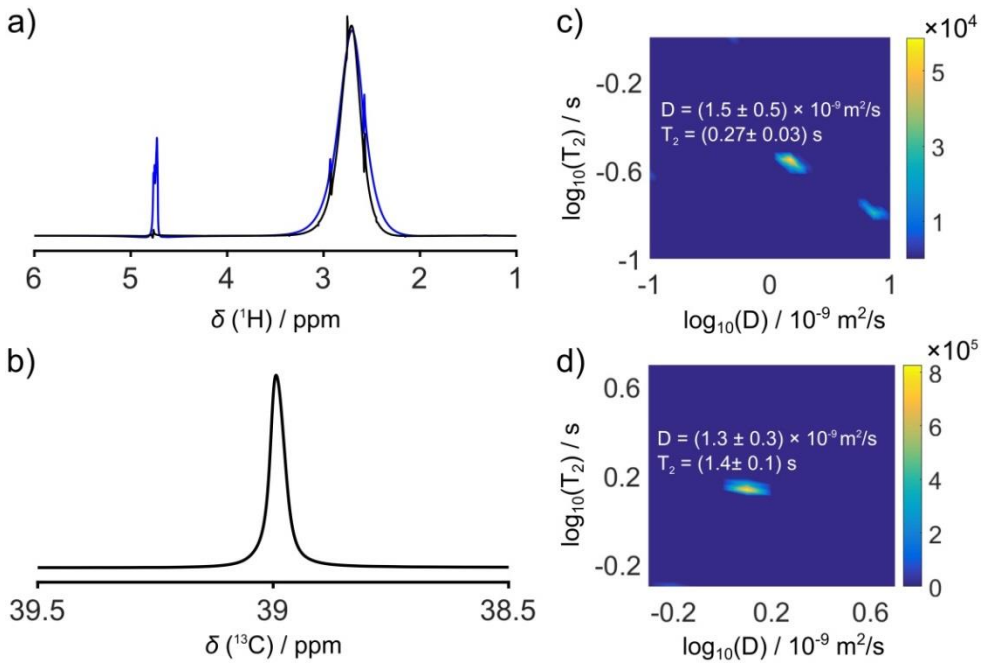

Fig. 4.4. a) ^{1}H spectra of hyperpolarized DMSO with (black spectrum) and without (blue spectrum) solvent suppression. b) ^{13}C spectrum of hyperpolarized DMSO. c) ^{1}H detected D-T_2 map of hyperpolarized DMSO measured with solvent suppression. d) ^{13}C detected D-T_2 map of hyperpolarized DMSO. The D and T_2 values correspond to the peaks with maximum intensities. The uncertainties are estimated from the width covered by the peaks.

A ^{13}C spectrum of hyperpolarized DMSO and its corresponding D-T_2 map are shown in Figure 4.4b and d. The final concentration of DMSO is 288 mM with ^{13}C signal enhancement of ~ 3200. This is calculated by comparing hyperpolarized ^{13}C signal of DMSO to that of a thermally polarized sample with known concentration. Since ^{13}C isotope has low natural abundance and small gyromagnetic ratio, the signal to noise ratio of the D-T_2 measurement is low (~ 24). However, the generated D-T_2 map by Laplace inversion resulted in diffusion coefficient in good agreement with UF ^{1}H and reference

experiments. This indicates that residual motions in the sample are successfully avoided after rapid transportation of hyperpolarized samples in the cell.

Since the use of read gradient during signal acquisition increases the echo attenuation[164], the resulting echo intensity is $S = S_0 \cdot \exp[t \cdot (-1/T_2' - \beta)]$, where T_2' is the observed relaxation time without a read gradient, $\beta = (8\gamma^2 G_{read}^2 te^2 D)/\pi^4$ is diffusion attenuation factor, *te* is the echo time of the first echo. This results in smaller observed T_2 in UF experiments than that measured in reference experiments using a CPMG sequence ($T_{2',1H}$ = 3.0 s, $T_{2',13C}$ = 2.8 s). Since γ_{1H} is ~ 4 fold larger than γ_{13C}, the observed $T_{2,1H}$ = (0.27 ± 0.03) s (Figure 4.4b) is smaller than the observed $T_{2,13C}$ = (1.4 ± 0.1) s (Figure 4.4d), even though $T_{2',1H}$ and $T_{2',13C}$ are very similar.

From the above demonstration, we emphasize that the employment of hyperpolarization technique makes UF *D*-T_2 LNMR experiment applicable to low-sensitivity heteronucleus, which is absolutely unachievable using conventional techniques with thermal polarization. Therefore, this ultrafast method opens unprecedented possibilities to the application of multidimensional LNMR in various fields.

4.3.2 Hyperpolarized UF *D*-T_2 LNMR Using a 13.24 MHz Single-Sided Magnet

Figure 4.5 shows a single-scan experimental ultrafast *D*-T_2 data of a hyperpolarized water sample (DMSO/H_2O (1/1, v:v)), measured using a single-sided magnet. Fourier transform of each echo of the hyperpolarized *D*-T_2 data results in 64 columns which correspond to 64 diffusion curves. Signals from the first column of the data are plotted as a function of space (z) in the coil sensitive region as shown in Figure 4.5a. Above the surface of the magnet, thickness of the sensitive layer affected by chirp

pulse is ~ 200 μm. The same data profile is also plotted against the effective length of gradient that a spin experiences (δ_{eff}) in the range of $\delta_{eff} = 0…387$ μs, corresponding to a signal intensity decrease. It can be seen that the data profile is heavily weighted by the excitation-detection profile of the coil. In order to compensate such weighting, each column of the *D*-T_2 data is divided by the same coil excitation-detection profile in Figure 4.5a and plotted as a function of time and b value as shown in Figure 4.5b.

Ultrafast *D*-T_2 maps of hyperpolarized water samples which consisted of DMSO/H_2O (1/1, v:v) or EG/H_2O (3/2, v:v) were shown in Figure 4.6. Each sample produces a single peak in the corresponding map. The *D* and T_2 values of the three maps are all within error limits which confirm the repeatability of the method. The T_2 values are underestimated due to the use of gradient during echo acquisition.[65] *D* values obtained from ultrafast experiment match that of a thermally polarized water measured by a conventional PGSTE pulse sequence using a 400 MHz NMR magnet at 298 K, which yielded D = (2.3±0.3) · 10^{-9} m^2/s (Figure 4.1b). The agreement of D values between the ultrafast and conventional measurements confirms the accuracy of the ultrafast method. It also demonstrates that the sample was already stationary after its rapid transfer in the sample holder at the time of measurement.

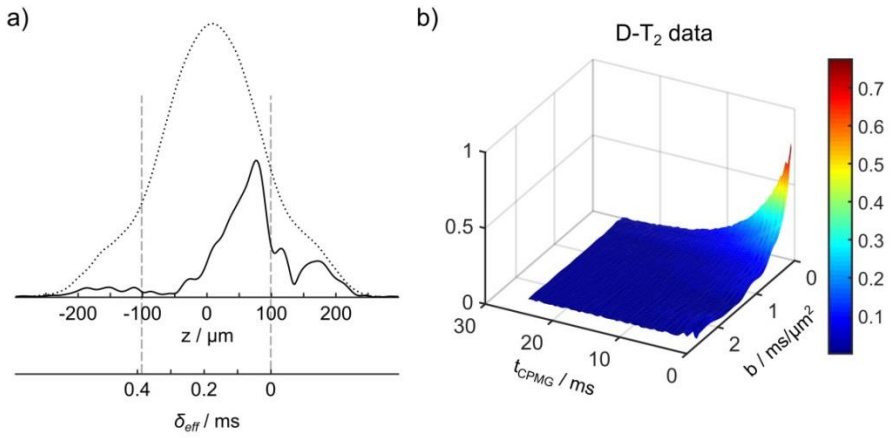

Fig. 4.5. a) Signals from the first column of ultrafast *D*-T_2 data (solid line) and coil excitation-detection profile (dotted line) of a hyperpolarized water sample (DMSO/H_2O (1/1, v:v)) with 38 complex points acquired along S dimension, shown as a function of space (z) in the coil sensitive region and δ_{eff}. The region swept by chirp pulse is indicated by the dotted grey lines. The beginning of the chirp pulse leads to an abrupt signal drop at δ_{eff} = 0 ms. b) Signals of the same ultrafast *D*-T_2 data as in a) are compensated by coil excitation-detection profile and shown as a function of t_{CPMG} and $b = \left(\gamma G \delta_{eff}\right)^2 \left(\Delta - \frac{\delta_{eff}}{3}\right)$. Points outside chirp pulse swept region are removed and those showing the signal decay in each column of the data are selected.

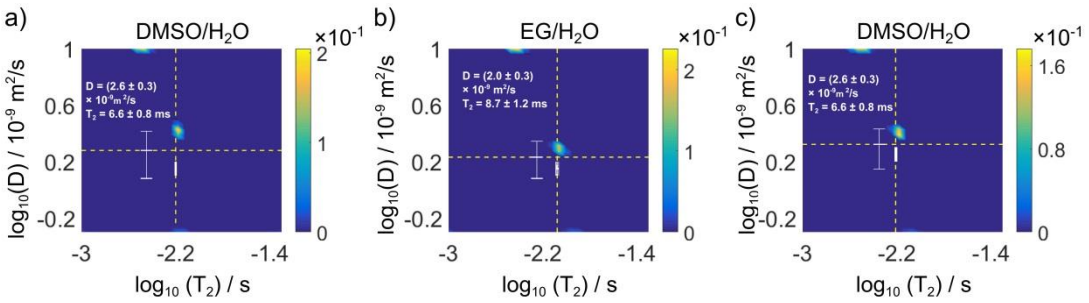

Fig. 4.6. *D*-T_2 maps including a),c) hyperpolarized DMSO/H_2O (1/1, v:v) and b) EG/H_2O (3/2, v:v). The number of complex points acquired along S dimension for a), b) and c) are 54, 54 and 38, respectively. The *D* and T_2 values are given from the peaks with maximum intensities. The uncertainties are obtained from peak width. Results from the single exponential fit of *D* and T_2 curves are represented by the dashed lines and white bars. Vertical bars represent 95% confidence intervals from the single exponential fit of T_2 curves (Figure 3.7). Horizontal bars represent errors obtained from the standard deviation of *D* values from the echoes (Figure 3.9).

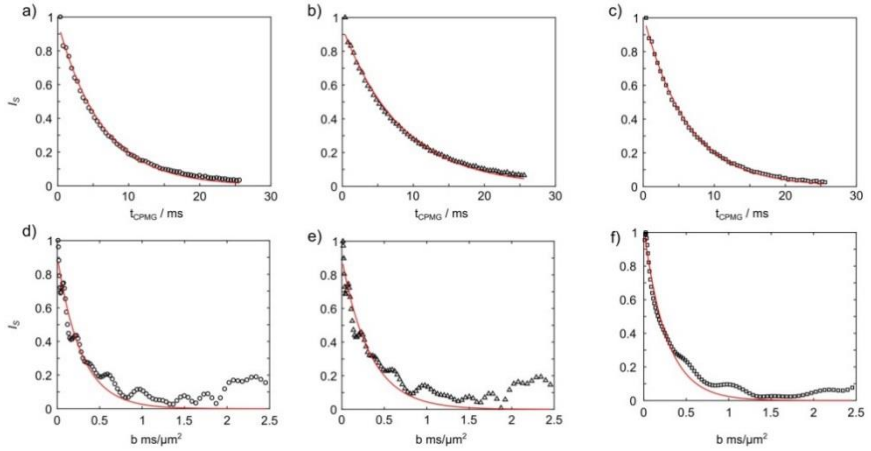

Fig. 4.7. Integral of hyperpolarized *D*-T_2 data of a),c) a DMSO/H_2O (18/7, v:v) sample and b) a EG/H_2O (3/2, v:v) sample along S dimension, shown as a function of t_{CPMG}. The integral of a), b) and c) comprises the range shown in d), e) and f), respectively. Signals are normalized to the maximum integral with shortest t_{CPMG}. Integrals are fitted with $I_S = I_0 \cdot \exp(-\frac{t_{CPMG}}{T_2})$ with fitting results T_2 = (6.3 ± 0.1) ms for a), (8.4 ± 0.2) ms for b) and (6.2 ± 0.1) ms. d), e) and f) Signals from the first columns of hyperpolarized *D*-T_2 data, shown in the S dimension as a function of $b = \left(\gamma G \delta_{eff}\right)^2 \left(\Delta - \frac{\delta_{eff}}{3}\right)$. Symbols represent the same data set as in a), b) and c). The number of complex points acquired along S dimension for d), e) and f) are 54, 54 and 38, respectively. Signals are normalized to the maximum signal amplitude with smallest b and fitted using the Stejskal–Tanner signal equation $I_S = I_0 \cdot \exp(-b \cdot D)$. Fitting results are D = (3.5 ± 1.3) · 10^{-9} m^2/s for d), (3.0 ± 1.3) · 10^{-9} m^2/s for e) and (3.8 ± 0.8) · 10^{-9} m^2/s for f).

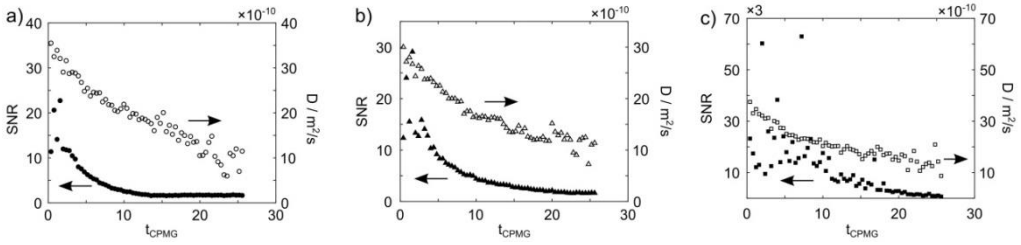

Fig.4.8. Signal to noise ratio and fitted D value of each echo as a function of echo time t_{CPMG} for hyperpolarized *D*-T_2 data of a),c) DMSO/H_2O (1/1, v:v) and b) EG/H_2O II (3/2, v:v). The SNR is calculated as the ratio of the maximum intensity of each echo to the standard deviation value of noise points. Noise points included the first 2 and last 3 points from the acquisition period of each echo, concatenated to comprise a total of 2×3 points. The complex points in S dimension for a), b) and c) are 54, 54, 38, respectively.

Since one peak is observed in each of the D-T_2 maps, the T_2 and D values of the data can be extracted by single exponential fit of the echoes along T and S dimension. As shown in Figure 4.7a-c, T_2 values are obtained from Fourier transform and integration of echoes from hyperpolarized D-T_2 data along S dimension. In Figure 4.7d-f, signals from the first columns of hyperpolarized D-T_2 data are plotted as a function of b values. Mean D values are derived by fitting diffusion decay curves in each column of the data along S dimension (Figure 4.9). The resulting D and T_2 values from the fit are in agreement with those in D-T_2 maps (Figure 4.6).

The SNR of the hyperpolarized D-T_2 data of DMSO/H_2O or EG/H_2O samples are ~ 20. A number of 54 complex points are collected in S dimension in these datasets. The SNR is increased to 130 of a second DMSO/H_2O sample by reducing the number of complex points to 38 in S dimension. Since SNR of each echo is lower as echo time increases (Figure 4.8), the fitted D value becomes smaller, resulting in large standard deviation of D (Figure 4.9). If D of each echo is weighted by its corresponding SNR, the resulting D from the weighted sum are $2.5 \cdot 10^{-9}$ m^2/s, $2.1 \cdot 10^{-9}$ m^2/s and $2.5 \cdot 10^{-9}$ m^2/s for Figure a, b and c, respectively.

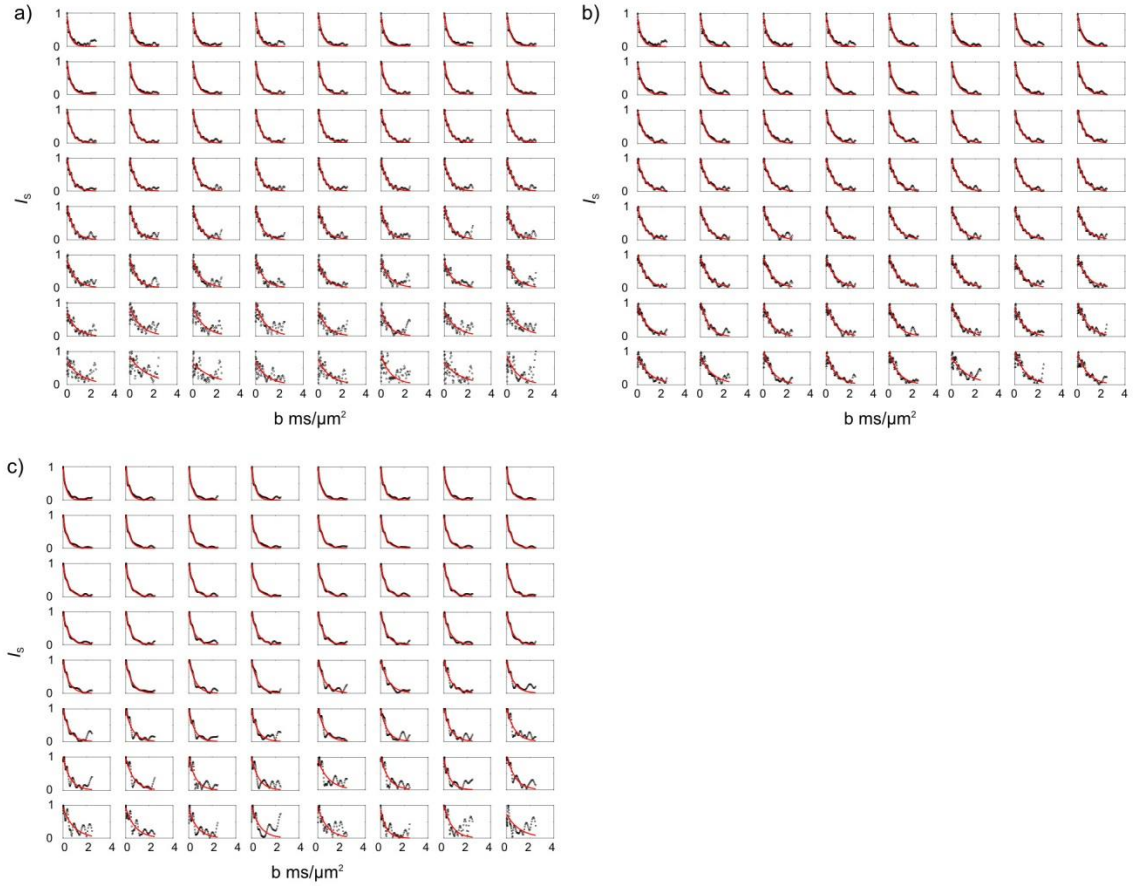

Fig. 4.9. Signals from 64 columns of hyperpolarized D-T_2 data of a), c) DMSO/H_2O (1/1,v:v) sample and b) a EG/H_2O (3/2, v:v) sample after Fourier transform of each echo along the S dimension with 54, 38 and 54 complex points, shown as a function of b and fitted with $I_s = I_0 \cdot \exp(-b \cdot D)$ (red curve). $b = \left(\gamma G \delta_{eff}\right)^2 \left(\Delta - \frac{\delta_{eff}}{3}\right)$ ranges from 0 ms/μm^2 to 2.1 ms/ μm^2. Each panel corresponds to signal decay from a column of the corresponding data set. The column number increases from left to right starting from the top row. The D values from the fit are averaged as mean D = (1.9±0.7) · 10^{-9} m^2/s, (1.7±0.5) · 10^{-9} m^2/s and (2.1±0.6) · 10^{-9} m^2/s for a), b) and c). The errors are from the standard deviation of D values. In each panel, signals are normalized to the maximum signal amplitude.

In this single-scan ultrafast LNMR experiment, spatial encoding reduced acquisition time by several orders of magnitude. Experimental sensitivity is enhanced by the use of hyperpolarization, which offers the opportunity to acquire single scan diffusion-

T_2 correlation information on a single-sided magnet with a magnetic field strength of 0.3 T. A polarization level of ~3% is achieved using hyperpolarized substances with a final proton concentration ~ 500 mM in the current experiment. The polarization level is calculated by comparing SNR of a hyperpolarized sample with that of the same sample without hyperpolarization. ^{1}H thermal polarization at this field strength is ~10^{-4}%. Without hyperpolarization, it needs ~6×10^8 number of scans to achieve the same SNR for a thermally polarized sample.

In order to observe an accurate magnetization profile, some experimental settings of the technique need to be aware of. For detecting a fully decayed diffusion curve along S dimension, an appropriate range of b values is needed, for instance a large b value is needed for measuring small *D*. Here, b is affected by chirp pulse length and diffusion delay. In the current experiment, the range of b is chosen from 0 ms/um^2 to 2.1 ms/um^2 which results in a relative signal decay from 1 to 0 as shown in Figure 4.7 d-f. For observing a fully decayed T_2 relaxation curve as shown in Figure 4.7 a-c, an appropriate echo time is needed with sufficient acquisition time for each echo.

4.4 Conclusion

In summary, we have demonstrated the application of hyperpolarized UF diffusion-T_2 LNMR to a homogenous high field magnet and an inhomogeneous low field, single-sided magnet. Due to spatial encoding, experimental time is reduced by several orders of magnitude which enables the use of D-DNP technique to boost experimental sensitivity. Diffusion and T_2 relaxation can be accurately obtained on both magnets using hyperpolarization technique. A combined diffusion and T_2 contrast is provided on D-T_2

maps by Laplace inversion, enhancing image resolution. This ultrafast method offers unprecedented opportunities to the application of multidimensional LNMR in various fields.

CHAPTER V

IDENTIFICATION OF INTRA- AND EXTRACELLULAR METABOLITES IN CANCER CELLS USING ^{13}C HYPERPOLARIZED ULTRAFAST LAPLACE NMR

5.1 Introduction

In cancer research, cardiovascular imaging, and diabetes research, metabolic differences between normal and diseased tissues can be accessed non-invasively by NMR.[91] Hyperpolarization by D-DNP has been shown to provide unprecedented gains in NMR signal.[29] In recent years, D-DNP has enabled the determination of metabolic pathways and measurement of metabolic flux both in cell cultures, and *in vivo* using MRI.[150,151] ^{13}C NMR of various hyperpolarized precursors, including pyruvate, glucose, bicarbonate, fumarate, and others, serve as probes for specific metabolic pathways. The observation time window of ^{13}C nuclei is wide due to their long T_1, and their broad chemical shift range facilitates the resolution of metabolites.

A challenge in studies of metabolism by NMR is that compounds inside and outside of cells are not resolved in the spectra. Furthermore, individual cells are smaller than the achieved spatial resolution in MRI. Therefore, only a combination of extracellular and intracellular locations is observed. The separation of these compartments can be achieved through measurement of diffusion.[86] Restrictions in the intracellular environment, such as macromolecular binding and boundaries due to compartmentation, lead to an intracellular diffusion coefficient of metabolites that is significantly smaller than that in the extracellular space. Diffusion MR spectroscopy therefore can be used to evaluate membrane transport, which itself can serve as a marker for tumor diagnosis.[165]

However, conventional diffusion measurements,[166,167] which require multiple incremental scans, are *a priori* not compatible with hyperpolarization, because preparation of D-DNP takes much longer than the scan time, from tens of minutes to hours. The diffusion contrast becomes available through the use of small flip angle excitations with various diffusion encoding steps. Therefore, ^{13}C hyperpolarized metabolite signals have been distinguished in different cellular compartments *in vitro* (9) and *in vivo*.[168]

Recently, we have shown that multidimensional NMR diffusion and relaxation data[56,57,169] can be measured with a single scan.[64–66] This method is termed UF-LNMR. Similar to ultrafast NMR spectroscopy[48,50,170,171] as well as single scan one-dimensional diffusion[62,158,172] and relaxation experiments,[61,63] the method is based on spatial encoding of multidimensional data. The distribution of the relaxation times and/or diffusion coefficients is obtained by a Laplace inversion.[161,173,174] The single scan approach makes it possible to use hyperpolarized substances to boost the experimental sensitivity by several orders of magnitude.[47,49,65]

Here, we demonstrate that UF-LNMR can be a powerful tool in the analysis of cell metabolism in biological samples. We introduce a spin-echo based chemical shift selective UF diffusion–T_2 relaxation correlation LNMR experiment, which enables the differentiation of intracellular and extracellular locations of ^{13}C hyperpolarized pyruvate and its metabolite product lactate in mouse 4T1 breast cancer cells. Contrary to the small flip angle diffusion measurements described above, the UF-LNMR method does not require repetition of experiment with multiple diffusion encoding steps or prior knowledge of diffusion coefficients in the compartments. Furthermore, it provides a combined *D* and

T_2 contrast, which improves the resolution of the components.

5.2 Experimental Section

5.2.1 Cell Cultures

4T1 mouse breast cancer cells were maintained as a monolayer and grown in RPMI-1640 medium (ThermoFisher Scientific, Waltham, MA) supplemented with 10% fetal bovine serum, 1% penicillin-streptomycin (10,000 U/mL) in a CO_2 incubator at 37 ^{o}C. The cells were passaged serially and used for NMR experiments between passages 3 to 5. Single cell suspensions were derived by trypsinization with 0.1% (w/v) trypsin / 0.04% (w/v) ethylenediaminetetracetic acid (EDTA) in 3 mins. For NMR measurements, cells with ~90% confluency from 8 culture plates (surface area 75 cm^2 per plate; VWR, Radnor, PA) were collected by trypsinization and centrifugation. Cells were resuspended in 0.5 mL phosphate buffer (0.2 g/L KCl, 0.2 g/L KH_2PO_4, 8.0 g/L NaCl, 1.15 g/L Na_2HPO_4, pH 7.25). The cell suspension was transferred to the first injection loop, for non-hyperpolarized sample, of a liquid driven sample injector for D-DNP NMR spectroscopy.[36] This transfer occurred shortly before the NMR experiment, in order to maintain cell viability. The number of cells was ~2.5×10^8 in the injection loop, and ~1×10^8 after injection into a flow cell pre-installed in the NMR magnet.

5.2.2 Hyperpolarization

A solution of 1 M $^{13}C_1$-pyruvate (Cambridge Isotopes, Tewksbury, MA) with 15 mM tris[8-carboxy-2,2,6,6-tetrakis(2-hydroxyethyl)benzo[1,2-d:4,5-d′]bis[1,3]-dithiol-4-yl]methyl free radical sodium salt (OX63; Oxford Instruments, Tubney Woods, U.K.) was prepared in a D_2O/ethylene glycol (2/3 v/v) glass forming mixture. An aliquot of this

sample solution was hyperpolarized on ^{13}C for 3 hours at 1.4 K in a HyperSense DNP polarizer (Oxford Instruments, Abingdon, UK), by irradiating microwaves with 60 mW power at a frequency of 93.974 GHz in a 3.35 T magnetic field. The hyperpolarized sample was rapidly dissolved in preheated phosphate buffer (10 mM Na_2HPO_4, 100 mg/L EDTA, pH 7.4), and transferred into the second loop of the liquid driven sample injector. The cell and hyperpolarized pyruvate samples were subsequently driven into a mixer, and then into a flow cell pre-installed in the magnet, using water from a high pressure syringe pump (model 1000D, Teledyne ISCO, Lincoln, NE). The final temperature was 308 K during NMR measurement. This temperature was determined by measuring a ^{1}H hyperpolarized spectrum of ethylene glycol (EG) sample (EG/D_2O (3/2, v/v); 15 mM 4-hydroxy-2,2,6,6-tetramethylpiperidine-1-oxyl (TEMPOL) free radical (Sigma-Aldrich, St. Louis, MO)) as a chemical shift thermometer (12) with the same injection time as used in the experiments. The liquid state polarization of $^{13}C_1$-pyruvate was ~ 20%.

5.2.3 NMR Experiments

Spectra were acquired on a 400 MHz NMR spectrometer with a triple resonance TXI probe (Bruker Biospin, Billerica, MA) and installed NMR flow cell. The time evolution of ^{13}C signals was determined using the pulse sequence (trigger – [G_z – α – acquire]$_{\times n}$). A total of n = 64 transients were acquired over a duration of 320 s. A pulsed field gradient G_z (45.5 G/cm, 1 ms) was applied for attenuation of coherences present from the previous scans. The small flip angle α of the excitation pulse was 10^{o}, with pulse strength $(\gamma B_1)/2\pi$ = 17.86 kHz. In each scan, a total of 12 k complex points were acquired

with an acquisition time of 0.5 s. The NMR experiment was triggered after 800 ms injection & mixing time and 5 s waiting time.

UF *D*-T_2 LNMR measurements incorporating chemical shift selection on pyruvate or lactate ^{13}C resonances at 170.4 ppm or 182.6 ppm were performed in single scans as shown in Figure 5.1.[60] The pulse sequence for Diffusion-T_2 correlation experiments was developed by Dr. Ahola and Dr. Telkki at University of Oulu. Each experiment was triggered after 0.8 s injection and 20 s reaction time.

A conventional PGSTE experiment was used for diffusion measurements without hyperpolarization, using thermally polarized ^1H signals of a pyruvate sample previously used in the hyperpolarized *D*-T_2 measurement without cell suspension (Figure 5.2). This pulse sequence consisted of $[p1 - G1 - p1 - \tau_1 / G2 - p1 - G3 - acquire]_{\times n}$. 90° hard pulses P1 were applied with $(\gamma B_1)/2\pi = 28.97$ kHz. Diffusion encoding and decoding gradients, G1 and G3, respectively, were simultaneously and linearly increased from 1.17 G/cm to 55.58 G/cm with $n = 16$ steps. The diffusion time Δ, which is between the first and last 90° pulse, was 80 ms. The gradient duration δ was 0.9 ms. The delay $\tau_1 = 78.08$ ms. A homospoil gradient G2 was applied with amplitude –10.02 G/cm and duration $\delta_{homospoil} = 0.85$ ms.

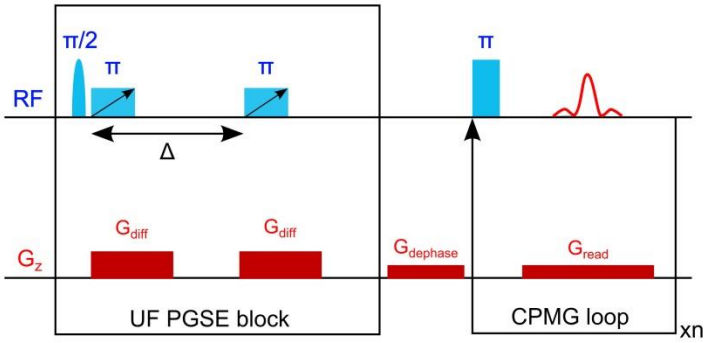

Fig. 5.1. Ultrafast Pulsed Field Gradient Spin Echo (UF-PGSE) pulse sequence for D-T_2 correlation with chemical shift selective excitation. The first π/2 was a selective 90° Gaussian pulse with 1% truncation level, applied at the center of a ^{13}C resonance. The pulse duration was 8488 μs and excitation bandwidth was 249 Hz. The following two π pulses were frequency swept chirp pulses with 10 % smoothing on the edges. The pulse duration (t_{chirp}) was 2.5 ms, bandwidth was 48.7 kHz, and $(\gamma B_{1max})/2\pi$ = 3.94 kHz. The power of the π pulse in the CPMG loop was $(\gamma B_1)/2\pi$ = 17.86 kHz. Pulsed field gradients were trapezoidal shaped with ramp time of 1 ms. Gradients are applied with amplitudes G_{diff} = 36.4 G/cm, $G_{dephase}$ = 2.3 G/cm, G_{read} = 2.3 G/cm, and durations $t_{G,diff}$ = 5.0 ms, $t_{G,dephase}$ = 8.9 ms, $t_{G,read}$ = 16.9 ms. The diffusion delay is Δ = 50 ms. The simultaneously applied G_{diff} and frequency swept π pulse resulted in a spatial dependence of the effective length of G that a spin experiences in the range of δ_{eff} = 0…5 ms. The spectral width was 25 kHz. The total experiment time was t_{exp} = 1.4 s. The resulting two dimensional D-T_2 data comprises a time (T) and a spatial frequency (S) dimension for obtaining T_2 and D, respectively. In the T dimension, n = 64 CPMG echoes are collected with CPMG loop time of 0.02 ms interval. Fourier transform of each echo leads to m = 256 complex points in the S dimension encoded in the UF PGSE block.

The z-gradient strength was calibrated using a H_2O sample with known diffusion coefficient of $2.3 \cdot 10^{-9}$ m^2/s at T = 298.2 K (Figure 5.3). A conventional PGSTE experiment was also used for calibration of z-gradient strength G. ^1H signals of thermally polarized water were measured at T = 298.2 K. The pulse sequence is the same as that used for diffusion measurement of a thermally polarized pyruvate sample (Figure 5.2). Experimental parameters are $(\gamma B_1)/2\pi$ = 28.57 kHz, Δ = 100 ms, δ = 1.1 ms, τ_1 = 98 ms and $\delta_{homospoil}$ = 0.8 ms.

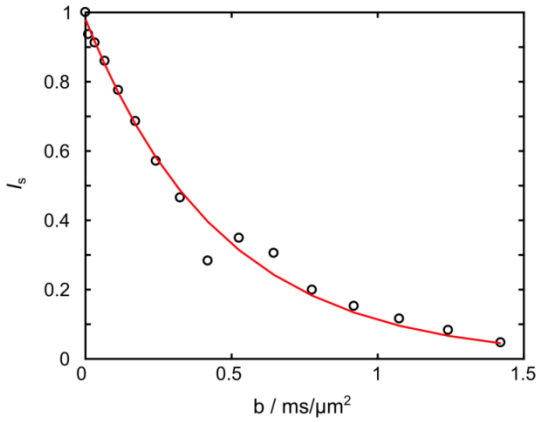

Fig. 5.2. ^{1}H NMR diffusion signal of pyruvate on its methyl proton at 308 K as a function of $b = \left(\gamma G \delta_{eff}\right)^2 \left(\Delta - \frac{\delta_{eff}}{3}\right)$, using a conventional PGSTE sequence. The spectrum was acquired under the same sample condition after the *D*-T_2 experiment of hyperpolarized pyruvate selection without cell suspension. The final pyruvate concentration is 13.5 mM. The red fitting line yields a self-diffusion coefficient of $D = (2.2 \pm 0.4) \cdot 10^{-9}$ m^2/s.

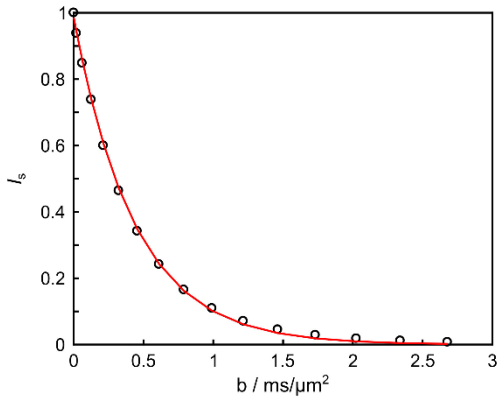

Fig. 5.3. ^{1}H NMR diffusion signal of H_2O at 25 °C as a function of $b = \left(\gamma G \delta_{eff}\right)^2 \left(\Delta - \frac{\delta_{eff}}{3}\right)$, using a conventional PGSTE sequence. The fitted curve using is shown in red. Using a self-diffusion coefficient of $D_{water} = 2.3 \cdot 10^{-9}$ m^2/s from published values,[159] the z-gradient strength G was calibrated as 6.5 G/mm.

Residual motions in the sample after injection were assessed using a single scan ultrafast *D*-T_2 measurement using the pulse sequence as shown in Fig. 5.1. As shown in Figure 5.4 (see Table 5.1 for experimental parameters), the sample was already stationary

after 20 s stabilization, with an apparent diffusion coefficient of $(3.3 \pm 1.0) \cdot 10^{-9}$ m^2/s, compared to the reference value of $2.9 \cdot 10^{-9}$ m^2/s.[159] The agreement of these diffusion coefficients within error limits indicates that the D-DNP sample is nearly stationary during data acquisition, validating the stopped-flow injection into the NMR flow cell. In this approach, the flow path is pinched both in the inlet and outlet tubing after delivering the sample into the cell, therefore preventing large scale flow of the sample during NMR measurement.[36]

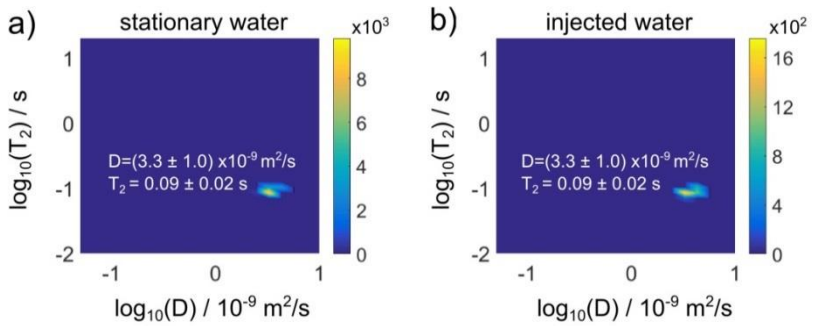

Fig. 5.4. a) *D*-T_2 map of stationary water in the flow cell at 308 K. D value agrees well with published value which is 2.9×10^{-9} m^2/s at 308 K. b) *D*-T_2 map of water injected into the flow cell. 8µL of water was loaded into the DNP polarizer and transferred to the flow cell without hyperpolarization. Injection procedures were the same as the actual hyperpolarized *D*-T_2 measurement. The measurement was triggered after the 20 s waiting time. The final temperature after injection is 308 K.

Table 5.1. Experimental parameters for *D*-T_2 measurement of thermally polarized water.

π/2 Gaussian pulse duration	2122 µs
π/2 Gaussian pulse excitation bandwidth	996 Hz
t_{chirp}	2.0 ms
chirp pulse bandwidth	34.1 kHz
chirp pulse $(\gamma B_{1max})/2\pi$	3.7 kHz

Table 5.1. Continued.

π pulse (CPMG loop) $(\gamma B_1)/2\pi$	29.1 kHz
G_{diff}	10.7 G/cm
$G_{dephase}$	7.8 G/cm
G_{read}	7.8 G/cm
$t_{G,diff}$	4.0 ms
$t_{G,dephase}$	4.1 ms
$t_{G,read}$	7.2 ms
Δ	100 ms
t_{CPMG}	[0.02 s, 1.28 s] with interval 0.02 s
δ_{eff}	[0 ms, 4 ms]
points in the T_2 dimension	64
complex points in the diffusion dimension	256
spectral width	100 kHz
scan number for stationary water	5
d1 for stationary water	5 s
t_{exp} for stationary water	33 s
scan number for injected water	1
t_{exp} for injected water	2 s

Furthermore, no gas bubbles were observed at the time of measurement, which was also confirmed by a one-dimensional imaging experiment (Figure 5.5). A pulsed field gradient echo experiment was used for this measurement. The pulse sequence consists of elements [p1 – G1 – τ1 – p2 – G2 / acquire]. P1 and P2 are 90^o and 180^o hard pulses with $\gamma B_1/(2\pi)$ = 27.03 kHz. G1 and G2 are denoted as defocusing and refocusing pulsed field gradients with gradient strength 1.95 G/cm. The gradient duration of G2 = 17.88 ms is twice as long as that of G1. The delay τ1 = 1.05 ms. The coincidence of red and black

curves in Figure S4 demonstrates that no gas bubbles were observed after 15 s waiting time.

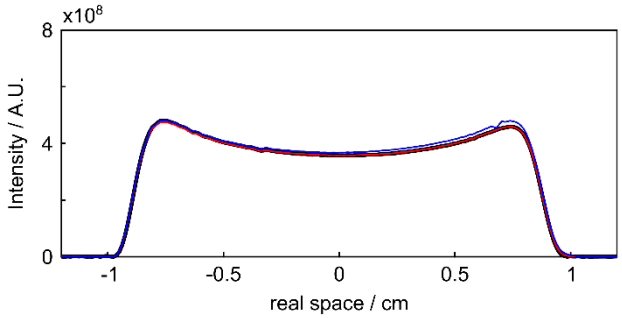

Fig.5.5. Coil image profiles. 8 µL water was loaded into the DNP polarizer and injected using the same procedures as for the actual hyperpolarized *D*-T_2 measurement. A first measurement were triggered after a waiting time of 10 s (blue curve), and a second measurement after 15 s (red curve). As a reference, an image was obtained by acquiring signal of static water in the flow cell (black curve).

5.2.4 Data Analysis

For determining time evolution from ^{13}C NMR spectra, the raw data was filled to 65536 complex data points and multiplied with an exponential window function with a line broadening of 0.3 Hz before Fourier transform, using TOPSPIN 3.5 (Bruker Biospin). All Peak integration and curve fitting were conducted using the Matlab program (MathWorks, Natick, MA).

For the analysis of *D*-T_2 data, the 2D relaxation time and diffusion coefficient distributions were determined using a Laplace inversion program provided by P. Callaghan (Victoria University of Wellington, New Zealand)[160] and based on a previously published method.[161] For *D*-T_2 experiments with hyperpolarized $^{13}C_1$-pyruvate. The number of samples in the T and S dimensions were 64 and 19, respectively. In order to

reduce noise, the size of the data matrix was compressed to 25 × 19 points using singular value decomposition. NNLS with Tikhonov regularization was then performed over the data ranges δ_{eff} = [0.94 ms, 3.75 ms], corresponding to diffusion decay of the signal, and t_{CPMG} = [0.02 ms, 1.28 ms], for the target ranges T_2 = [0.01 s, 50 s] and D = [5×10^{-11} m^2/s, 10^{-8} m^2/s].

For D-T_2 experiments with water, a range of δ_{eff} = [0.87 ms, 2.63 ms] corresponding to the diffusion decay of the signal, and t_{CPMG} = [0.02 ms, 1.28 ms] was used. The size of the data matrix was 64 × 29, which was compressed to 40 × 20 by reducing the number of samples in both T and S dimensions using singular value decomposition. Correlation diagrams with ranges T_2 = [0.01 s, 20 s] and D = [5×10^{-11} m^2/s, 10^{-8} m^2/s] were computed using NNLS minimization with Tikhonov regularization.

The simulation of D-T_2 data (see Figure 4.8) are described elsewhere.[65] Briefly, the echo amplitudes are calculated using the equation: $E(k,l) = S_{max}\exp[-D\gamma^2\delta_{eff}(k)^2G_{diff}^2\Delta]\exp[-t(l)\left(-\frac{1}{T_2'}-\beta\right)]$, where S_{max} is the signal amplitude, D is diffusion coefficient, δ_{eff} [0 ms, 5 ms] is effective length of G, G = 36.4 G/cm is gradient strength, Δ = 50 ms is diffusion delay, and T_2' is relaxation time that would be observed in the absence of a gradient, $\beta = (\delta\gamma^2G_{read}^2te^2D)/\pi^4$ is the diffusive attenuation factor, which further depends on echo time of the first echo te = 20 ms and G_{read} = 2.3 G/cm. All parameter settings, as indicated, are the same as in the experiment. For the simulation, data was generated using the above equation in Matlab. Normally distributed noise was added using matlab function "randn". The simulated data was then processed using the same method as the experimental data in Figure 5.7.

5.3 Results and Discussion

5.3.1 Turnover of Hyperpolarized Pyruvate

The time evolution of a series of 1D ^{13}C spectra of hyperpolarized $^{13}C_1$-pyruvate with 4T1 cancer cells injected into the NMR flow cell is shown in Figure 5.6a. The ^{13}C signal of pyruvate appears at 170.4 ppm, and the metabolic product lactate is visible at 182.6 ppm. A further signal at 178.7 ppm corresponds to pyruvate hydrate, which is formed by a non-biological process. The observation of a strong lactate signal is expected for cancer cells, where the glycolytic pathway is strongly favored even in the presence of sufficient oxygen (Figure 5.6b).[175] Due to the combined effects of reaction kinetics, T_1 relaxation and radio frequency pulses,[115] the pyruvate signal shows a monoexponential decay, which is paralleled by an initial increase of lactate signal. The integrated lactate signal reaches its maximum after 20 s (Figure 5.6c). At that point, it is approximately 12.5 times lower than the initial signal of pyruvate (Figure 5.6c). A lower signal of the metabolic product is also expected due to the interplay of the different rate constants affecting the signal. Changes in the signal intensities, $M_{z,pyr}$ and $M_{z,lac}$, can be quantitatively modeled:

$$\frac{dM_{z,pyr}(t)}{dt} = -k_{pyr-lac} \times M_{z,pyr}(t) - \left(R_{1,pyr} + \lambda\right) \times M_{z,pyr}(t) \quad (4.1)$$

$$\frac{dM_{z,lac}(t)}{dt} = k_{pyr-lac} \times M_{z,pyr}(t) - \left(R_{1,lac} + \lambda\right) \times M_{z,lac}(t) \quad (4.2)$$

The observed rate constant for the conversion from pyruvate to lactate, $k_{pyr\text{-}lac}$, depends on the cell density in the experiment. It includes contributions from the lactate dehydrogenase activity, as well as from the membrane transport of pyruvate. $R_{1,pyr}$ and

$R_{1,lac}$ are the relaxation rates on the carbonyl sites. The parameter $\lambda = -\ln(\cos(\alpha))/\Delta t$, with $\alpha = 10^{o}$ and $\Delta t = 5$ s the time interval between two scans, accounts for signal depletion due to the small flip angle pulses. For the experimental data from Figure 5.6c, the resulting fit parameters are $k_{pyr\text{-}lac} = 6.5 \cdot 10^{-3}$ s^{-1} under the given experimental conditions with ~1×10^{8} 4T1 cancer cells, $T_{1,pyr} = 41$ s and $T_{1,lac} = 19$ s. The T_1 values match the values reported for an *in vitro* experiment using T47D human breast cancer cells ($T_{1,pyr}$ ~45 s and $T_{1,lac}$ ~19 s).[152]

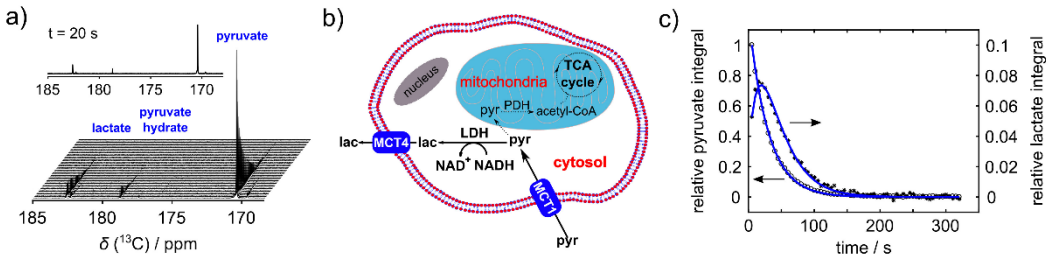

Fig. 5.6. a) Stacked plots of a series of ^{13}C spectra from hyperpolarized $^{13}C_1$-pyruvate with 4T1 cancer cells. The inset shows the spectrum at the time point of 20 s, where the *D*-T_2 measurements were performed. b) Scheme of a cancer cell, indicating membrane transport of pyruvate and lactate, as well as the associated metabolic pathways (21). MCT; monocarboxylate transporters, LDH; lactate dehydrogenase, PDH; pyruvate dehydrogenase. c) Integrals and kinetic fit of pyruvate and lactate signals as a function of time. All signal integrals were normalized with the maximum pyruvate signal integral.

5.3.2 Ultrafast D-T_2 maps

UF *D*-T_2 maps were measured from hyperpolarized $^{13}C_1$-pyruvate, as well as from hyperpolarized $^{13}C_1$-pyruvate mixing with 4T1 cells (Figure 5.7). After a waiting time of 20 s after sample injection, the *D*-T_2 data of pyruvate or lactate was acquired by selectively exciting either one of the metabolite signals. Hyperpolarized pyruvate without cell suspension results in a single signal with $T_2 = (6.0 \pm 2.0)$ s and $D = (3.1 \pm 0.8) \cdot 10^{-9}$ m^2/s

(Figure 5.7a). This diffusion coefficient is consistent with that obtained using a conventional PGSTE pulse sequence on a stationary, non-hyperpolarized sample at T = 308 K, which yielded $D = (2.2 \pm 0.4) \cdot 10^{-9}$ m^2/s (Figure 5.2). The T_2 value obtained from hyperpolarized pyruvate is shortened compared to values that would be obtained with a basic spin-echo pulse sequence due to the magnetic field gradients.

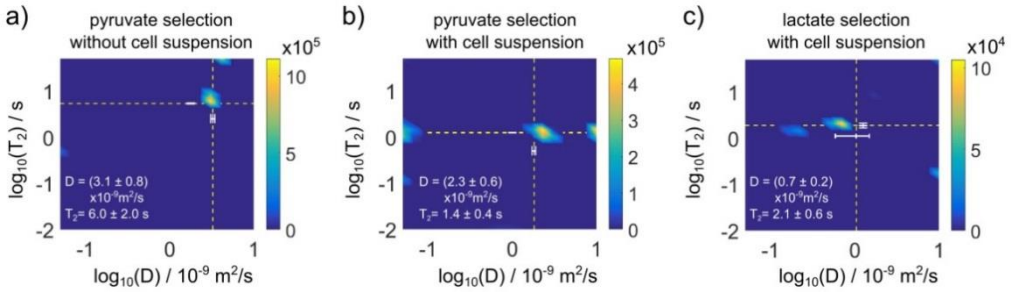

Fig. 5.7. D-T_2 map including a) pyruvate selection without cell suspension, b) pyruvate selection with cell suspension and c) lactate selection with cell suspension. The D and T_2 values correspond to the peaks with maximum intensities. The uncertainties are estimated from peak width. The dashed lines and white bars are results from the exponential fits of single D and T_2 curves. For D values (Figure 5.10) the bars represent errors given from the standard deviation of D values obtained from each of the echoes. For T_2 values (Figure 5.9b), the bars represent 95% confidence intervals from the fit of a single exponential.

In the presence of cell suspension, the signal obtained with selective excitation of the pyruvate $^{13}C_1$-resonance shifts to smaller T_2 and D values of (1.4 ± 0.4) s and (2.3 ± 0.6) $\cdot 10^{-9}$ m^2/s, respectively (Figure 5.7b). These changes can be explained by the higher viscosity of the cell suspension. A D-T_2 map acquired in a separate experiment with selective excitation of the lactate resonance is shown in Figure 3c. It can be seen that the diffusion coefficient of lactate is 3 fold lower than that of pyruvate. Since pyruvate and lactate show similar diffusion coefficients in aqueous solution alone,[176] the observed

difference suggests that, here, the two signals stem from different environments. Pyruvate is converted into lactate in the cytoplasm, and therefore the lower diffusion coefficient of lactate is explained by restricted diffusion inside the cells due to increased viscosity, compartmentalization and interactions with macromolecules. At the same time, this data indicates that lactate that is exported from cells, at the time of measurement does not significantly contribute the observed signal. Conversely, the primary pyruvate pool in this experiment appears to be extracellular.

D_{lac} and D_{pyr} obtained from Laplace inversion in Figure 5.7b and 5.7c can also be compared with literature values. They are consistent with $D_{lac} = (0.8\pm0.2) \cdot 10^{-9}$ m^2/s and $D_{pyr} = (1.7\pm0.6) \cdot 10^{-9}$ m^2/s values measured using a surface coil in EL-4 murine lymphoma tumor *in vivo* at 37 ºC by Kettunen et al..[177] They are also consistent with $D_{pyr} = (1.94\pm0.07) \cdot 10^{-9}$ m^2/s and $D_{lac} = (1.06\pm0.15) \cdot 10^{-9}$ m^2/s measured in MCF-7 tumor cell spheroids *in vitro* at 37 ºC, from Schilling et al..[85] In these reference values, the observed D_{pyr} is presumed to predominantly stem from an extracellular pool of pyruvate and the observed D_{lac} predominantly from an intracellular pool of its metabolite product lactate. Therefore the comparison confirms the reliability of the UF LNMR method.

The current ultrafast experiment employs a 90º selective pulse to excite a metabolite peak of interest. Such selection may be advantageous for spectra with multiple peaks, simplifying the identification of peaks. Furthermore, here, a data set recorded without selective excitation did not show multiple resolved signals. The ratio of pyruvate to lactate signal intensity is ~ 10, with the SNR of $^{13}C_1$-pyruvate ~ 170. This SNR was calculated as the ratio of the maximum intensity of the echoes to the standard deviation

value of noise points. Noise points included the first 4 and last 4 points from the acquisition period of each echo, concatenated to comprise a total of $2\times4\times n$ points. Such SNR may not be sufficient to resolve these two components as shown in a previous simulation.[65] Multiple components that cannot be resolved in the Laplace inversion due to low SNR, can however be resolved through chemical shift selective excitation as demonstrated here.

5.3.3 Spread of Observed T_2 -values

Comparing the panels in Figure 5.7, it can be seen that the observed T_2 values in each case are different. While a slightly reduced T_2 in (b) would be expected due to the higher viscosity of the sample compared to (a), which leads to longer rotational correlation time, an increase in T_2 in (c) cannot be explained in this way. Another effect that needs to be taken into consideration is a coupling between diffusion and T_2 relaxation measurement.[164] A magnetic field gradient at the time of signal acquisition increases the echo attenuation due to molecular self-diffusion. The resulting echo intensity is $S = S_0 \cdot \exp[t \cdot (-1/T_2' - \beta)]$, where T_2' is the relaxation time that would be observed in the absence of a gradient, and $\beta = (8\gamma^2 G_{read}^2 te^2 D)/\pi^4$ is a diffusive attenuation factor with te echo time of the first echo. Therefore, depending on the relative magnitude of the changes in β and T_2', the observed T_2 can increase or decrease. A calculation of this effect for the conditions observed in the lactate and pyruvate signals is shown in Figure 5.8. Irrespective of the origin of the observed changes in T_2, this parameter takes a different value for each of the species observed in Figure 5.7, thereby improving the contrast between the species.

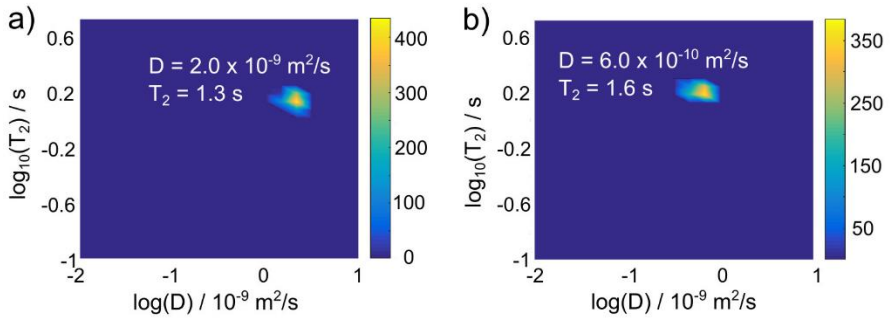

Fig. 5.8. a) Simulated D-T_2 map of molecule A with $D = 2.0 \cdot 10^{-9}$ m^2/s. b) Simulated D-T_2 map of molecule B with $D = 6.0 \cdot 10^{-10}$ m^2/s. Relaxation time T_2', which is observed in the absence of a gradient, is 1.7 s for both A and B.

5.3.4 Analysis of Single D and T_2 Traces

Under the assumption that there is only one signal component in these data sets, the Laplace inversions can be compared to single D or T_2 traces from the same data set. The Fourier transform of hyperpolarized D-T_2 data in each echo leads to 64 columns in the T dimension, corresponding to 64 diffusion curves (Figure 5.10). Signals from the 8th columns of hyperpolarized data are plotted in Figure 4a as a function of b values. Fitting diffusion curves of each data set results in mean D values as shown in Figure 5.10. T_2 values are derived by Fourier transform and integration of hyperpolarized D-T_2 data along the time dimension (Figure 5.9c). As shown in Figure 5.7, the D and T_2 values of the D-T_2 maps match those from the individual trace analysis.

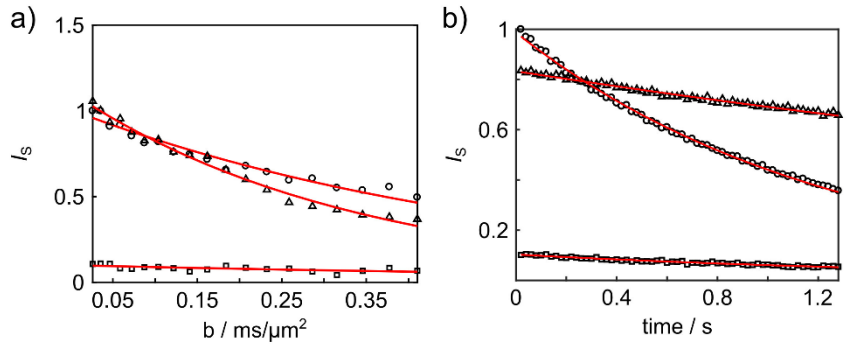

Fig. 5.9. a) Signals from the 8th columns of hyperpolarized *D*-T_2 data, shown in the S dimension as a function of $b = \left(\gamma G \delta_{eff}\right)^2 \left(\Delta - \frac{\delta_{eff}}{3}\right)$. Triangle, circle and square symbols stand for hyperpolarized *D*-T_2 data of pyruvate selection without cell suspension, pyruvate selection with cell suspension and lactate selection with cell suspension, respectively. Signals are normalized to the maximum signal amplitude of hyperpolarized *D*-T_2 data set with circle symbols. Fitted curves using the Stejskal–Tanner signal equation $I_s = I_0 \cdot \exp(-b \cdot D)$ are shown in red. The fitting results are D = (2.97 ± 0.11) m²/s, (1.89 ± 0.37) m²/s and (1.19 ± 0.55) m²/s for curves with triangle, circle and square symbols. b) Integral of each hyperpolarized *D*-T_2 data along S dimension are shown as a function of t_{CPMG}. Symbols represent the same data sets shown in (a). The integral comprises the range shown in (a). Signals are normalized to the maximum integral with shortest *t*. Integrals are fitted with $I_s = I_0 \cdot \exp(-\frac{t}{T_2})$. The fitting results are T_2 = (5.35 ± 0.17) s, (1.24 ± 0.01) s and (1.88 ± 0.30) s for curves with triangle, circle and square symbols.

In this experiment, spatial encoding results in the same spectra as that in conventional diffusion experiment, but in a single scan. Therefore, the acquisition time can be reduced by several orders of magnitude compared to conventional measurement. Here, sensitivity is enhanced by the use of hyperpolarization. This makes it possible to measure diffusion and T_2 relaxation based on ^{13}C signals, of pyruvate and lactate with concentrations as low as ~ 10 mM and ~ 1 mM, and within 1.4 s. The detection of ^{13}C signal may have more specificity, in particular in complex samples containing many metabolites.

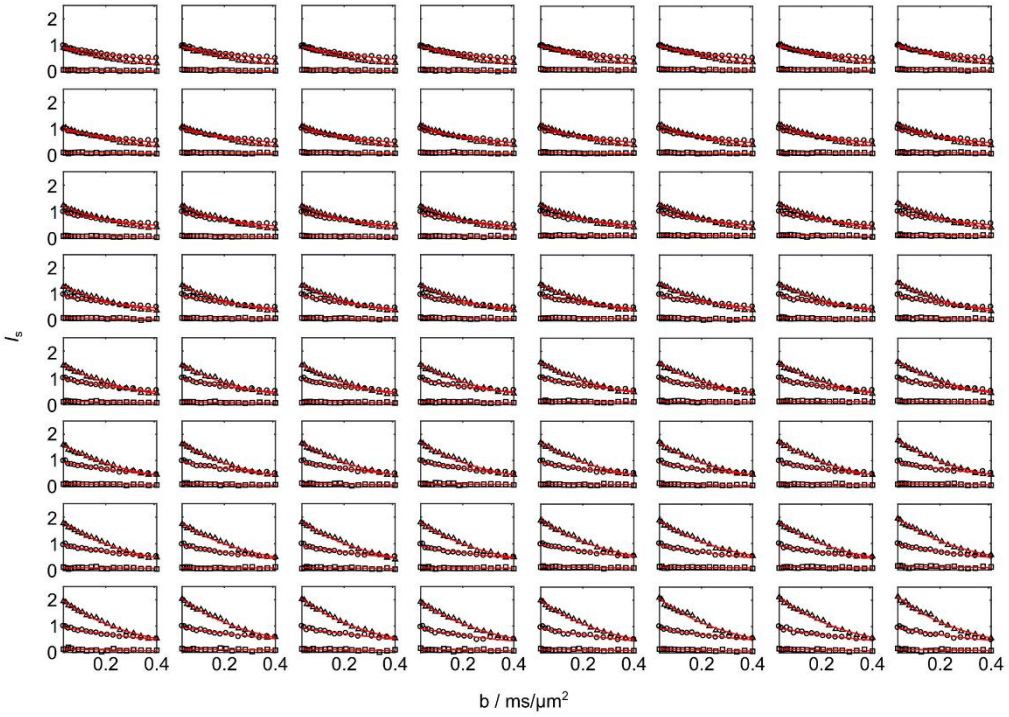

Fig. 5.10. Signals from 64 columns of hyperpolarized *D*-T_2 data after Fourier transform of each echo along the S dimension, shown as a function of b and fitted with $I_s = I_0 \cdot \exp(-b \cdot D)$ (red curve). $b = \left(\gamma G \delta_{eff}\right)^2 \left(\Delta - \frac{\delta_{eff}}{3}\right)$ ranged from 0.026 ms/μm^2 to 0.410 ms/ μm^2. Each panel corresponds to signal decay from a column of the corresponding data set. The column number increases from left to right starting from the top row. Within each panel, triangle, circle and square symbols stand for hyperpolarized *D*-T_2 data of pyruvate selection without cell suspension, pyruvate selection with cell suspension and lactate selection with cell suspension, respectively. The *D* values from the fit are averaged as mean $D = (3.26 \pm 0.18) \cdot 10^{-9}$ m^2/s, $(1.81 \pm 0.09) \cdot 10^{-9}$ m^2/s and $(1.04 \pm 0.45) \cdot 10^{-9}$ m^2/s for the three experiments, respectively. The errors are from the standard deviation of *D* values. In each panel, signals are normalized to the maximum signal amplitude of pyruvate selection with cell suspension experiment.

The identification of intracellular metabolite is of importance for the interpretation of rate constants obtained from *in vitro* metabolic studies using D-DNP hyperpolarization. Specifically, a potential application of this method is the assessment of membrane permeability. Necrosis of cancer cells due to the use of anticancer drugs can cause cell

membrane to lose its selectivity. Molecules, which are normally transported across cell membrane by transmembrane proteins, are free to diffuse in or out of cells more rapidly. Schilling *et al.*[85] has reported a decreased ratio of D_{pyr} over D_{lac} as the fraction of dead cell increases during progressive membrane permeabilization. This ratio can serve as a biomarker for monitoring the pathological changes and treatment response in cancer. Secondly, it has been found that up-regulation of MCT is associated with malignancy of cancer cells.[178] By measuring the change of intra- and extracellular proportion of metabolites, such as lactate, as a function of time after the injection of hyperpolarized precursor, such as pyruvate, transport rates can be derived which opens the way to assess the activity of MCTs.[83]

5.4 Conclusion

In summary, we have described ultrafast D-T_2 correlation LNMR as a tool to distinguish intra- vs. extracellular metabolites in the study of cellular metabolism. This experiment simultaneously provides contrast in the diffusion and T_2 relaxation parameters, therefore enhancing the ability to localize a metabolite. The correlation map can be acquired in a single scan, resulting in a shorter experiment time than for other diffusion measurements. The single scan nature also renders the method inherently compatible with the use of non-renewable hyperpolarization to provide a large sensitivity enhancement. Using ^{13}C hyperpolarization, we demonstrated the identification of pools of intracellular lactate and extracellular pyruvate in cultures of mouse 4T1 breast cancer cells by this method. For determining diffusion by Laplace inversion, no prior knowledge of the value of the diffusion coefficient or the number of components that are present is required.

Beyond the measurement of diffusion, the basic scheme of hyperpolarized UF LNMR can further be adapted to investigate other parameters for characterizing dynamic and exchange processes.

CHAPTER VI

GENERAL CONCLUSIONS

Dissolution DNP enhanced NMR, boosting experimental sensitivity by several orders of magnitude, has extensive applications in chemistry and biochemistry. This technique allows polarization of a variety of nuclei, such as ^{1}H, ^{13}C, ^{19}F and ^{15}N. The significantly enhanced signal facilitates structural elucidation of molecules with limited mass or concentration. Additionally, it enables to track hyperpolarized spins for investigation of fast non-equilibrium processes, with the goal of studying reaction dynamics and mechanisms. However, challenges in dissolution DNP enhanced NMR still exist. The limited life time and non-renewability of hyperpolarized states require data acquisition accomplished in a single scan. At the same time, all necessary information, which can be obtained by conventional experiments with multiple scans, needs to be extracted from a single-scan approach. In the present dissertation, methods have been developed to accomplish this goal and applied to identify structures and physical properties of molecules.

Structural determination frequently relies on correlation spectroscopy. Heteronuclear correlations of chemical shifts in single scan NMR spectra are determined by an off-resonance decoupling scheme, using the method of SHOT. Through modulation of *J*-coupling evolution by shaped radio frequency pulses, off resonance decoupling using SHOT pulses causes a user-defined dependence of the observed *J*-splitting. [^{13}C, ^{1}H] chemical shift correlations of transient species from hyperpolarized styrene polymerization were calculated based on the *J*-splitting constants. In addition, a novel

SHOT pulse is presented that allows to scale *J*-splittings 50% larger than the respective *J*-coupling constant. This feature can be used to enhance the resolution of the indirectly detected chemical shift and reduce peak overlap. While off resonance decoupling by SHOT pulses does not enhance the resolution in the same way as a 2D NMR spectrum would, the ability to obtain the correlations in single scans makes this method ideal for determination of chemical shifts in on-going reactions, such as tracking the fate of metabolites over time.

Physical properties of molecules, such as diffusion and spin relaxation, can further be characterized with single-scan correlation methods and used to examine membrane transport of metabolite. UF-LNMR, which is based on the spatial encoding of multidimensional data, enables one to carry out 2D relaxation and diffusion measurements in a single-scan. Besides reducing the experiment time to a fraction, it significantly facilitates the use of nuclear spin hyperpolarization to boost experimental sensitivity, because the time consuming polarization step does not need to be repeated.

Diffusion-T_2 correlation data was obtained by acquiring hyperpolarized signals of small molecules in a single scan, and two-dimensional maps are generated from ultrafast time-domain data using an inverse Laplace transform. The experiments were conducted in a homogeneous / high field magnet as well as an inhomogeneous / low field magnet. Diffusion coefficient and T_2 relaxation determined by UF-LNMR matched the values measured using conventional approaches, demonstrating the robustness of the method. Contrary to the small flip angle diffusion methods reported in the literature, the UF-LNMR does not require several scans with varying gradient strength, and it provides a combined

diffusion and T_2 contrast.

The usability of hyperpolarized UF-LNMR is then demonstrated in the context of cell metabolism, allowing the determination of the extra-vs. intracellular location of metabolites in mouse 4T1 cancer cells. With the acquisition of ^{13}C NMR signals, metabolites can be distinguished via chemical shift. The inherently low sensitivity of ^{13}C NMR spectroscopy is overcome by hyperpolarization using D-DNP. NMR signals are enhanced by several orders of magnitude to allow acquisition of the correlation data in a single scan. Two-dimensional maps are generated from ultrafast time-domain data using an inverse Laplace transform. In cultures of mouse 4T1 cancer cells, the conversion of pyruvate to lactate is observed. Correlation maps acquired with selective excitation at the chemical shifts of these two metabolites result in $D = (2.3 \pm 0.6) \times 10^{-9}$ m^2/s and $T_2 = (1.4 \pm 0.4)$ s; and $D = (0.7 \pm 0.2) \times 10^{-9}$ m^2/s and $T_2 = (2.1 \pm 0.6)$ s, respectively. These signals are interpreted as arising from a predominantly extracellular pool of pyruvate, and a predominantly intracellular pool of lactate. A significant difference both in observed D and $T2$ parameters indicates the ability to distinguish these pools.

The work focused in the present dissertation illustrated some powerful application of D-DNP enhanced NMR to study chemical and biological reactions using fast correlation methods. The significantly enhanced NMR signal enables acquisition of single scan spectra, both in steady state and non-equilibrium processes. The investigation and characterization of molecular structures, kinetics and physical properties of metabolites provides important insights into reaction mechanism and biological processes.

REFERENCES

(1) Ernst, R. R.; Bodenhausen, G.; Wokaun, A., *Principles of Nuclear Magnetic Resonance in One and Two Dimensions*. Oxford: Clarendon Press, **2004**.

(2) Hills, B. P., *Encyclopedia of Magnetic Resonance*. Chichester: John Wiley & Sons, Ltd, **2009**.

(3) Ardelean, I.; Kimmich, R., *Annual Reports on NMR Spectroscopy*. Amsterdam: Elsevier, **2003**.

(4) Bible, R. H., *Interpretation of NMR Spectra : an Empirical Approach*. New York: Plenum Press, **1965**.

(5) Gutowsky, H. S. *Annu. Rev. Phys. Chem.* **1954**, *5* (1), 333–356.

(6) Shoolery, J. N. *Anal. Chem.* **1954**, *26* (9), 1400–1403.

(7) Lipchock, J. M.; Loria, J. P., *Protein Structure, Stability, and Interactions*. Totowa: Humana Press, **2009**.

(8) Davis, B., *Protein-Ligand Interactions*. Totowa: Humana Press, **2013**.

(9) Wüthrich, K., *NMR of Proteins and Nucleic Acids*. New York: Wiley, **1986**.

(10) Sanders, J. K. M.; Hunter, B. K., *Modern NMR Spectroscopy: a Guide for Chemists*. Oxford: Oxford University Press, **1993**.

(11) Tomlins, A. M.; Foxall, P. J. D.; Lynch, M. J.; Parkinson, J.; Everett, J. R. *et al. Biochim. Biophys. Acta* **1998**, *1379* (3), 367–380.

(12) Mlynárik, V. *Anal. Biochem.* **2016**, *529*, 4–9.

(13) Hoult, D. I.; Richards, R. E. *J. Magn. Reson.* **1976**, *24* (1), 71–85.

(14) Ardenkjær-Larsen, J.-H.; Boebinger, G. S.; Comment, A.; Duckett, S.; Edison, A. S. *et al. Angew. Chem. Int. Ed.* **2015**, *54* (32), 9162–9185.

(15) Kelly, A. E.; Ou, H. D.; Withers, R.; Dötsch, V. *J. Am. Chem. Soc.* **2002**, *124* (40), 12013–12019.

(16) Overhauser, A. W. *Phys Rev* **1953**, *92* (2), 411–415.

(17) Carver, T. R.; Slichter, C. P. *Phys. Rev.* **1953**, *92* (1), 212–213.

(18) Nikolaou, P.; Coffey, A. M.; Barlow, M. J.; Rosen, M. S.; Goodson, B. M. *et al. Anal. Chem.* **2014**, *86* (16), 8206–8212.

(19) Nikolaou, P.; Goodson, B. M.; Chekmenev, E. Y. *Chem. - Eur. J.* **2015**, *21* (8), 3156–3166.

(20) Keshari, K. R.; Wilson, D. M. *Chem. Soc. Rev.* **2014**, *43* (5), 1627–1659.

(21) Hu, K.-N.; Debelouchina, G. T.; Smith, A. A.; Griffin, R. G. *J. Chem. Phys.* **2011**, *134* (12), 125105.

(22) Becerra, L. R.; Gerfen, G. J.; Temkin, R. J.; Singel, D. J.; Griffin, R. G. *Phys. Rev. Lett.* **1993**, *71* (21), 3561–3564.

(23) Ardenkjær-Larsen, J. H.; Laursen, I.; Leunbach, I.; Ehnholm, G.; Wistrand, L.-G. *et al. J. Magn. Reson.* **1998**, *133* (1), 1–12.

(24) Haze, O.; Corzilius, B.; Smith, A. A.; Griffin, R. G.; Swager, T. M. *J. Am. Chem. Soc.* **2012**, *134* (35), 14287–14290.

(25) Lee, Y. *Appl. Spectrosc. Rev.* **2016**, *51* (3), 210–226.

(26) Ni, Q. Z.; Daviso, E.; Can, T. V.; Markhasin, E.; Jawla, S. K. *et al. Acc. Chem. Res.* **2013**, *46* (9), 1933–1941.

(27) Hu, K.-N.; Yu, H.; Swager, T. M.; Griffin, R. G. *J. Am. Chem. Soc.* **2004**, *126* (35), 10844–10845.

(28) Song, C.; Hu, K.-N.; Joo, C.-G.; Swager, T. M.; Griffin, R. G. *J. Am. Chem. Soc.* **2006**, *128* (35), 11385–11390.

(29) Ardenkjær-Larsen, J. H.; Fridlund, B.; Gram, A.; Hansson, G.; Hansson, L. *et al. Proc. Natl. Acad. Sci.* **2003**, *100* (18), 10158–10163.

(30) Günther, U. L., *Modern NMR Methodology*. Berlin: Springer, **2011**.

(31) Karlsson, M.; Jensen, P. R.; Duus, J. Ø.; Meier, S.; Lerche, M. H. *Appl. Magn. Reson.* **2012**, *43* (1–2), 223–236.

(32) Jähnig, F.; Kwiatkowski, G.; Ernst, M. *J. Magn. Reson.* **2016**, *264*, 22–29.

(33) Bowen, S.; Hilty, C. *Phys. Chem. Chem. Phys.* **2010**, *12* (22), 5766.

(34) Bowen, S.; Hilty, C. *Angew. Chem. Int. Ed.* **2008**, *47* (28), 5235–5237.

(35) Granwehr, J.; Panek, R.; Leggett, J.; Köckenberger, W. *J. Chem. Phys.* **2010**, *132* (24), 244507.

(36) Chen, H.-Y.; Hilty, C. *ChemPhysChem* **2015**, *16* (12), 2646–2652.

(37) Leggett, J.; Hunter, R.; Granwehr, J.; Panek, R.; Perez-Linde, A. J. *et al. Phys. Chem. Chem. Phys.* **2010**, *12* (22), 5883.

(38) Sharma, M.; Janssen, G.; Leggett, J.; Kentgens, A. P. M.; van Bentum, P. J. M. *J. Magn. Reson.* **2015**, *258*, 40–48.

(39) Cheng, T.; Mishkovsky, M.; Bastiaansen, J. A. M.; Ouari, O.; Hautle, P. *et al. NMR Biomed.* **2013**, *26* (11), 1582–1588.

(40) Halse, M. E. *TrAC Trends Anal. Chem.* **2016**, *83*, 76–83.

(41) Levitt, M. H. *Annu. Rev. Phys. Chem.* **2012**, *63* (1), 89–105.

(42) Ahuja, P.; Sarkar, R.; Jannin, S.; Vasos, P. R.; Bodenhausen, G. *Chem. Commun.* **2010**, *46* (43), 8192.

(43) Vasos, P. R.; Comment, A.; Sarkar, R.; Ahuja, P.; Jannin, S. *et al. Proc. Natl. Acad. Sci.* **2009**, *106* (44), 18469–18473.

(44) Bornet, A.; Jannin, S.; Bodenhausen, G. *Chem. Phys. Lett.* **2011**, *512* (4–6), 151–154.

(45) Giraudeau, P.; Frydman, L. *Annu. Rev. Anal. Chem.* **2014**, *7* (1), 129–161.

(46) Zhang, G.; Schilling, F.; Glaser, S. J.; Hilty, C. *Anal. Chem.* **2013**, *85* (5), 2875–2881.

(47) Mishkovsky, M.; Frydman, L. *ChemPhysChem* **2008**, *9* (16), 2340–2348.

(48) Frydman, L.; Scherf, T.; Lupulescu, A. *Proc. Natl. Acad. Sci.* **2002**, *99* (25), 15858–15862.

(49) Frydman, L.; Blazina, D. *Nat. Phys.* **2007**, *3* (6), 415–419.

(50) Tal, A.; Frydman, L. *Prog. Nucl. Magn. Reson. Spectrosc.* **2010**, *57* (3), 241–292.

(51) Chen, H.-Y.; Hilty, C. *Anal. Chem.* **2013**, *85* (15), 7385–7390.

(52) Bowen, S.; Zeng, H.; Hilty, C. *Anal. Chem.* **2008**, *80* (15), 5794–5798.

(53) Zhang, G.; Schilling, F.; Glaser, S. J.; Hilty, C. *J. Magn. Reson.* **2016**, *272*, 123–128.

(54) Peemoeller, H.; Shenoy, R. K.; Pintar, M. M. *J. Magn. Reson.* **1981**, *45* (2), 193–204.

(55) Peemoeller, H.; Pintar, M. M. *Biophys. J.* **1979**, *28* (2), 339–355.

(56) Bernin, D.; Topgaard, D. *Curr. Opin. Colloid Interface Sci.* **2013**, *18* (3), 166–172.

(57) Song, Y.-Q. *J. Magn. Reson.* **2013**, *229*, 12–24.

(58) Thrippleton, M. J.; Loening, N. M.; Keeler, J. *Magn. Reson. Chem.* **2003**, *41* (6), 441–447.

(59) Stejskal, E. O.; Tanner, J. E. *J. Chem. Phys.* **1965**, *42* (1), 288–292.

(60) Ahola, S.; Mankinen, O.; Telkki, V.-V. *Magn. Reson. Chem.* **2017**, *55* (4), 341–347.

(61) Loening, N. M.; Thrippleton, M. J.; Keeler, J.; Griffin, R. G. *J. Magn. Reson.* **2003**, *164* (2), 321–328.

(62) Shrot, Y.; Frydman, L. *J. Magn. Reson.* **2008**, *195* (2), 226–231.

(63) Smith, P. E. S.; Donovan, K. J.; Szekely, O.; Baias, M.; Frydman, L. *ChemPhysChem* **2013**, *14* (13), 3138–3145.

(64) Ahola, S.; Telkki, V.-V. *ChemPhysChem* **2014**, *15* (8), 1687–1692.

(65) Ahola, S.; Zhivonitko, V. V.; Mankinen, O.; Zhang, G.; Kantola, A. M. *et al. Nat. Commun.* **2015**, *6*, 8363.

(66) King, J. N.; Lee, V. J.; Ahola, S.; Telkki, V.-V.; Meldrum, T. *Angew. Chem. Int. Ed.* **2016**, *55* (16), 5040–5043.

(67) DeBerardinis, R. J.; Thompson, C. B. *Cell* **2012**, *148* (6), 1132–1144.

(68) Anthony, M. L.; Williams, S. N. O.; Brindle, K. M., *Animal Cell Biotechnology: Methods and Protocols*. Totowa: Humana Press, **1999**.

(69) Cohen, S. M.; Shulman, R. G.; McLaughlin, A. C. *Proc. Natl. Acad. Sci. U. S. A.* **1979**, *76* (10), 4808–4812.

(70) Alger, J.; Sillerud, L.; Behar, K.; Gillies, R.; Shulman, R. *et al. Science* **1981**, *214* (4521), 660–662.

(71) Jue, T.; Rothman, D. L.; Tavitian, B. A.; Shulman, R. G. *Proc. Natl. Acad. Sci. U. S. A.* **1989**, *86* (5), 1439–1442.

(72) Mashimo, T.; Pichumani, K.; Vemireddy, V.; Hatanpaa, K. J.; Singh, D. K. *et al. Cell* **2014**, *159* (7), 1603–1614.

(73) Damadian, R. *Science* **1971**, *171* (3976), 1151–1153.

(74) Meier, S.; Karlsson, M.; Jensen, P. R.; Lerche, M. H.; Duus, J. Ø. *Mol. Biosyst.* **2011**, *7* (10), 2834.

(75) Meier, S.; Jensen, P. R.; Duus, J. Ø. *FEBS Lett.* **2011**, *585* (19), 3133–3138.

(76) Gómez Damián, P. A.; Sperl, J. I.; Janich, M. A.; Khegai, O.; Wiesinger, F. *et al. Radiol. Res. Pract.* **2014**, *2014*, 1–10.

(77) Day, S. E.; Kettunen, M. I.; Gallagher, F. A.; Hu, D.-E.; Lerche, M. *et al. Nat. Med.* **2007**, *13* (11), 1382–1387.

(78) Harrison, C.; Yang, C.; Jindal, A.; DeBerardinis, R. J.; Hooshyar, M. A. *et al. NMR Biomed.* **2012**, *25* (11), 1286–1294.

(79) Hill, D. K.; Orton, M. R.; Mariotti, E.; Boult, J. K. R.; Panek, R. *et al. PLoS ONE* **2013**, *8* (9), 71996.

(80) Witney, T. H.; Kettunen, M. I.; Brindle, K. M. *J. Biol. Chem.* **2011**, *286* (28), 24572–24580.

(81) Lodi, A.; Woods, S. M.; Ronen, S. M. *NMR Biomed.* **2013**, *26* (3), 299–306.

(82) Keshari, K. R.; Sriram, R.; Koelsch, B. L.; Van Criekinge, M.; Wilson, D. M. *et al. Cancer Res.* **2013**, *73* (2), 529–538.

(83) Reineri, F.; Daniele, V.; Cavallari, E.; Aime, S. *NMR Biomed.* **2016**, *29* (8), 1022–1027.

(84) Brindle, K. M. *J. Am. Chem. Soc.* **2015**, *137* (20), 6418–6427.

(85) Schilling, F.; Düwel, S.; Köllisch, U.; Durst, M.; Schulte, R. F. *et al. NMR Biomed.* **2013**, *26* (5), 557–568.

(86) Koelsch, B. L.; Sriram, R.; Keshari, K. R.; Leon Swisher, C.; Van Criekinge, M. *et al. Magn. Reson.* **2016**, *270*, 115–123.

(87) Golman, K.; Zandt, R. in ‘t; Lerche, M.; Pehrson, R.; Ardenkjær-Larsen, J. H. *Cancer Res.* **2006**, *66* (22), 10855–10860.

(88) Golman, K.; Zandt, R. in ‘t; Thaning, M. *Proc. Natl. Acad. Sci.* **2006**, *103* (30), 11270–11275.

(89) Golman, K.; Ardenkjær-Larsen, J. H.; Petersson, J. S.; Mansson, S.; Leunbach, I. *Proc. Natl. Acad. Sci.* **2003**, *100* (18), 10435–10439.

(90) Warburg, O. *J. Cancer Res.* **1925**, *9* (1), 148–163.

(91) Amoêdo, N. D.; Valencia, J. P.; Rodrigues, M. F.; Galina, A.; Rumjanek, F. D. *Biosci. Rep.* **2013**, *33* (6), 865–873.

(92) Albers, M. J.; Bok, R.; Chen, A. P.; Cunningham, C. H.; Zierhut, M. L. *et al. Cancer Res.* **2008**, *68* (20), 8607–8615.

(93) Gallagher, F. A.; Kettunen, M. I.; Hu, D.-E.; Jensen, P. R.; Zandt, R. in ‘t. *et al. Proc. Natl. Acad. Sci.* **2009**, *106* (47), 19801–19806.

(94) Bohndiek, S. E.; Kettunen, M. I.; Hu, D. -E.; Witney, T. H.; Kennedy, B. W. C. *et al. Mol. Cancer Ther.* **2010**, *9* (12), 3278–3288.

(95) Gallagher, F. A.; Kettunen, M. I.; Brindle, K. M. *NMR Biomed.* **2011**, *24* (8), 1006–1015.

(96) Gallagher, F. A.; Kettunen, M. I.; Day, S. E.; Hu, D.-E.; Ardenkjær-Larsen, J. H. *et al. Nature* **2008**, *453* (7197), 940–943.

(97) Merritt, M. E.; Harrison, C.; Storey, C.; Jeffrey, F. M.; Sherry, A. D. *et al. Proc. Natl. Acad. Sci.* **2007**, *104* (50), 19773–19777.

(98) Schroeder, M. A.; Cochlin, L. E.; Heather, L. C.; Clarke, K.; Radda, G. K. *et al. Proc. Natl. Acad. Sci.* **2008**, *105* (33), 12051–12056.

(99) Golman, K.; Petersson, J. S.; Magnusson, P.; Johansson, E.; Åkeson, P. *et al. Magn. Reson. Med.* **2008**, *59* (5), 1005–1013.

(100) Merritt, M. E.; Harrison, C.; Sherry, A. D.; Malloy, C. R.; Burgess, S. C. *Proc. Natl. Acad. Sci.* **2011**, *108* (47), 19084–19089.

(101) Karlsson, M.; Jensen, P. R.; Zandt, R. in 't; Gisselsson, A.; Hansson, G. *et al. Int. J. Cancer* **2010**, *127* (3), 729–736.

(102) Ball, D. R.; Rowlands, B.; Dodd, M. S.; Le Page, L.; Ball, V. *et al. Magn. Reson. Med.* **2014**, *71* (5), 1663–1669.

(103) Gallagher, F. A.; Kettunen, M. I.; Day, S. E.; Lerche, M.; Brindle, K. M. *Magn. Reson. Med.* **2008**, *60* (2), 253–257.

(104) Bohndiek, S. E.; Kettunen, M. I.; Hu, D.; Kennedy, B. W. C.; Boren, J. *et al. J. Am. Chem. Soc.* **2011**, *133* (30), 11795–11801.

(105) Keshari, K. R.; Sai, V.; Wang, Z. J.; VanBrocklin, H. F.; Kurhanewicz, J. *et al. J. Nucl. Med.* **2013**, *54* (6), 922–928.

(106) Keshari, K. R.; Kurhanewicz, J.; Bok, R.; Larson, P. E. Z.; Vigneron, D. B. *et al. Proc. Natl. Acad. Sci.* **2011**, *108* (46), 18606–18611.

(107) Meier, S.; Jensen, P.; Karlsson, M.; Lerche, M. *Sensors* **2014**, *14* (1), 1576–1597.

(108) Miclet, E.; Abergel, D.; Bornet, A.; Milani, J.; Jannin, S. *et al. J. Phys. Chem. Lett.* **2014**, *5* (19), 3290–3295.

(109) Allouche-Arnon, H.; Hovav, Y.; Friesen-Waldner, L.; Sosna, J.; Moshe Gomori, J. *et al. NMR Biomed.* **2014**, *27* (6), 656–662.

(110) Jensen, P. R.; Meier, S.; Ardenkjær-Larsen, J. H.; Duus, J. Ø.; Karlsson, M. *et al. Chem. Commun.* **2009**, No. 34, 5168.

(111) Chen, A. P.; Hurd, R. E.; Gu, Y.; Wilson, D. M.; Cunningham, C. H. *NMR Biomed.* **2011**, *24* (5), 514–520.

(112) Allouche-Arnon, H.; Gamliel, A.; Barzilay, C. M.; Nalbandian, R.; Gomori, J. M. *et al. Contrast Media Mol. Imaging* **2011**, *6* (3), 139–147.

(113) Jamin, Y.; Gabellieri, C.; Smyth, L.; Reynolds, S.; Robinson, S. P. *et al. Magn. Reson. Med.* **2009**, *62* (5), 1300–1304.

(114) Bowen, S.; Hilty, C. *Anal. Chem.* **2009**, *81* (11), 4543–4547.

(115) Zeng, H.; Lee, Y.; Hilty, C. *Anal. Chem.* **2010**, *82* (21), 8897–8902.

(116) Lee, Y.; Heo, G. S.; Zeng, H.; Wooley, K. L.; Hilty, C. *J. Am. Chem. Soc.* **2013**, *135* (12), 4636–4639.

(117) Chen, C.-H.; Shih, W.-C.; Hilty, C. *J. Am. Chem. Soc.* **2015**, *137* (21), 6965–6971.

(118) Cala, O.; Guillière, F.; Krimm, I. *Anal. Bioanal. Chem.* **2014**, *406* (4), 943–956.

(119) Lee, Y.; Zeng, H.; Ruedisser, S.; Gossert, A. D.; Hilty, C. *J. Am. Chem. Soc.* **2012**, *134* (42), 17448–17451.

(120) Chappuis, Q.; Milani, J.; Vuichoud, B.; Bornet, A.; Gossert, A. D. *et al. J. Phys. Chem. Lett.* **2015**, *6* (9), 1674–1678.

(121) Lee, Y.; Zeng, H.; Mazur, A.; Wegstroth, M.; Carlomagno, T. *et al. Angew. Chem. Int. Ed.* **2012**, *51* (21), 5179–5182.

(122) Kim, Y.; Hilty, C. *Angew. Chem. Int. Ed.* **2015**, *54* (16), 4941–4944.

(123) Kim, Y.; Liu, M.; Hilty, C. *Anal. Chem.* **2016**, *88* (22), 11178–11183.

(124) Wang, Y.; Ragavan, M.; Hilty, C. *J. Biomol. NMR* **2016**, *65* (1), 41–48.

(125) Lerche, M. H.; Meier, S.; Jensen, P. R.; Baumann, H.; Petersen, B. O. *et al. J. Magn. Reson.* **2010**, *203* (1), 52–56.

(126) Harris, T.; Szekely, O.; Frydman, L. *J. Phys. Chem. B* **2014**, *118* (12), 3281–3290.

(127) Min, H.; Sekar, G.; Hilty, C. *ChemMedChem* **2015**, *10* (9), 1559–1563.

(128) Olsen, G.; Markhasin, E.; Szekely, O.; Bretschneider, C.; Frydman, L. *J. Magn. Reson.* **2016**, *264*, 49–58.

(129) Kim, J.; Liu, M.; Hilty, C. *J. Phys. Chem. B* **2017**.

(130) Schanda, P.; Brutscher, B. *J. Am. Chem. Soc.* **2005**, *127* (22), 8014–8015.

(131) Schanda, P.; Kupče, Ē.; Brutscher, B. *J. Biomol. NMR* **2005**, *33* (4), 199–211.

(132) Chen, H.-Y.; Ragavan, M.; Hilty, C. *Angew. Chem. Int. Ed.* **2013**, *52* (35), 9192–9195.

(133) Kurzbach, D.; Canet, E.; Flamm, A. G.; Jhajharia, A.; Weber, E. M. M. *et al. Angew. Chem. Int. Ed.* **2017**, *56* (1), 389–392.

(134) Ragavan, M.; Iconaru, L. I.; Park, C.-G.; Kriwacki, R. W.; Hilty, C. *Angew. Chem. Int. Ed.* **2017**, *56* (25), 7070–7073.

(135) Kupče, E.; Nishida, T.; Freeman, R. *Prog. Nucl. Magn. Reson. Spectrosc.* **2003**, *42* (3–4), 95–122.

(136) Bloom, A. L.; Shoolery, J. N. *Phys. Rev.* **1955**, *97* (5), 1261–1265.

(137) Anderson, W. A.; Freeman, R. *J. Chem. Phys.* **1962**, *37* (1), 85–103.

(138) Waugh, J. S. *J. Magn. Reson.* **1982**, *50* (1), 30–49.

(139) Neves, J. L.; Heitmann, B.; Khaneja, N.; Glaser, S. J. *J. Magn. Reson.* **2009**, *201* (1), 7–17.

(140) Schilling, F.; Glaser, S. J. *J. Magn. Reson.* **2012**, *223*, 207–218.

(141) Schilling, F.; Warner, L. R.; Gershenzon, N. I.; Skinner, T. E.; Sattler, M. *et al. Angew. Chem. Int. Ed.* **2014**, *53* (17), 4475–4479.

(142) Khaneja, N.; Reiss, T.; Kehlet, C.; Schulte-Herbrüggen, T.; Glaser, S. J. *J. Magn. Reson.* **2005**, *172* (2), 296–305.

(143) Glaser, S. J.; Boscain, U.; Calarco, T.; Koch, C. P.; Köckenberger, W. *et al. Eur. Phys. J. D* **2015**, *69* (12).

(144) Harris, R. K.; Becker, E. D.; De Menezes, S. M. C.; Granger, P.; Hoffman, R. E. *et al. Magn. Reson. Chem.* **2008**, *46* (6), 582–598.

(145) Zeng, H.; Bowen, S.; Hilty, C. *J. Magn. Reson.* **2009**, *199* (2), 159–165.

(146) Szwarc, M. *Nature* **1956**, *178* (4543), 1168–1169.

(147) Szwarc, M.; Levy, M.; Milkovich, R. *J. Am. Chem. Soc.* **1956**, *78* (11), 2656–2657.

(148) Matsuzaki, K.; Shinohara, Y.; Kanai, T. *Makromol. Chem.* **1980**, *181* (9), 1923–1934.

(149) Ernst, R. R. *J. Chem. Phys.* **1966**, *45* (10), 3845–3861.

(150) Siddiqui, S.; Kadlecek, S.; Pourfathi, M.; Xin, Y.; Mannherz, W. *et al. Adv. Drug Deliv. Rev.* **2016**.

(151) Serrao, E. M.; Brindle, K. M. *Front. Oncol.* **2016**, *6*.

(152) Harris, T.; Eliyahu, G.; Frydman, L.; Degani, H. *Proc. Natl. Acad. Sci.* **2009**, *106* (43), 18131–18136.

(153) Merritt, M. E.; Harrison, C.; Storey, C.; Sherry, A. D.; Malloy, C. R. *Magn. Reson. Med.* **2008**, *60* (5), 1029–1036.

(154) Moret, S.; Dyson, P. J.; Laurenczy, G. *Dalton Trans.* **2013**, *42* (13), 4353.

(155) Daniels, C. J.; McLean, M. A.; Schulte, R. F.; Robb, F. J.; Gill, A. B. *et al. NMR Biomed.* **2016**, *29* (4), 387–399.

(156) Brindle, K. M.; Bohndiek, S. E.; Gallagher, F. A.; Kettunen, M. I. *Magn. Reson. Med.* **2011**, *66* (2), 505–519.

(157) Shatzkes, K.; Teferedegne, B.; Murata, H. *Sci. Rep.* **2015**, *4* (1).

(158) Thrippleton, M. J.; Loening, N. M.; Keeler, J. *Magn. Reson. Chem.* **2003**, *41* (6), 441–447.

(159) Holz, M.; Heil, S. R.; Sacco, A. *Phys. Chem. Chem. Phys.* **2000**, *2* (20), 4740–4742.

(160) Godefroy, S.; Callaghan, P. T. *Magn. Reson. Imaging* **2003**, *21* (3–4), 381–383.

(161) Venkataramanan, L.; Yi-Qiao Song; Hurlimann, M. D. *IEEE Trans. Signal Process.* **2002**, *50* (5), 1017–1026.

(162) Zhu, Y.; Chen, C.-H.; Wilson, Z.; Savukov, I.; Hilty, C. *J. Magn. Reson.* **2016**, *270*, 71–76.

(163) Krishnan, V. V.; Murali, N. *Prog. Nucl. Magn. Reson. Spectrosc.* **2013**, *68*, 41–57.

(164) Stepišnik, J.; Lasič, S.; Mohorič, A.; Serša, I.; Sepe, A. *J. Magn. Reson.* **2006**, *182* (2), 195–199.

(165) Tsuruda, J. S.; Chew, W. M.; Moseley, M. E.; Norman, D. *Magn. Reson. Med.* **1991**, *19* (2), 316–320.

(166) Stejskal, E. O.; Tanner, J. E. *J. Chem. Phys.* **1965**, *42* (1), 288–292.

(167) Tanner, J. E. *J. Chem. Phys.* **1970**, *52* (5), 2523–2526.

(168) Koelsch, B. L.; Reed, G. D.; Keshari, K. R.; Chaumeil, M. M.; Bok, R. *et al. Magn. Reson. Med.* **2015**, *74* (3), 622–633.

(169) Callaghan, P. T., *Translational Dynamics and Magnetic Resonance: Principles of Pulsed Gradient Spin Echo NMR*. Oxford: Oxford University Press, **2011**.

(170) Pelupessy, P. *J. Am. Chem. Soc.* **2003**, *125* (40), 12345–12350.

(171) Akoka, S.; Giraudeau, P. *Magn. Reson. Chem.* **2015**, *53* (11), 986–994.

(172) Guduff, L.; Kuprov, I.; van Heijenoort, C.; Dumez, J.-N. *Chem. Commun.* **2017**, *53* (4), 701–704.

(173) Song, Y.-Q.; Venkataramanan, L.; Hürlimann, M. D.; Flaum, M.; Frulla, P. *et al. J. Magn. Reson.* **2002**, *154* (2), 261–268.

(174) Granwehr, J.; Roberts, P. J. *J. Chem. Theory Comput.* **2012**, *8* (10), 3473–3482.

(175) Warburg, O. *Science* **1956**, *123* (3191), 309–314.

(176) Koelsch, B. L.; Keshari, K. R.; Peeters, T. H.; Larson, P. E. Z.; Wilson, D. M. *et al. The Analyst* **2013**, *138* (4), 1011.

(177) Kettunen, M. I.; Kennedy, B. W. C.; Hu, D.; Brindle, K. M. *Magn. Reson. Med.* **2013**, *70* (5), 1200–1209.

(178) Ullah, M. S.; Davies, A. J.; Halestrap, A. P. *J. Biol. Chem.* **2006**, *281* (14), 9030–9037.